Politecnico di Torino

Politecnico di Torino

Master of Science in Aerospace Engineering

Academic Year 2024/2025

Graduation Session October 2025

Role of gravity stress on pressure and flow wave patterns in the arterial tree: from micro- to hyper-gravity conditions

Supervisors:

Stefania Scarsoglio

Luca Ridolfi

Francesco Tripoli

Candidate:

Giovanna Colussi

Abstract

The evolution of the human cardiovascular system has taken place under Earth's gravitational conditions, leading to an optimal configuration which results highly sensitive to deviations from this environment. As a matter of fact, alterations in gravitational acceleration (ranging from microgravity to hypergravity) induce a cascade of physiological responses affecting both cardiac and vascular functions. The mechanism of fluid shift toward the cranial or caudal body compartments, triggered by microgravity and hypergravity respectively, has been identified as the driver of critical cardiovascular alterations, such as cardiac atrophy, hypovolemia, orthostatic intolerance, and diminished venous return. It is widely known that, under increasing gravitational loads, the cardiovascular system experiences pronounced orthostatic stress, resulting in marked changes in several central hemodynamic parameters (such as stroke volume reduction and heart rate elevation), as well as influencing the dynamics of pressure and flow wave propagation, which are inherently delayed due to vessel wall viscoelasticity. While the general framework of cardiovascular adaptation to the gravitational environment is widely recognized, detailed descriptions and insights into hemodynamic changes still remain limited due to the scarcity of in-vivo data from spaceflight as well as ground-based analogues. The present work fits within this scenario, resorting to the use of a validated multiscale (0D-1D) cardiovascular model to explore acute hemodynamic responses in upright posture to varying gravitational levels, ranging from 0g to 3g environment. The analysis will be conducted with a specific focus on wave propagation phenomena, at specific positions along the arterial network. The model combines a 1D representation of major systemic and coronary arteries with a lumped-parameter (0D) depiction of distal compartments, venous return, cardiopulmonary and ocular-cerebrovascular circulations. Key short-term regu latory mechanisms, including baroreflex, cardiopulmonary reflexes, and cerebral autoregulation, are incorporated within the model, along with posture- and gravity-related effects. By means of waveform analysis and decomposition of blood pressure and flow signals along the 1D arterial domain, the characterization of the gravity-dependent variations in forward and backward wave components is carried out, along with the assessment of altered spatio-temporal patterns implications at the cardiac level. Furthermore, specific attention is given to wave trapping mechanisms (known to preserve the heart region from adverse wave reflections under normal gravity) which interestingly may undergo alterations or impairment in hypergravity conditions. Present results suggest that the computational approach is a promising tool increasingly adopted, which can affordably and reliably contribute to filling the current in vivo gaps associated to the cardiovascular response to altered gravity induced by human spaceflight.

Table of Contents

Chapter 1

Introduction

Human presence during spaceflight missions remains an irreplaceable factor from a technical standpoint, as well as a symbol of humanity's inextinguishable aspiration to expand the boundaries of scientific knowledge. However, the human cardiovascular system (CVS) undergoes a constellation of severe haemodynamic alterations whenever a change in hydrostatic pressure gradient occurs. A key aspect to investigate and evaluate CVS functioning lies in the analysis of blood pressure and flow waves travelling throughout the arterial tree. In particular, the study of wave patterns under different hydrostatic stress is of great importance since it is closely connected with the arterial haemodynamic response. In fact, pressure-flow wave patterns arise as a consequence of arterial system characteristics, due to both mechanical and geometric properties of the arterial tree structure. During a cardiac cycle, the contraction and relaxation of the left ventricle induces pressure and flow waves through the aortic valve, which propagate from the aortic root to all peripheral compartments. Along their path from central to distal regions, these waves encounter successive bifurcations, resulting in continuous reflections and in the generation of backward-propagating wave components [1][2][3][4]. Consequently, at any location within the arterial tree, the local pressure and flow waveforms are shaped by the superposition of a direct and a retrograde traveling wave.

The phenomenon of wave reflection plays an important role in the cardiac workload and represents a point of concern in terms of safeguarding the natural cardiac functionality. It is known that the change in hydrostatic pressure gradient has an impact on waves transmission and reflection phenomena and that the causes behind a change in hydrostatic stress lie, for instance, in the variation of body posture or in the alteration of gravitational environmental conditions. Anyway, while the former cause has already been investigated [5], the dependence of the dynamics of travelling waves on the gravitational acceleration remains unclear.

Since the human CVS evolved under 1G conditions—which also represent the most accessible framework for in vivo analysis—numerous studies have recently focused on this environment. In this regard, [4] and [6] showed that the 1G supine position represents an optimized condition for wave transmission and reflection. Indeed, forward-traveling waves are efficiently propagated across arterial bifurcations, primarily due to favorable cross-sectional area matching between parent and daughter vessels and the presence of tapering vascular segments, resulting in minimal energy loss. In contrast, backward waves are largely unable to propagate retrogradely toward the aortic valve due to a complex mechanism of re-reflection known as wave trapping. This mechanism, under 1G supine conditions, proves effective in preserving cardiac functionality. According to [5], an investigation was conducted aiming at understanding whether this optimal 1G supine CVS configuration is preserved when tilting from supine to upright position. Their results show a good vessel lumens matching at arterial bifurcations in the forward direction, the preservation of the wave entrapment mechanism and a reduction in wave reflection at central level likely due to the backward propagation of attenuated pressure waves produced by cerebral autoregulation.

Within this framework, the present work aims to computationally shed light on the cardiovascular knowledge gap related to the effect of gravitational environment alterations on pressure and flow wave patterns. To this end, the 1G upright condition is chosen as the baseline for numerical analysis. This choice is supported by the fact that it reflects the posture in which healthy individuals spend most of their day, while also allowing consistent comparisons under different gravitational accelerations (g) without introducing postural variability. In this study, a total of 31 gravitational cases—ranging from microgravity (0G) to hypergravity (3G), in 0.1G increments—are analyzed, all in the upright posture. It should be noted that in microgravity, the "standing" posture differs from the upright 1G condition and is instead referred to as the "Neutral Body Posture," characterized by a lowering of the line of sight (approximately -$15^o \pm 2^o$) and a reduction in hip angle (approximately -$52^o \pm 7^o$). Through this posture-independent analysis, the present work aims at exploring the gravity-induced wave dynamics, which is directly connected to the alteration of the hydrostatic pressure gradient, focusing at specific positions along the arterial network. For the present analysis, a closed-loop, multi-scale model of the entire human CVS has been adopted, which has been already validated under various operative conditions [7][8]. The model is a combination of a 1D representation of major systemic and coronary arteries and a lumped-parameter (0D) depiction of distal compartments, venous return, cardiopulmonary and ocular-cerebrovascular circulations. The model also takes into account short-term regulatory mechanisms (including baroreflex, cardiopulmonary reflexes and cerebral autoregulation), along with posture- and gravity-related effects.

Resorting to the use of this mathematical model, wave analysis (WA) has been carried out in function of gravitational variation, with a specific focus on pressure and flow waves transmission and reflection phenomena. The present work, first provides an overview of the mathematical foundation of the WA, where the concept of wave, the Method of Characteristics and the theory behind wave separation are briefly introduced. After that, a more detailed description of the cardiovascular model used for the numerical simulations and of the main central physiological adaptations to changes in gravitational load is presented. Subsequently, the core of the study is illustrated. Following the processing of the numerical data, the results obtained through WA are presented, in terms of arterial tree wave patterns, characteristic impedance, wave speed and reflection parameters. Furthermore, specific metrics are introduced to quantify the impact of gravitational stress on waveform morphology, with respect to the baseline 1G condition, for both forward and backward components. Finally, a comprehensive discussion is provided to underline and summarise the influence of the gravitational acceleration variable on wave propagation mechanisms within the human CVS, under constant postural conditions.

Chapter 2

Mathematical Foundation of the Wave Analysis

2.1 Interpretative Remarks on the Concept of Wave

The problem of tracking the propagation of waves through the flow field has played a crucial role in the development of gas dynamics. In 1858, Bernhard Riemann provided the mathematical tools for the solution of hyperbolic equations, such as Euler Equations, being the first to systematically apply the Method of Characteristics to nonlinear hyperbolic systems, laying the foundations for the modern theory of discontinuity propagation. Referring to the human cardiovascular system, although arteries naturally exhibit complex three-dimensional geometries, for several practical purposes they can be well approximated as 1D pipes [9], with a preferential direction characterized by a characteristic length scale significantly greater than the others. On one hand, the 1D approximation obviously neglects any cross-sectional velocity variation and does not account for the no-slip wall condition. On the other hand, this approach turns out to be optimal for the axial determination of the pressure and velocity field along the vessel. At this point, a clarification on what is meant by "wave" is necessary to avoid any kind of ambiguity throughout this work. According to the definition of [10], a wave is a change in pressure and flow that propagates along a blood vessel, whereas for [11] the term 'waveform' refers to the pressure or flow pulse signal that can be measured at a particular vascular location. As clearly explained in [9], every single waveform can be considered as the result of a sequence of small discontinuities, called "wavefronts", whose combination produces the overall measured wave. From the analytical perspective, this interpretation of wave phenomenon represents a

point of contact with the Riemann approach and results particularly suitable for the application of the Method of Characteristic, in the so-called wave intensity analysis. Moreover, from the data acquisition perspective, this approach is amenable to a digital sampling procedure, which allows for an accurate description of each wavefront as a discrete change in properties during a sampling period. Nevertheless, this definition of a wave is not the sole interpretation that has found acceptance in the scientific literature. In fact, in many scientific contexts, a waveform is seen as a composition of sinusoidal wavetrains, each of one representing a fundamental element of Fourier analysis. In this optic, the measured wave is the result of the sum of all sinusoidal wavetrains, associated to the fundamental and higher harmonic frequencies.
In Figure 2.1, an example of both wave decomposition methodologies is illustrated, according to [9].

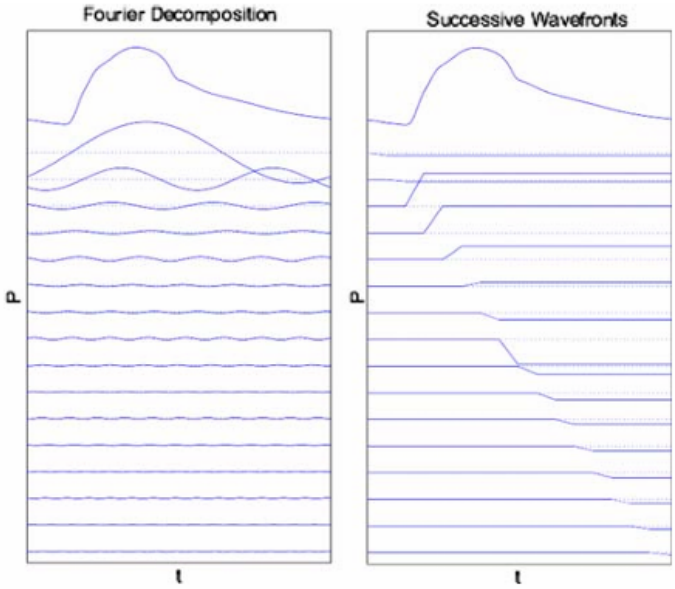

Figure 2.1: Representation of the pressure signal recorded in the human aorta during a cardiac cycle, decomposed into sinusoidal wave trains (left) and sequential wave fronts (right) [9]. In both panels, the original pressure waveform is displayed at the top.

It is important to note that, considering all particular wave decompositions, no one is intrinsically better than the other: Fourier analysis and wave intensity analysis each provide a distinct, rigorous and comprehensive characterization of the measured waveform. In the present work, the choice fell on the latter one, a decision guided primarily by consideration of analytical and practical convenience.

2.2 The Method of Characteristics

Once clarified the wave related terminology, an overview about the main aspects of the Method of Characteristics (MOC) is reported below.
The MOC typically represents the go-to technique for the solution of quasilinear hyperbolic systems of partial differential equations, such as the 1D Euler equations governing inviscid flow in elastic tubes. Focusing on the inviscid and incompressible case, the method can be tailored for the study of blood flow in large arteries, applying the conservation of mass and momentum to a Newtonian fluid interacting with a compliant wall.
In particular, the continuity equation, applied to a differential element of the tube, requires that the difference between the volume inflow and outflow rates is equal to the change in volume of the element. Along with this, the momentum equation requires that the fluid acceleration within the control volume equals the net incoming momentum flux combined with the net force exerted by the pressure.

$$\begin{cases} \frac{\partial A}{\partial t} + \frac{\partial (AU)}{\partial x} = 0 \\ \frac{\partial U}{\partial t} + U\frac{\partial U}{\partial x} + \frac{1}{\rho}\frac{\partial p}{\partial x} = 0 \end{cases}$$

Here, A(x,t) represents the cross-sectional area of the tube, U(x,t) is the axial velocity averaged over the cross-section, ρ is the fluid density (assumed to be constant), and p(x,t) is the hydrostatic pressure averaged over the cross-section. The 1D Euler system, then, involves two independent variables:

- x, that represents the axial distance along the tube;
- t, that represents the time.

On the other hand, three independent variables appear in the conservation equations: U, A and p. Then, a constitutive relationship, reflecting vessel wall elasticity, is necessary to close the system:

$$A(x,t) = A(p(x,t);x) \tag{2.1}$$

According to this functional relation, the local cross-sectional area changes as a function of local pressure and location along the vessel. Although it does not contain a direct dependence on time variable, the temporal variation of pressure still introduces a time-dependent behaviour of the local area of the tube. Focusing on the dependent variables most frequently used for clinical measures, p and U, the partial derivatives of A can be written:

$$\begin{cases} \left(\frac{\partial A}{\partial x}\right)_t = A_p\frac{\partial p}{\partial x} + \frac{\partial A}{\partial x} \\ \left(\frac{\partial A}{\partial t}\right)_x = A_p\frac{\partial p}{\partial t} \end{cases}$$

where

$$A_p = \left(\frac{\partial A}{\partial p}\right)_x \qquad A_x = \left(\frac{\partial A}{\partial x}\right)_p \tag{2.2}$$

It is important to note that A_p represents the local area compliance of the artery, which is defined as the local change in cross-sectional vessel area caused by a local variation in pressure. Remembering that area compliance for vessels is proportional to

$$C_A = \frac{\Delta A}{\Delta P} \propto \frac{k\pi r_i^3}{E_{inc} h} \tag{2.3}$$

one can assume it as a measure of the local stiffness of the artery, being E_{inc} the incremental Young modulus, h the wall thickness, r_i the internal vessel radius and k an adimensional parameter (k = 1.5 - 2). Through a substitution and a rearrangement of these terms, a system of two conservation equations can be obtained:

$$\begin{cases} \frac{\partial p}{\partial t} + U\frac{\partial p}{\partial x} + \frac{A}{A_p}\frac{\partial U}{\partial x} = -\frac{U}{A_p}\frac{\partial A}{\partial x} \\ \frac{\partial U}{\partial t} + \frac{1}{\rho}\frac{\partial p}{\partial x} + U\frac{\partial U}{\partial x} = 0 \end{cases}$$

The system can be written in matrix form, highlighting the matrix of coefficients of the x derivative terms:

$$\begin{Bmatrix} p \\ U \end{Bmatrix}_t + \begin{bmatrix} U & A/A_p \\ 1/\rho & U \end{bmatrix} \begin{Bmatrix} p \\ U \end{Bmatrix}_x = \begin{Bmatrix} -\frac{U}{A_p}\frac{\partial A}{\partial x} \\ 0 \end{Bmatrix}$$

The eigenvalues of the coefficient matrix of the spatial derivatives in a system of PDEs has a peculiar physical meaning: they represent the characteristic speeds of the system, that is, the speeds at which information (or disturbances) propagate in the x-t plane (i.e. the phase plane). In the Method of Characteristics, these define the slopes of the characteristic lines in the space-time domain, allowing the reduction of the original PDE system to an ODE one, along those curves. The interesting aspect of MOC is that the characteristic speeds are expressed in terms of the physical parameters of the problem (U, A, ρ and A_p):

$$\lambda_\pm = U \pm \sqrt{\frac{A}{\rho A_p}} = U \pm c \tag{2.4}$$

Being A a function of p and x, c would depend on p and x as well. For the sake of simplicity, c will be considered constant for each particular position along the arterial tree: c=c(x).
According to [9], this assumption results acceptable for our purposes, even though real arteries become stiffer as internal vessel pressure increases.

The hyperbolic nature of Euler Equations assures the existence of real and distinct eigenvalues of the matrix of coefficients, paving the way for Riemann solution of this system of equations through the MOC. In particular, Riemann observed that along the characteristic directions ($dx/dt = \lambda_{\pm}$), the total derivative with respect to time can be expressed in the form of Lagrangian transport:

$$\frac{D}{Dt} = \frac{\partial}{\partial t} + \frac{dx}{dt}\frac{\partial}{\partial x} = \frac{\partial}{\partial t} + (U \pm c)\frac{\partial}{\partial x} \tag{2.5}$$

Once the eigenvalues are known, the associated eigenvectors can be calculated, diagonalizing the system:

$$\vec{r}_{\pm} = \left\{ \begin{array}{c} 1 \\ \pm\rho c \end{array} \right\} \tag{2.6}$$

Then, by projecting the system along the directions represented by the eigenvectors (i.e. along the characteristics), the following equations are obtained:

$$\frac{D}{Dt}\left(U \pm \int \frac{dp}{\rho c}\right) = \mp \frac{Uc}{A}\frac{\partial A}{\partial x} \tag{2.7}$$

where

$$R_{\pm} = U \pm \int \frac{dp}{\rho c} \tag{2.8}$$

are called Riemann variables. In the case of uniform vessel, the source term vanishes, since $\partial A/\partial x = 0$. Then, the Riemann variables result to be constant along the characteristic lines:

$$\frac{DR_{\pm}}{Dt} = 0 \tag{2.9}$$

For this reason, in this case they are generally referred to as *Riemann invariants*.

According to this analytical result, two physical quantities have been found, the Riemann invariants precisely, that remain constant along paths that propagate with speed U+c e U-c. According to the arterial physiology, the blood flow velocity (U) is usually in the order of [cm/s], whereas c is in the order of [m/s]. For this reason, when the blood is moving, the waves are carried along with it: one moves downstream (at a velocity of U + c) and the other upstream (at U – c). Moreover, the fact that $U << c$ supports the interpretation of c as the wave propagation speed. To determine the solution at a specific point (x, t), one must identify the two waves intersecting at that location. Then, the corresponding values of the Riemann variables R_+ and R_- must be calculated, allowing the final evaluation of the pressure p and velocity U at (x,t) using:

$$p = \frac{\rho c}{2}(R_+ - R_-) \qquad U = \frac{1}{2}(R_+ + R_-) \tag{2.10}$$

where c is assumed to be constant with respect to pressure variations. In practice, however, the procedure is more complex: the trajectory of each wave depends on the local flow velocity, which itself is influenced by the incoming waves from both directions. Additionally, since c may vary with pressure, solving for p and U may require integrating along characteristic curves.

To sum up, any disturbance introduced into an arterial vessel propagates as pressure and flow rate waves: forward at a speed of U + c and backward at U - c. In particular, c is generally called wave speed and depends on the artery's distensibility (D):

$$D = \frac{A_p}{A} \tag{2.11}$$

2.3 Wave decomposition

An immediate consequence of the Method of Characteristic is the generally so-called water hammer equation for tubes. This equation describes the relationship between a change in pressure (dP) and a change in velocity (dU) across a wavefront, under the hypothesis of only forward or backward waves existence, constant diameter, absence of bifurcations, negligible pressure drops and absence of cavitation. The concept expressed by this relation basically lies in the constraint of preservation of the value of Riemann variable on the backward characteristic line also where it intersects a forward characteristic line. In other terms, at a specific point in space-time influenced by an incoming forward wave, the backward-traveling information must still be respected.

In practice, the equations state:

$$dR_{-} = dU^{+} - \frac{dp^{+}}{\rho c} = 0 \qquad for\ a\ forward\ wave \tag{2.12}$$

$$dR_{+} = dU^{-} + \frac{dp^{-}}{\rho c} = 0 \qquad for\ a\ backward\ wave \tag{2.13}$$

$$\rightarrow \qquad dp_{\pm} = \pm\, \rho c\, dU_{\pm} \tag{2.14}$$

where dp_{+} and dU_{+} represent the change in pressure and velocity for a forward-traveling wave, whereas dp_{-} and dU_{-} represent the same changes for a backward-traveling wave.
The water hammer equations reveal how the propagation of any wave involves a continuous exchange of energy between different forms. In arterial waves, the relation between dp and dU assumes a further meaning of exchange between the

potential energy stored in the elastic vessel walls (p) and the kinetic energy of the flowing blood (U).

Making the assumption of linear wave propagation [9], one can conclude that the forward and backward waves are additive when they intersect. According to this condition, one can write:

$$dp = dp_+ + dp_- \qquad dU = dU_+ + dU_- \tag{2.15}$$

From the combination of the water hammer equations with the relations of linear addition, a decomposition of the measured pressure and flow rate waves can be obtained. According to this method, the forward and backward contributes within the total waves can be distinguished and computed:

$$dp_\pm = \frac{dp \pm \rho c dU}{2} \tag{2.16}$$

$$dU_\pm = \frac{dU \pm dp/\rho c}{2} \tag{2.17}$$

2.4 Characteristic Impedance and Wave Speed

The equations 2.16 and 2.17 are valid until the wave analysis concerns large conduit arteries, characterized by a large Womersley number. In these cases, blood viscosity and wall viscoelasticity are negligible and the ratio between a local change in pressure and flow rate during the early systolic phase turns out to be a real number, called Characteristic Impedance (Z_c). In conduit arteries, it can be shown that this parameter can be evaluated as follows:

$$Z_c = \frac{\rho c}{A} \tag{2.18}$$

where ρ represents the blood density (constant), c is the wave speed in the arterial vessel and A stands for the cross-sectional area of the artery.
Recalling that the volumetric flow rate (Q) is defined as $A \cdot U$, another form for the water hammer equations can be written:

$$dp_\pm = \pm Z_c dQ_\pm \quad \rightarrow \quad p_\pm = \pm Z_c Q_\pm \tag{2.19}$$

The Characteristic Impedance, in absence of reflections, is a local parameter that is independent of peripheral resistance, depending only on local arterial properties and reflecting arterial stiffness and geometry.

2.5 Reflection Parameters

Once the wave has been decomposed into its forward and backward components, two wave reflection parameters can be defined:

- Reflection Magnitude : $RM = \frac{p_-}{p_+}$
- Reflection Index : $RI = \frac{p_-}{p_+ + p_-}$

Both parameters are computed using the amplitudes of the decomposed waves. While the Reflection Magnitude (RM) represents the ratio of the reflected wave amplitude to that of the forward component, the Reflection Index (RI) serves as a reliable estimator of the magnitude of overall reflection. Specifically, it highlights the contribution of the reflected wave relative to the total wave, thus indicating the extent to which reflection phenomena affect the complete wave propagating through the vessel.

Chapter 3

The cardiovascular model

The proposed model is a closed-loop, multiscale representation of the human cardiovascular system, integrating a one-dimensional (1D) description of the arterial tree with multiple zero-dimensional (0D) lumped-parameter models for various circulatory subsystems. It is calibrated on a healthy adult male aged 25 years, weighing 75 kg and measuring 175 cm in height, and accounts for gravitational effects induced by postural changes through a tilt-table simulation framework.

The one-dimensional (1D) arterial network includes 63 major arteries modeled as tapered, bifurcating vessels. These are organized into 15 coronary arteries and 48 primary large arteries, extending from the ascending aorta to the arteries of the upper and lower limbs. Blood flow in this network is governed by the axisymmetric form of the Navier–Stokes equations, while the arterial wall mechanics are described by a nonlinear viscoelastic constitutive law relating pressure to the local circular cross-sectional area. At each bifurcation, conservation of mass and total pressure is imposed as a boundary condition. The inlet of the 1D model, located at the level of the ascending aorta, is coupled with a zero-dimensional (0D) representation of the aortic valve. Each of the 24 terminal arteries in the 1D model is connected to a three-element RLC Windkessel model representing the distal arteriolar compartment via a characteristic impedance. These boundary value problems are solved using the Method of Characteristics, as described in Section 2.2, and the 1D governing equations are numerically integrated via a Discontinuous Galerkin Finite Element method in combination with a two-stage explicit Runge-Kutta time integration scheme. The Figure 3.1 schematically shows the multiscale cardiovascular model, illustrating the 1D arterial tree and its connections with the different 0D compartments.

The 0D lumped-parameter model is employed to represent the peripheral and venous circulations, as well as the cardiopulmonary, coronary, cerebrovascular, and

ocular compartments.

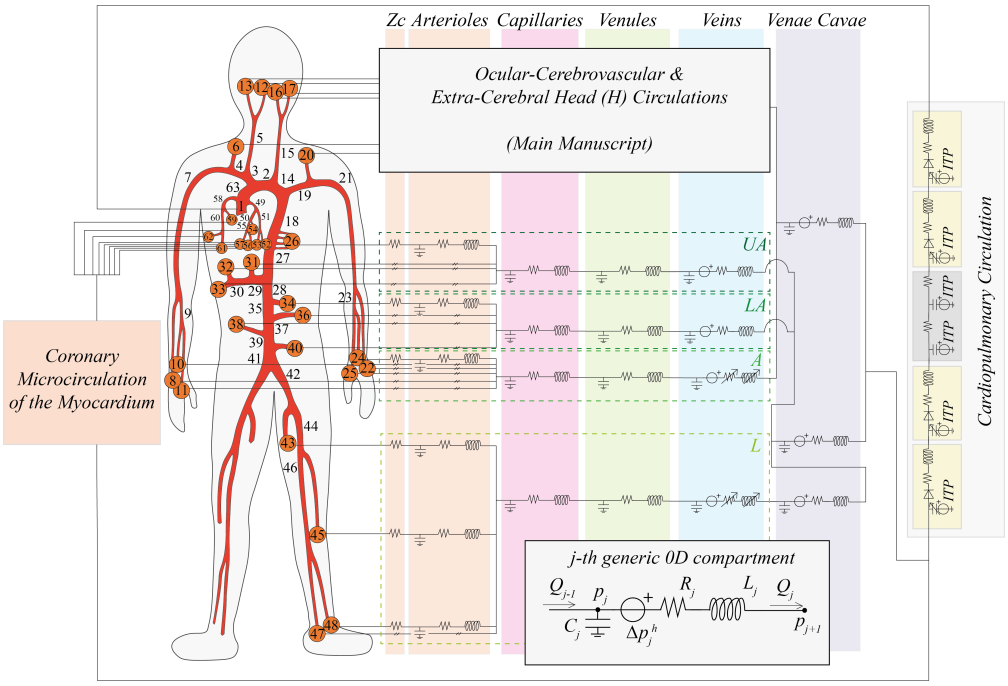

Figure 3.1: Schematic illustration of the multiscale Cardiovascular Model. The sketch shows the one-dimensional arterial tree (left), the structure of the general zero-dimensional compartments (grey box, bottom), and the cardiopulmonary circulation (right). The connections between the 1D model and the coronary microvascular compartments, the extracerebral head circulation, and the ocular-cerebrovascular circulation are also illustrated.

In particular, the **peripheral and venous circulations** are modeled using multiple interconnected three-element RLC Windkessel circuits, where R, L, and C denote the hydraulic resistance, blood inertance, and local vessel compliance, respectively. The generic 0D compartment is shown inside the grey box, in the lower part of Figure 3.1. Each terminal branch of the 1D arterial network is connected to a corresponding 0D arteriolar compartment, which subsequently feeds into capillary, venular, and venous segments. The arteriolar compartments are grouped into five anatomical regions: head, upper limbs, upper abdomen, lower abdomen, and lower limbs. Three major venous pathways—corresponding to the superior, inferior, and abdominal segments of the vena cava—connect these regions to the right atrium, thereby closing the systemic circulation and ensuring venous return. In addition, the venous segments of the arms and legs include 0D models of venous valves, which prevent backflow. The system of ordinary differential equations governing the 0D compartments is solved using a time-marching two-stage Runge-Kutta explicit

scheme, consistent with that used for the 1D model.
According to the Windkessel model and based on the principles of mass and momentum conservation, the following equations govern blood flow in a generic (i,j)-th 0D compartment within the peripheral circulation and venous return:

$$\frac{dV_{i,j}}{dt} = Q_{i,j-1} - Q_{i,j}\,, \tag{3.1}$$

$$\frac{dQ_{i,j}}{dt} = \begin{cases} \dfrac{p_{i,j} + \Delta p^h_{i,j} - R_{i,j}Q_{i,j} - p_{i,j+1}}{L_{i,j}}, & \text{if } j \in \{v, svc, ivc, avc\} \\ \dfrac{p_{i,j} - R_{i,j}Q_{i,j} - p_{i,j+1}}{L_{i,j}}, & \text{if } j \in \{art, cap, ven\} \end{cases}, \tag{3.2}$$

$$V_{i,j} = V^{un}_{i,j} + \Big(p_{i,j} - p^{ext}_{i,j}\Big)C_{i,j}\,, \tag{3.3}$$

where i identifies the specific body region under consideration (H: head, A: arms, UA: upper abdomen, LA: lower abdomen, L: legs), while j refers to the type of vascular compartment—namely, arterial (art), capillary (cap), venular (ven), venous (v), superior vena cava (svc), inferior vena cava (ivc), or abdominal vena cava (avc). The intraluminal pressure within the (i,j)-th compartment is denoted by $p_{i,j}$, and the corresponding blood flow rate is represented by $Q_{i,j}$. The hydraulic resistance and inertance associated with that compartment are indicated by $R_{i,j}$ and $L_{i,j}$, respectively. Finally, $V_{i,j}$ represents the compartmental total blood volume, $C_{i,j}$ the compartmental compliance and $p^{ext}_{i,j}$ either intracranial (ICP) or intrathoracic pressure (ITP) (if specified, otherwise $p^{ext}_{i,j} = 0\,mmHg$).

The term $\Delta p^h_{i,j}$ in 3.2, defined according to Stevino's law, plays a key role in the model by introducing hydrostatic pressure effects arising from variations in tilt angle (α) or gravitational acceleration (g). In the following equation $\Delta h_{i,j}$ represents the hydrostatic height of the corresponding fluid column, which is applied only to v, svc, ivc and avc compartments.

$$\Delta p^h_{i,j} = \rho g\, \Delta h_{i,j}\, \sin\alpha\,, \tag{3.4}$$

Focusing on the **cerebro-ocular system**, the blood flow originating from the internal carotid and vertebral arteries supplies the ocular–cerebrovascular circulation, which integrates two lumped-parameter models: one for the eye and one for the brain. The ocular model comprises six compartments that govern intraocular pressure (IOP) and ocular volume dynamics, and it requires three input variables: intracranial pressure (ICP), arterial pressure, and venous pressure at the eye level. The latter two pressures, taken at the internal carotid and dural venous sinus respectively, are influenced by changes in body tilt through the hydrostatic pressure gradient induced by the vertical distance between the eye and

the mid-coronal plane. Figure 3.2 schematically illustrates the lumped-parameter model of the cerebral, extracerebral and ocular circulation, according to [5]. In particular, the ocular compartment is shown in detail in the lower part of the image.

The **cerebral circulation** is represented by a lumped model of the major arteries forming the Circle of Willis, which branch into intracerebral arterioles and the right and left pial networks. These distal compartments—anterior, middle, and posterior—are interconnected via cortical collateral vessels. Cerebral autoregulation and CO_2 reactivity mechanisms adjust compliance and resistance within the pial vasculature to maintain stable cerebral perfusion. A single capillary–venous compartment completes the cerebral circulation. Intracranial pressure (ICP) is governed by cerebrospinal fluid dynamics and gravitational hydrostatic effects via a non-linear compliance relation. The outflow from the cerebral model drains into the superior vena cava, together with blood from the arms, extracerebral head circulation, and ocular vasculature.

The coronary microcirculation is also modeled through a dedicated 0D circuit, which is connected to the large coronary arteries represented in 1D. The **heart and pulmonary circulations** are described through lumped 0D models comprising the four cardiac chambers, cardiac valves, and pulmonary vessels. A time-varying elastance model is used to represent atrial and ventricular contraction, while cardiac valves are modeled as non-ideal diodes to capture their resistive and directional flow characteristics. These compartments are influenced by intrathoracic pressure (ITP), which varies with posture and gravity to simulate diaphragm movement and its impact on hemodynamics during tilt-induced postural changes. Specifically, a constitutive equation can be formulated to describe the mechanical behavior of the four cardiac chambers under the influence of ITP:

$$p_{ch} = E_{ch}\left(V_{ch} - V_{ch}^{un}\right) + ITP\,, \tag{3.5}$$

where $p_{ch} - ITP$ represents the cardiac transmural pressure, related to the stressed volume $V_{ch} - V_{ch}^{un}$ through the elastance function E_{ch}. Furthermore, the following analytical expression for ITP is adopted, which takes into account postural and gravity changes ($g_0 = 9.81\,m/s^2$):

$$ITP = -4.014 + 1.127\frac{g}{g_0} + 0.895\left(\frac{g}{g_0}\right)^2 \sin\alpha - 4.508\frac{g}{g_0}\sin\alpha\,, \tag{3.6}$$

On the other hand, the following equations govern pulmonary arterial and venous compartments:

$$\frac{dp_j}{dt} = \frac{Q_{j-1} - Q_j}{C_j} + \frac{dITP}{dt}\,, \tag{3.7}$$

$$Q_j = \frac{p_j - p_{j+1}}{R_j}\,, \tag{3.8}$$

where j-1 indicates the *pulmonary valve* and j+1 the *pulmonary veins* when j = pa (pulmonary arteries), while j-1 stands for *pulmonary arteries* and j+1 for *left atrium* when j = pv (pulmonary veins).

Finally, **autonomic regulation** is incorporated through baroreflex and cardiopulmonary reflex mechanisms to control short-term blood pressure variations in response to postural transitions and gravitational changes. These reflexes are modeled using two distinct sigmoid functions: the baroreflex is driven by mean aortic–carotid sinus pressure, whereas the cardiopulmonary reflex depends on central venous pressure (CVP). The baroreflex adjusts peripheral vascular resistance and venous tone and modulates inotropic and chronotropic responses in both ventricles. In contrast, the cardiopulmonary reflex exclusively affects peripheral vascular resistance.

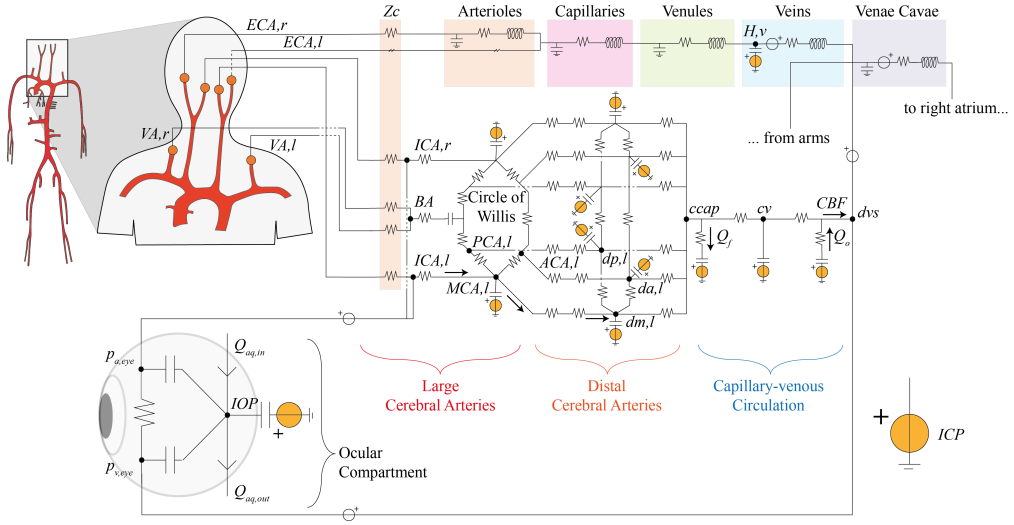

Figure 3.2: Schematic representation of the lumped-parameter model of the cerebral, extracerebral and ocular circulation- Fois et al. (2024). The figure represents the arterial and venous extracerebral circulation, which departs from the External Carotid Arteries (ECA), and the cerebral circulation which departs from the Vertebral Arteries (VA) and Internal Carotid Arteries (ICA), converging into the Circle of Willis, which distributes blood flow into large cerebral arteries (red), distal cerebral arteries (orange), and the capillary–venous circulation (blue). The lower part shows in detail the ocular compartment.

3.1 Mathematical Model of the 1D Arterial Tree

Focusing on the representation of the arterial tree, it is modeled as a network of 63 tapered vessels that reproduce the anatomical arterial bifurcations (see Figure 3.1). From a mathematical standpoint, this constitutes a distributed model that enables a one-dimensional analysis. The axial vessel coordinate (x) and time (t) are considered independent variables, while cross-sectional area A(x,t), pressure p(x,t), and blood flow rate Q(x,t) are the dependent variables. Each arterial vessel is divided into a number (N_v) of small cylindrical segments. The solution, in terms of local pressure and flow rate signals, is computed for each vessel segment.

The mathematical formulation involves a set of hyperbolic partial differential equations that account for a greater level of geometrical and viscoelastic detail compared to a lumped-parameter (0D) approach. The one-dimensional form of the incompressible blood flow equations also enables the modeling of pulse wave propagation while ensuring a reasonable computational cost. The governing equations include the one-dimensional axisymmetric form of the Navier–Stokes equations for mass and momentum conservation, and a constitutive law for blood (transmural) pressure p(x,t) that closes the system.

$$\frac{\partial A}{\partial t} + \frac{\partial Q}{\partial x} = 0 \tag{3.9}$$

$$\frac{\partial Q}{\partial t} + \frac{\partial}{\partial x}\left(\beta \frac{Q^2}{A}\right) + \frac{A}{\rho}\frac{\partial p}{\partial x} - N_4 \frac{Q}{A} - Ag \sin\gamma \sin\alpha = 0 \tag{3.10}$$

$$p(x,t) = f(A(x,t)) \tag{3.11}$$

The large lumen characteristic of conduit arteries justifies modeling blood as a Newtonian fluid, with constant density set to $\rho = 1050\ kg/m^3$ and dynamic viscosity $\mu = 0.004\ Pa{\cdot}s$. The Coriolis coefficient and the viscous coefficient N_4 are evaluated assuming a flat–parabolic velocity distribution across the cross-sectional area of each vessel. Gravitational effects are incorporated into the mass and momentum balance equations via the term $g\,sin\gamma\,sin\alpha$, where g denotes gravitational acceleration, γ is the vessel orientation relative to the frontal–transverse body axis, and α is the vessel inclination relative to the horizontal reference plane. The constitutive equation expressing transmural blood pressure as a function of local vessel area is reported in Appendix A .

At vessel bifurcations, mass and total pressure conservation are imposed at both inlet and outlet sections, leading to the following equations:

$$\begin{cases} Q_{in} = Q_{out,1} + Q_{out,2} \\ p_{in} + \frac{1}{2}\rho\left(\frac{Q}{A}\right)^2_{in} = p_{out,1} + \frac{1}{2}\rho\left(\frac{Q}{A}\right)^2_{out,1} = p_{out,2} + \frac{1}{2}\rho\left(\frac{Q}{A}\right)^2_{out,2} \end{cases}$$

Subscripts *in, out,1*, and *out,2* refer to the parent vessel and its two daughter vessels, respectively (three daughter vessels in the case of coronary bifurcations).

At the terminal connections of the 1D arterial system, the inlet of the proximal aorta is coupled to a 0D model of the aortic valve, while each terminal 1D distal artery is connected to a 0D arteriolar compartment via a set of lumped characteristic impedances.

Operationally, each arterial vessel is uniquely identified by a number and associated with a set of properties: length, inlet diameter, outlet diameter, wall thickness, and orientation relative to the frontal–transverse body axis.

3.2 Evaluation methods for Wave Speed and Impedance

Operatively, the evaluation of characteristic impedance and wave speed can be carried out using a local approach, starting from the solution of the 1D mathematical model. In particular, the adoption of the local so-called PU-Loop and PQ-Loop methods involves the use of numerical results in terms of pressure and flow rate signals associated with each individual segment of each 1D arterial vessel. The PU-Loop method consists in extracting the linear slope of the pressure-velocity relation during the early-systolic phase, which corresponds to the product ρc according to the water hammer equation. The relatively linear trend of this PU-Loop portion is due to a unidirectional forward wave, under the assumption of a negligible backward wave contribution in the initial phase of the cardiac cycle. As the PU-Loop evolves, the P–U relation deviates from linearity when reflected waves become significant. Once the slope of the linear phase is identified, dividing it by the blood density yields the local wave speed. Recalling the relation between the pressure and flow rate signals (2.19), in the absence of backward waves, the PQ-Loop can be introduced. This method allows for the identification of the local characteristic impedance for each segment of every single arterial vessel, which directly corresponds to the slope of the linear phase in the P–Q relation.

To illustrate the analytical procedure of wave decomposition applied across all arterial sites and gravitational conditions, a few representative cases are briefly presented. Specifically, three gravitational conditions (0G, 1G, and 3G) and two representative vessels were selected: one from the central region (the aortic root) and one from the peripheral region (the anterior tibial artery). It is important to

underline that each arterial vessel within the model is further subdivided into a sequence of segments, each characterized by its own solution in terms of pressure and flow rate waveforms over a single cardiac cycle. For each segment, the corresponding PU and PQ-Loops are reported below (see Figures 3.3, 3.4, 3.5, 3.6), and the slope of the linear portion of each loop is evaluated. In the PU and PQ-Loop plots, the red lines highlight the approximately linear segments, from which the angular slope was manually calculated. These slopes are then used to calculate the wave speed and characteristic impedance of each segment. Once these quantities are obtained for all segments associated to the two arterial vessels, an averaging operation is performed to derive the mean values of c and Z_c over each entire vessel (Tab. 3.1 and Tab. 3.2). These averaged values can then be used to perform the wave decomposition.

As a first step, the PQ and PU-Loops corresponding to the two segments of the aortic root are presented (see fig. 3.3, 3.4). For each loop, a red line highlights the nearly linear portion of the curve. This line has been manually fitted by identifying the longest segment that reliably represents a linear regression, aimed at approximating the local characteristic impedance (from the PQ-Loops) and the wave speed (from the PU-Loops). For the sake of completeness, the table 3.1 reports the numerical values extracted from the linear slopes of each loop referred to every single segment, along with the average value computed over the entire vessel, both in terms of characteristic impedance Z_c and wave propagation speed c.

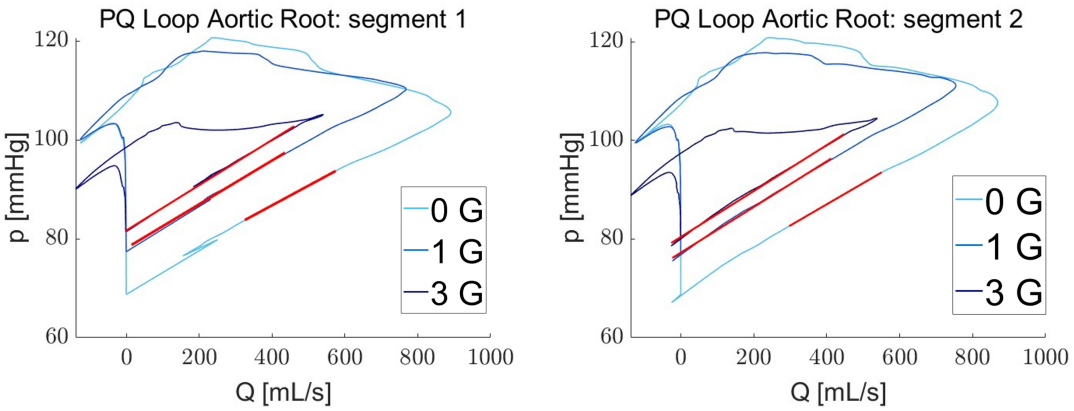

Figure 3.3: PQ-Loops at the aortic root under different gravity conditions: 0G (light blue), 1G (blue) and 3G (dark blue). Being the aortic root divided into two consecutive segments, the figure separately displays the PQ-Loops corresponding to each section (left and right). Red lines indicate the approximately linear portions in each loop, whose slope corresponds to the local characteristic impedance.

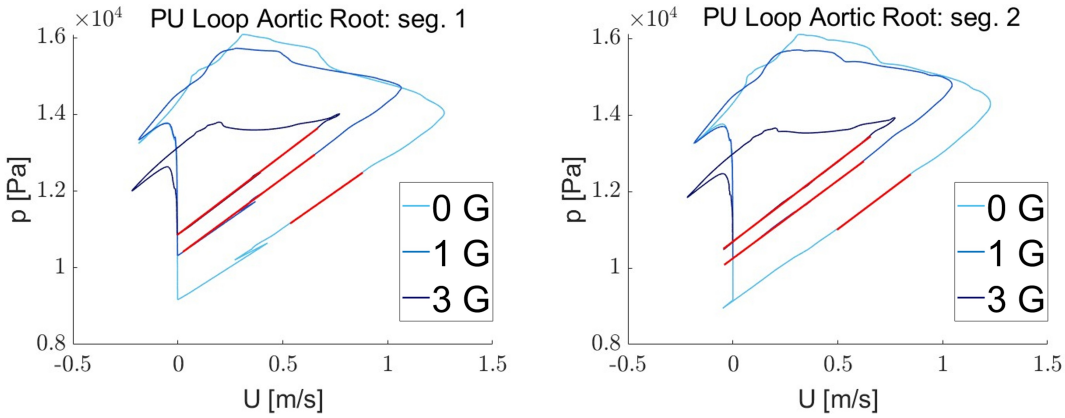

Figure 3.4: PU-Loops at the aortic root under different gravity conditions: 0G (light blue), 1G (blue) and 3G (dark blue). Being the aortic root divided into two consecutive segments, the figure separately displays the PU-Loops corresponding to each section (left and right). Red lines indicate the approximately linear portions in each loop, whose slope corresponds to the local product ρc.

	Z_c $[mmHg \cdot s/mL]$			c $[m/s]$		
	1° seg.	**2° seg.**	**mean**	**1° seg.**	**2° seg.**	**mean**
0 G	0.0398	0.0430	0.0414	3.6528	3.9303	3.7915
1 G	0.0442	0.0463	0.0453	3.8446	3.8786	3.8616
3 G	0.0458	0.0466	0.0462	3.9600	3.9910	3.9755

Table 3.1: Characteristic impedance (Z_c) and wave speed (c) values in the aortic root obtained using the local PQ and PU-Loop methods under four different gravity conditions.

Subsequently, the PQ and PU-Loops are shown for different segments of the anterior tibial artery, which is composed of 10 consecutive sections progressing toward the periphery (see fig. 3.5, 3.6). This additional example allows to illustrate the impedance and wave speed extraction method not only in the central region of the arterial network (as for the aortic root), but also at the level of a peripheral vessel (e.g. aterior tibial artery). Notably, as one moves distally along the arterial tree, both PQ and PU-Loops corresponding to different gravitational conditions become increasingly separated from each other.

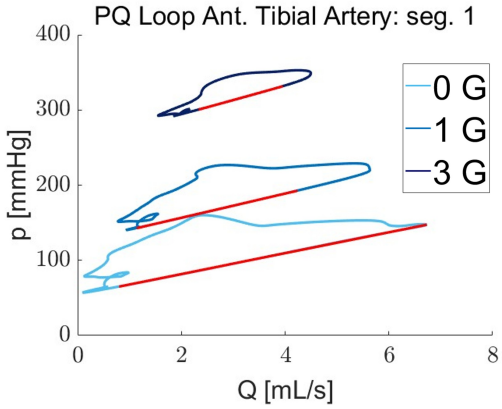
PQ Loop Ant. Tibial Artery: seg. 1
p [mmHg]
Q [mL/s]
0 G
1 G
3 G

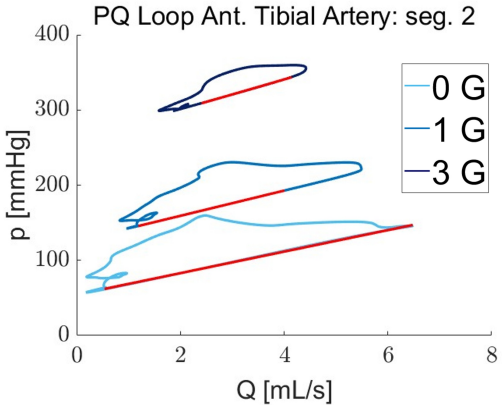
PQ Loop Ant. Tibial Artery: seg. 2
p [mmHg]
Q [mL/s]
0 G
1 G
3 G

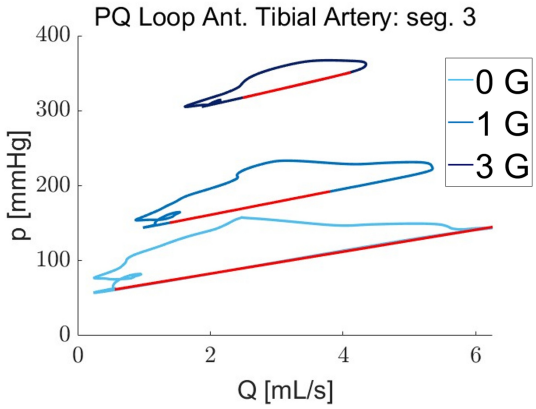
PQ Loop Ant. Tibial Artery: seg. 3
p [mmHg]
Q [mL/s]
0 G
1 G
3 G

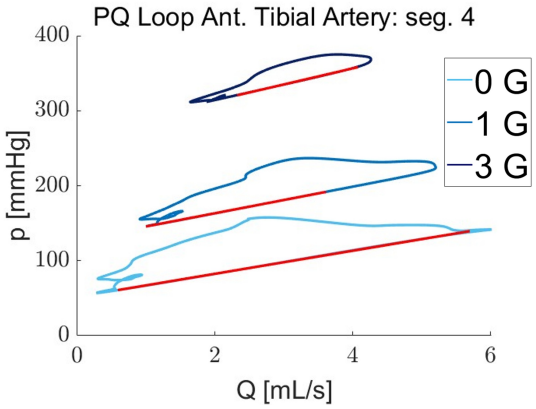
PQ Loop Ant. Tibial Artery: seg. 4
p [mmHg]
Q [mL/s]
0 G
1 G
3 G

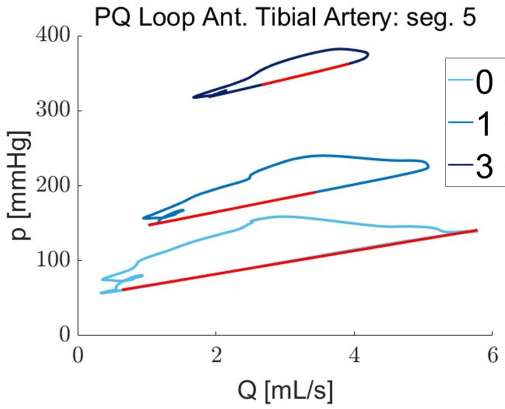
PQ Loop Ant. Tibial Artery: seg. 5
p [mmHg]
Q [mL/s]
0 G
1 G
3 G

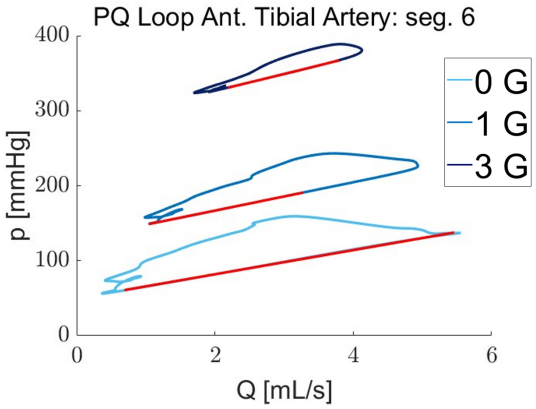
PQ Loop Ant. Tibial Artery: seg. 6
p [mmHg]
Q [mL/s]
0 G
1 G
3 G

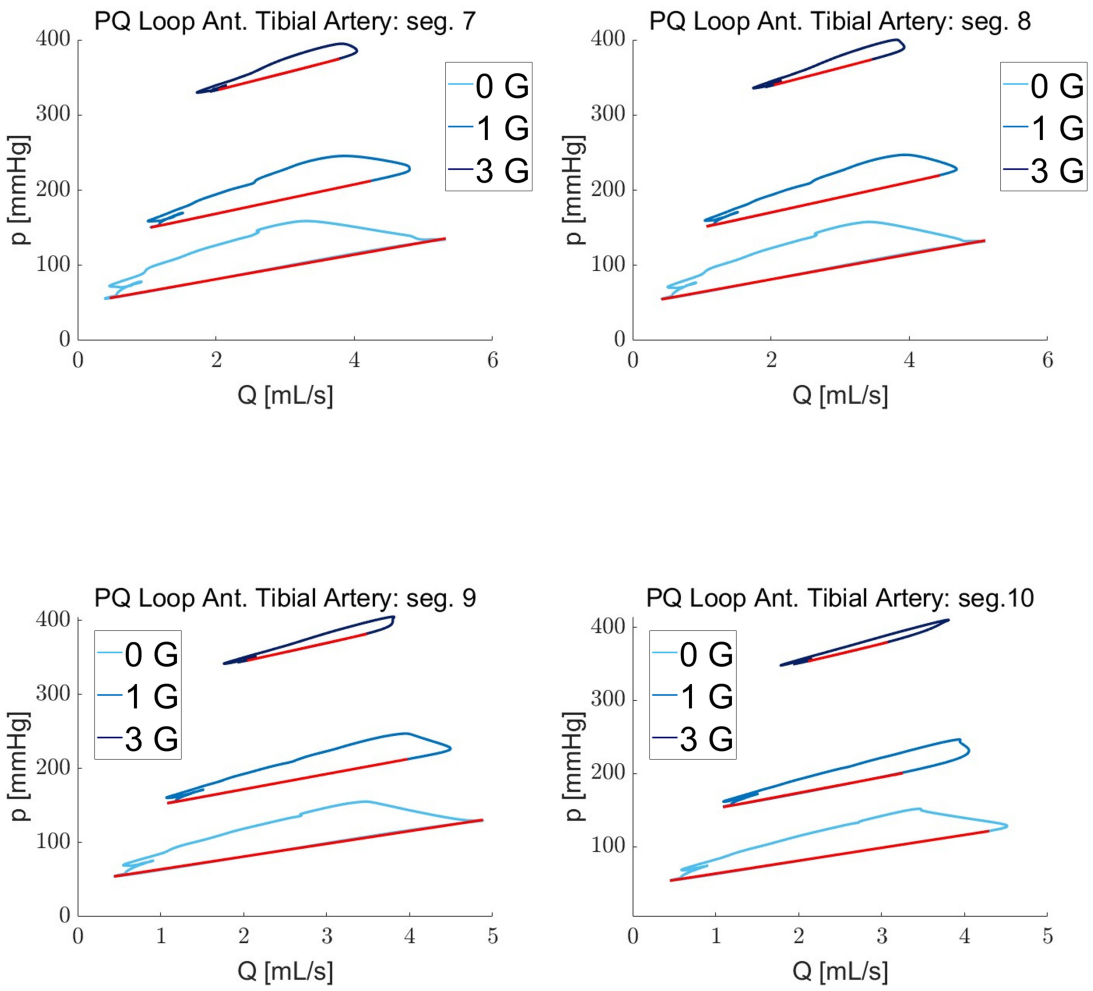

Figure 3.5: PQ-Loops at the anterior tibial artery under different gravity conditions: 0G (light blue), 1G (blue) and 3G (dark blue). Being the ant. tibial artery divided into ten consecutive segments, the figure separately displays the PQ-Loops corresponding to each section. Red lines indicate the approximately linear portions in each loop, whose slope corresponds to the local characteristic impedance.

In contrast to the case of the aortic root—where the loops associated with 0G, 1G, and 3G exhibit a substantial degree of overlap for each segment—in the anterior tibial artery, the overlap area among loops at different g-levels is nearly negligible. Furthermore, a progressive flattening of the PQ and PU-Loops is observed with increasing distance from the heart. In particular, the loops tend to become more regular, reflecting a reduced complexity in the pressure-flow interaction at the level of peripheral vasculature compared to central arteries.

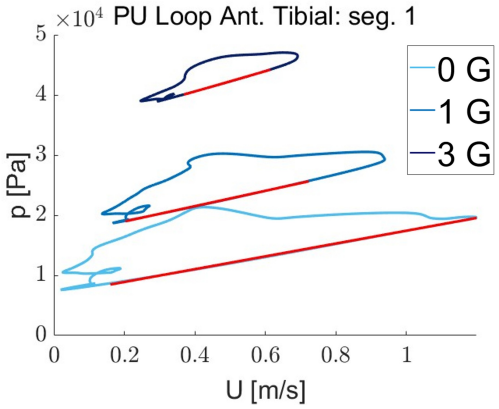
×10^4 PU Loop Ant. Tibial: seg. 1
p [Pa]
U [m/s]
0 G
1 G
3 G

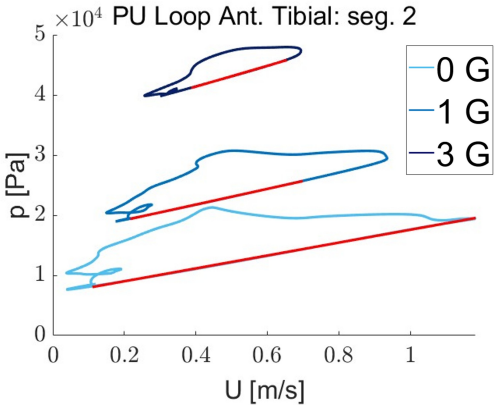
×10^4 PU Loop Ant. Tibial: seg. 2
p [Pa]
U [m/s]
0 G
1 G
3 G

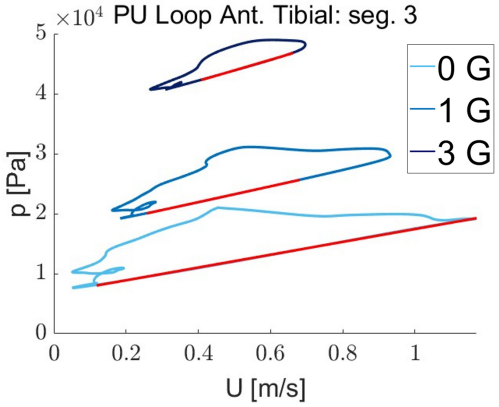
×10^4 PU Loop Ant. Tibial: seg. 3
p [Pa]
U [m/s]
0 G
1 G
3 G

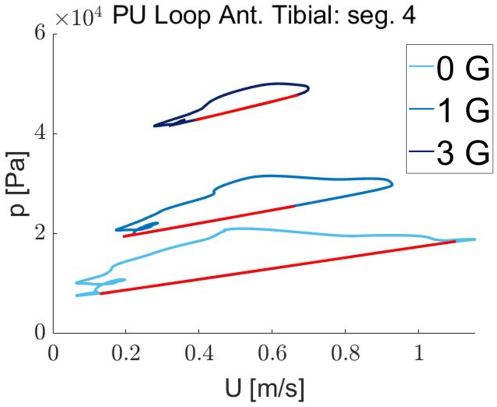
×10^4 PU Loop Ant. Tibial: seg. 4
p [Pa]
U [m/s]
0 G
1 G
3 G

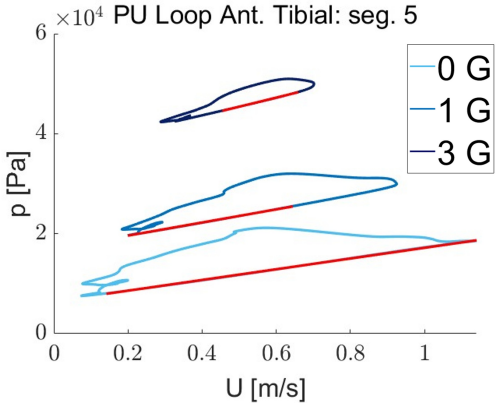
×10^4 PU Loop Ant. Tibial: seg. 5
p [Pa]
U [m/s]
0 G
1 G
3 G

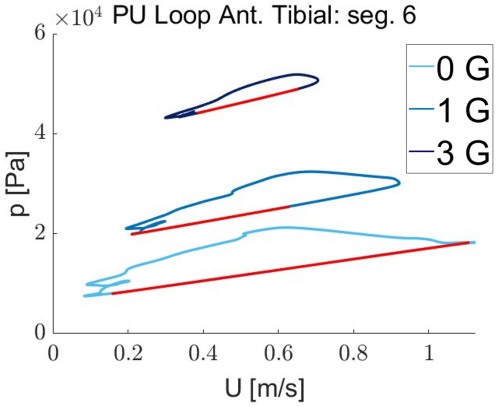
×10^4 PU Loop Ant. Tibial: seg. 6
p [Pa]
U [m/s]
0 G
1 G
3 G

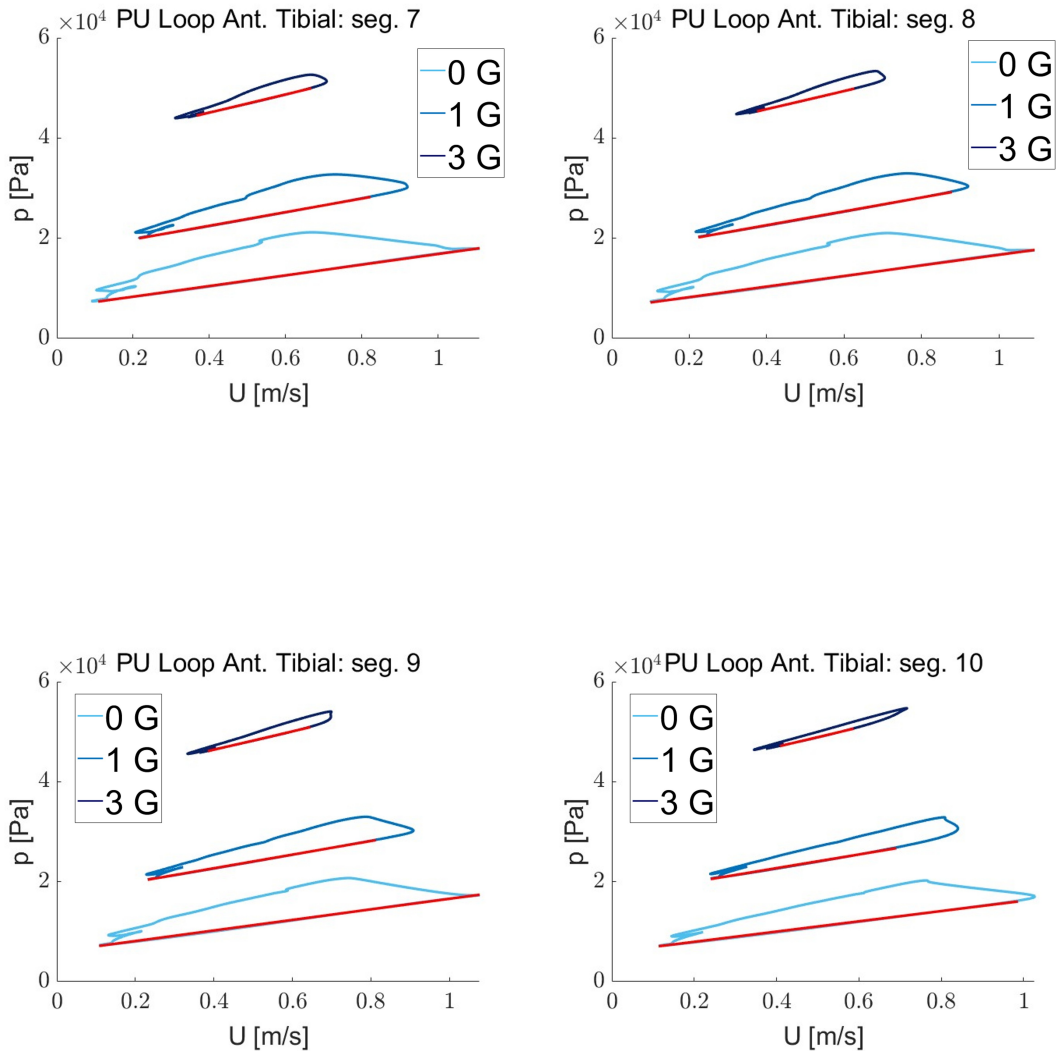

Figure 3.6: PU-Loops at the anterior tibial artery under different gravity conditions: 0G (light blue), 1G (blue) and 3G (dark blue). Being the ant. tibial artery divided into ten consecutive segments, the figure separately displays the PU-Loops corresponding to each section. Red lines indicate the approximately linear portions in each loop, whose slope corresponds to the local product ρc.

Finally, the table 3.2 reports the numerical values extracted from the linear slopes of each loop referred to every single segment, along with the average value computed over the entire vessel, both in terms of characteristic impedance Z_c and wave propagation speed c.

	$Z_c\ [mmHg \cdot s/mL]$										
	Seg 1	**Seg 2**	**Seg 3**	**Seg 4**	**Seg 5**	**Seg 6**	**Seg 7**	**Seg 8**	**Seg 9**	**Seg 10**	**Mean**
0 G	13.89	14.31	14.63	15.40	15.52	16.10	16.34	16.74	17.21	17.62	15.77
1 G	16.09	16.76	17.28	17.64	18.21	18.81	19.47	20.17	20.59	21.42	18.64
3 G	19.16	19.95	20.74	21.45	22.23	22.63	23.44	23.92	24.91	27.09	22.55
	$c\ [m/s]$										
	Seg 1	**Seg 2**	**Seg 3**	**Seg 4**	**Seg 5**	**Seg 6**	**Seg 7**	**Seg 8**	**Seg 9**	**Seg 10**	**Mean**
0 G	10.15	10.20	10.17	10.28	10.21	10.28	10.14	10.05	10.06	9.77	10.13
1 G	12.16	12.41	12.54	12.37	12.48	12.59	12.93	13.13	12.96	13.01	12.66
3 G	16.07	16.49	16.82	17.02	17.30	17.12	17.31	17.18	17.48	18.51	17.13

Table 3.2: Characteristic impedance (Z_c) and wave speed (c) values in the Anterior Tibial Artery obtained using the local PQ and PU-Loop methods under different gravity conditions.

Chapter 4

Primary Central Responses to Varying Gravity Conditions

The aim of this section is to provide a comprehensive overview of how the cardiovascular system adapts to changes in gravitational acceleration, with a particular emphasis on central haemodynamic and mechano-energetic parameters. The discussion is largely informed by the study of Tripoli et al. (2025)[12], which investigates cardiac function within the [0G–3G] gravity range—exactly in line with the conditions explored in the present thesis. Notably, the authors employ a validated 0D–1D multiscale cardiovascular model that closely resembles the computational framework described in Chapter 3.

It is well established that gravitational shifts induce profound alterations in the distribution of body fluids and in cardiovascular regulation. In the standing position, decreasing gravity levels toward microgravity (0G) elicit a cephalad fluid shift, consisting in a redistribution of blood and cerebrospinal fluid from the lower to the upper body. In the case of long-term 0G exposure, microgravity-induced unloading of the cardiovascular system promotes cardiac atrophy, hypovolemia, and a reduction in aerobic capacity, all hallmarks of cardiovascular deconditioning. This phenomenon leads also to an increase in intracranial pressure (ICP) and it is currently considered a major contributor to the spaceflight-associated neuro-ocular syndrome (SANS)—a condition that may cause potentially irreversible visual impairment in astronauts after prolonged exposure to microgravity. Conversely, in hyper-gravity conditions ($G > 1$), the gravitational vector promotes a caudal fluid shift, leading to increased venous pooling in the lower extremities. This results in reduced venous return, elevated orthostatic stress, and potential cerebral

hypoperfusion. It is important to underline that, in both extremes of the gravity spectrum, short-term cardiovascular compensation relies on rapid adjustments in vascular tone and autonomic regulation, as it will be later discussed.

First, it is essential to introduce the definitions of the main central mechano-energetic parameters, which are fundamental for describing the cardiovascular system's response to gravitational variations. For greater clarity, figure 4.1 illustrates the Pressure-Volume Loop of the left ventricle, highlighting some of the main mechano-energetic cardiac parameters, as well as the systolic and diastolic phases associated with the opening and closing of the mitral and aortic valves.

- **RR (R-R interval)** [s]
  It represents the duration of a single cardiac cycle, corresponding to the time interval between two consecutive R-waves in the electrocardiogram (ECG);
- **HR (Heart Rate)** [beats/min]
  It represents the number of heartbeats per minute: $HR = \frac{60}{RR}$;
- **SV (Stroke Volume)** [mL/beat]
  It represents the volume of blood ejected by a ventricle during a single cardiac cycle:

  $$SV = EDV - ESV$$

  where EDV is end-diastolic volume and ESV is end-systolic volume [mL];
- **CO (Cardiac Output)** [L/min]
  It represents the total volume of blood pumped by the heart per minute:

  $$CO = SV \cdot HR$$

- **EF (Ejection Fraction)** [-]
  It represents the fraction of the end-diastolic volume ejected during systole and it is a dimensionless indicator of ventricular contractility:

  $$EF = \frac{SV}{EDV}$$

- **EW (External Work)** [J]
  It represents the mechanical work performed by the ventricle per beat and correspond to the area enclosed by the pressure–volume (PV) loop:

  $$EW = \oint p \, dV$$

- **RPP (Rate-Pressure Product)** [mmHg/min]
  It represents an index of myocardial oxygen consumption, defined as the product of heart rate and systolic arterial pressure:

$$RPP = HR \cdot p_{sys}$$

- **TTI/min (Tension-Time Index per minute)** $[mmHg \cdot s/min]$
  It represents a proxy for the oxygen demand of the myocardium, calculated as the integral of left ventricular pressure over the duration of systole, normalized per minute:

$$TTI/min = \int_{RR} p_{LV}(t)dt \cdot HR$$

- **LVE / RVE (Left/Right Ventricular Efficiency)** [-]
  They represent the mechanical efficiency of the left and right ventricle, defined as the ratio between useful work and total ventricular energy cost (external work plus potential energy):

$$LVE = \frac{EW_{LV}}{EW_{LV}+PE_{LV}} \qquad RVE = \frac{EW_{RV}}{EW_{RV}+PE_{RV}}$$

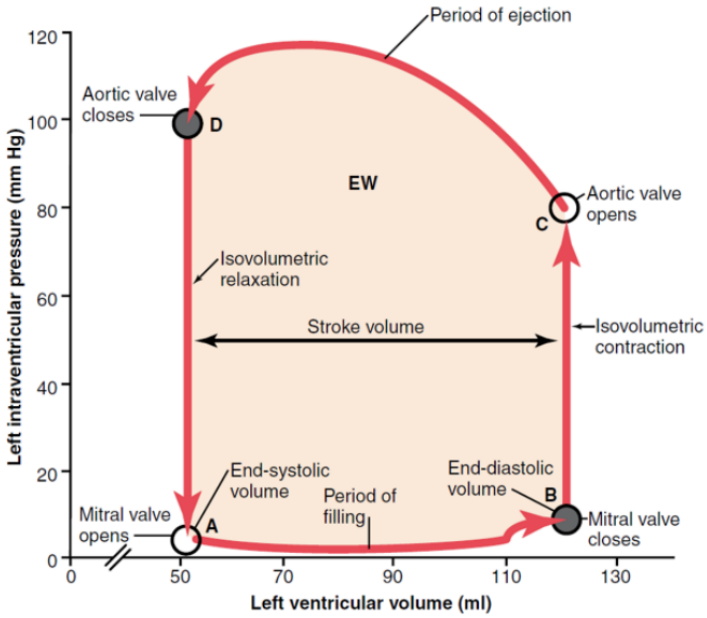

Figure 4.1: Left Ventricular Pressure-Volume Loop. Lecture slides from the "Biofluidodinamica e medicina spaziale" course, Prof. S. Scarsoglio, Politecnico di Torino, a. y. 2024/2025.

In terms of short-term adaptation, the study by Tripoli et al. (2025) sheds new light on the influence of gravity changes on key mechano-energetic cardiac metrics, along with indices of myocardial oxygen consumption. Specifically, the study highlights distinct ventricular responses across the gravity spectrum, as it is shown in the figure 4.2 (A e B) [12], where the right and left ventricles Pressure-Volume Loops are illustrated for different gravity conditions (0G, 1G, 2G and 3G). Under microgravity, the left ventricle (LV) exhibits improved preload and reduced afterload, resulting in increased stroke volume (SV), elevated ejection fraction (EF), and greater efficiency (LVE). The pressure-volume loop (PV loop) of the LV widens and shifts rightward, indicative of augmented contractile performance. In contrast, under hypergravity, preload decreases sharply due to impaired venous return, leading to reduced end-diastolic volume (EDV) and stroke work, with a consequent decline in efficiency. The LV PV loop compresses, signifying an energetic deficit. The right ventricle (RV) displays even greater sensitivity. As G increases from 0G to 3G, the end-systolic pressure (ESPrv) falls by approximately 85%, and RV external work (EWrv/min) drops by 33.5%. Yet, the RV efficiency (RVE) remains relatively stable, suggesting a proportional reduction in both energy supply and potential energy. From an energetic standpoint, myocardial oxygen demand, estimated via rate-pressure product (RPP) and tension-time index (TTI/min), increases with G. However, the energy delivered by ventricular contraction (EW/min) does not rise proportionally, particularly in the LV. This mismatch between oxygen demand and mechanical energy supply becomes particularly evident under hypergravity and reflects a state of suboptimal cardiac performance and heightened stress.

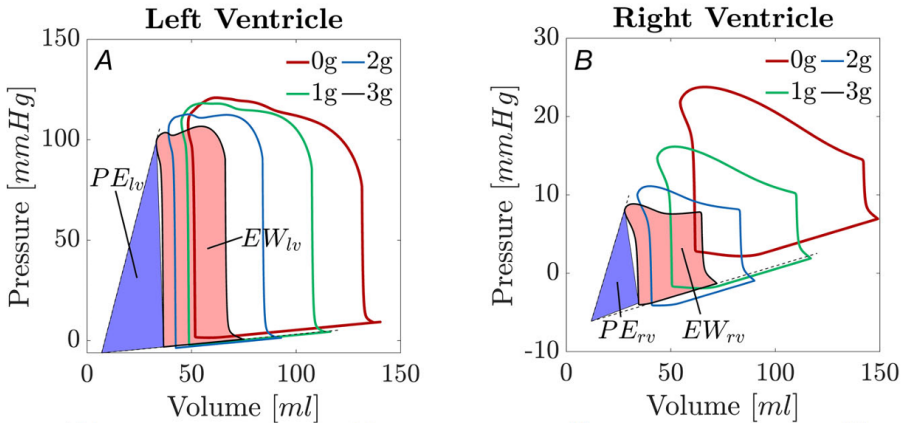

Figure 4.2: Tripoli et al. (2025)[12]. Right and left ventricles Pressure-Volume Loops under four different gravity conditions: 0G (red), 1G(green), 2G(blue) and 3G(black). $PE_{lv/rv}$ denotes the potential energy associated with the mechanical action of the left/right ventricle, while $EW_{lv,rv}$ represents the external work performed by the left/right ventricle during one cardiac cycle.

Coronary perfusion is also significantly affected by gravitational changes. The stroke volumes in both the left anterior descending artery (LAD) and the right coronary artery (RCA) initially increase between 0G and 0.5G, where a peak value is observed. Beyond 0.5G, however, both stroke volumes exhibit a sharp decline, as a consequence of the increased heart rate (HR). Over the entire range of gravitational acceleration, total coronary blood flow (CBF) increases as a result of baroreflex-mediated tachycardia (chronotropic effect). Nevertheless, this nonlinear increase in CBF does not match the concurrent rise in myocardial oxygen demand, especially at higher G-levels, leading to a potential imbalance between metabolic supply and demand. In particular, at higher gravitational levels, diastolic duration (RR_{dia}) shortens more markedly than the systolic phase (RR_{sys}), decreasing from 59.8% to 43.3% of the total cardiac cycle (RR) as gravity increases from 0G to 3G. Since coronary blood flow predominantly occurs during diastole, the reduction in RR_{dia}/RR_{sys} ratio indicates a more restricted temporal window for effective coronary perfusion despite the overall shortening of the cardiac cycle (RR) induced by HR increase under hypergravity conditions. Specifically, the diastolic-to-systolic coronary flow ratio (SV_{dia}/SV_{sys}) decreases from 3.7 at 0G to 1.7 at 3G in the LAD, signalling an altered supply pattern unfavourable to myocardial tissue. Despite an increase in coronary perfusion pressure (CPP)—driven by elevated diastolic aortic pressure (DAP)—the imbalance persists. Ultimately, the energy supply–demand mismatch extends to the coronary level, reinforcing the evidence of myocardial stress under hypergravity.

Regarding central pressures, the mean aortic pressure ($\overline{p_{aa}}$) slightly increases from 0G to 1G (with a variation ranging between the values 92 mmHg and 96.2 mmHg), then stabilizes or slightly decreases at higher g, reaching the value of 92 mmHg again. However, pulsatile amplitude of Paa decreases by 55.5% as G rises from 0G to 3G, consistent with reduced SV. In contrast, central venous pressure (CVP), pulmonary artery pressure (p_{pa}), and pulmonary capillary wedge pressure (PCWP) all exhibit a monotonic and non-linear decrease across the same range, largely due to the downward displacement of the diaphragm and the consequent reduction in intrathoracic pressure (ITP). These pressure drops compromise pulmonary venous return and reduce right atrial filling, contributing to the deterioration of RV function in hypergravity. Interestingly, while the driving pressure of the systemic perfusion ($\overline{p_{aa}}$ - CVP) increases moderately (+13%) between 0G and 3G, the cardiopulmonary circulation driving pressure (p_{pa} - PCWP) decreases by 30%, indicating a differential regulation across the systemic and pulmonary circuits. On the contrary, the pulse values of these pressures undergo similar variation as G increases. In general, for gravitational levels below 1G, [12] reported an increase in all computed pulsatile pressure values, which is clearly associated with the concurrent increase in SV.

In an attempt to compensate for the physiological effects induced by altered gravitational acceleration, the human cardiovascular system relies on a sophisticated network of vascular regulation mechanisms and autonomic reflexes. In particular, the baroreflex and cardiopulmonary reflex play a central role in counteracting blood pooling and hypotension, helping to preserve haemodynamic stability across a wide range of gravitational conditions. In fact, [12] confirms the critical role of baroreflex and cardiopulmonary reflexes in short-term compensation. In hypergravity, these reflexes trigger systemic vasoconstriction, particularly in body regions below the heart, effectively sustaining mean arterial pressure (MAP) despite reductions in SV. The increased total peripheral resistance also contributes to maintaining systemic perfusion. Conversely, in microgravity, a sympathetic withdrawal occurs due to the cephalad fluid shift. This leads to systemic vasodilation, especially in regions below the orthostatic indifference point. The decrease in vascular tone, combined with enhanced venous return, facilitates improved ventricular filling and efficiency. These phenomena are consistent with the observed increase in cardiac efficiency and performance under short-term microgravity exposure.

In summary, variations in gravitational acceleration have a profound impact on cardiovascular function, not only in the context of long-term exposure but also in terms of acute haemodynamic response. While microgravity enhances cardiac efficiency and reduces myocardial oxygen demand, hypergravity induces mechanical and energetic inefficiencies, as well as potential haemodynamic compromise—particularly affecting right ventricular performance. The overall cardiovascular adaptation to gravitational stress is governed by a complex and dynamic interplay between cardiac preload, afterload, reflex-mediated vascular regulation, and coronary perfusion. These physiological mechanisms provide a solid foundation for the wave analysis presented in the subsequent sections, particularly for the assessment of vascular impedance and wave speed under variable gravity conditions. In fact, both wave speed and impedance are tightly linked to systemic vascular tone, and are therefore expected to be influenced by fluid shift mechanisms triggered by altered gravitational loading. In this context, the *Moens–Korteweg equation* 4.1 provides a theoretical framework to elucidate the relationships between specific geometric and mechanical properties of blood vessels and the resulting wave propagation speed in blood flow:

$$c = \sqrt{\frac{hE_{inc}}{2r_i\rho}} = \sqrt{\frac{A}{\rho C_A}} \tag{4.1}$$

where A is the vessel cross-sectional area, C_A is the area compliance, h is the vessel thickness, E_{inc} is the local stiffness, r_i is the radius and ρ is the blood density.
According to 4.1, an increase in vasoconstriction, correlated with a rise in the incremental elastic modulus (E_{inc}) of the vessel wall, is expected to lead to an

increase in local wave speed (c). Conversely, a more relaxed vascular tone would be associated with a reduced wave speed, reflecting lower vessel wall stiffness. Moreover, venous pooling, which occurs in standing posture under hypergravity due to gravity-induced caudal fluid shift, leads to an increase in venous volume. This enlargement is expected to be connected with a rise in mean transmural pressure, the magnitude of which is modulated by the local vessel compliance, defined as:

$$C = \frac{\Delta V}{\Delta p} \tag{4.2}$$

where ΔV represents the volume variation inside the vessel and Δp the corresponding change in pressure. Such changes further influence wave transmission dynamics, especially in the venous compartment, where compliance plays a dominant role.

Building upon the concepts introduced in this chapter, the following section presents and discusses the results obtained through wave analysis across varying gravitational acceleration levels, under upright posture conditions.

Chapter 5

Results

This chapter presents the results of the wave propagation analysis conducted within the framework of this study, aimed at assessing the impact of varying gravitational acceleration on signal transmission characteristics in the arterial system. The vasculature is modeled as a one-dimensional (1D) network of compliant vessels, as described in the Chapter 3, allowing for the investigation of pressure and flow wave dynamics under different gravity conditions.

The chapter opens with the analysis of total pressure and flow waveforms at selected sites along the arterial tree, for increasing values of gravitational acceleration ranging from 0G to 3G (Section 5.1). The examined locations extend from the level of the heart to the lower limbs, with the anterior tibial artery representing the most peripheral analysed vessel. This initial overview provides a qualitative insight into the global effects of gravity on wave morphology and amplitude.
Following this, the analysis illustrated in Section 5.2 focuses on two key hemodynamic parameters: characteristic impedance (Z_c) and wave speed (c), both derived using localized wave separation techniques previously described (namely, the PQ-Loop and PU-Loop methods). In this phase, the set of analyzed sites is expanded to include vessels located above the hydrostatic indifference level, specifically the right external and internal carotid arteries, in order to assess the gravitational effects on the cerebral circulation.
Once Z_c and c are estimated, the total pressure and flow waves are decomposed into their forward and backward components. Section 5.3 presents the resulting decomposed waveforms at each arterial site for all gravity levels considered, enabling the identification of reflected wave patterns and their relative contribution to the total signal.
Based on the separated wave components, wave reflection coefficients are then computed, as previously introduced in Section 2.5. Specifically, the Reflection Magnitude (RM) and Reflection Index (RI) are evaluated, and their spatial and

gravitational trends are discussed in detail to characterize the extent and distribution of wave reflections throughout the vascular network.

To allow for a rigorous and consistent comparison of waveform characteristics across different gravitational environments—particularly in light of gravity-induced variations in cardiac cycle duration—a normalization procedure is implemented. Section 5.5 outlines the normalization approach applied to the total and the decomposed waveforms, ensuring comparability of shape and phase features across all test conditions.
On the basis of the normalized data, the subsequent sections present a combined qualitative and quantitative assessment of waveform alterations, including gravity-induced changes in wave morphology and phase shift. Ad hoc metrics are introduced to quantify these variations and support objective comparisons across sites and conditions.

5.1 Gravity stress effect on Arterial Tree Total Waveforms

In the first section dedicated to the presentation of the results, the trends of total pressure and flow waves are analyzed under different gravitational conditions and at various sites along the arterial tree. Specifically, the selected sites were chosen to provide a representative overview of the central and lower-body arterial pathway, from central regions to more peripheral areas, located below the level of orthostatic indifference (i.e., the level of the heart). The arterial sites analyzed in this section are as follows: aortic root, thoracic aorta, abdominal aorta, iliac artery, femoral artery and anterior tibial artery.

The gravitational conditions investigated cover a range of gravitational accelerations from 0 G to 3 G, with increments of 0.5 G. Below, the total pressure and flow waveforms measured at the aforementioned sites are presented for the 0G, 1G, 2G, and 3G cases (see Figures 5.1, 5.2, 5.3 and 5.4). The plots show the temporal evolution of total pressure waves at the different sites over the duration of a single cardiac cycle, once steady-state conditions have been reached. It is immediately evident from the plots that, as gravitational acceleration increases, the duration of the cardiac cycle generally becomes shorter. For the sake of completeness, the table 5.1 reports the values of mean pressure and pulse pressure for all analyzed gravitational conditions.

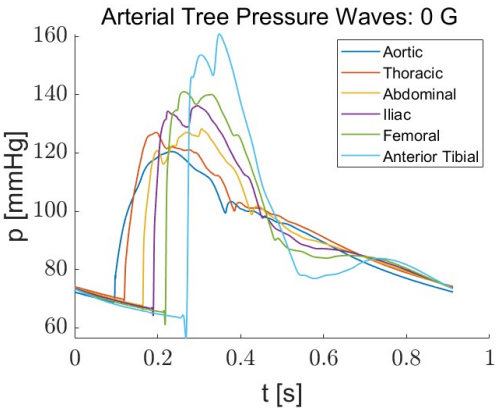

Figure 5.1: Total pressure waveforms measured at various arterial sites: 0g

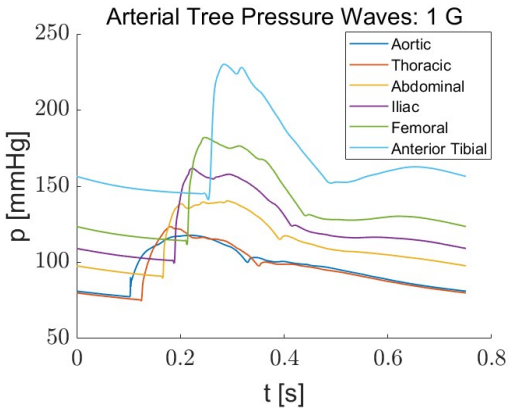

Figure 5.2: Total pressure waveforms measured at various arterial sites: 1g

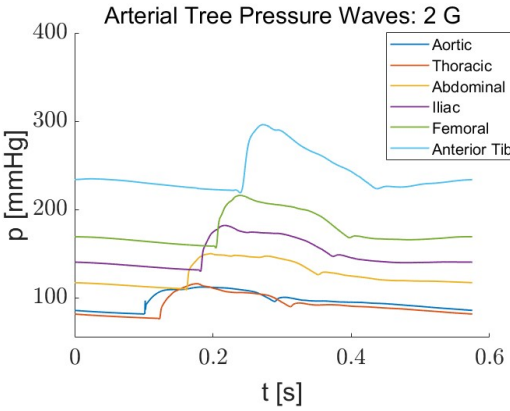

Figure 5.3: Total pressure waveforms measured at various arterial sites: 2g

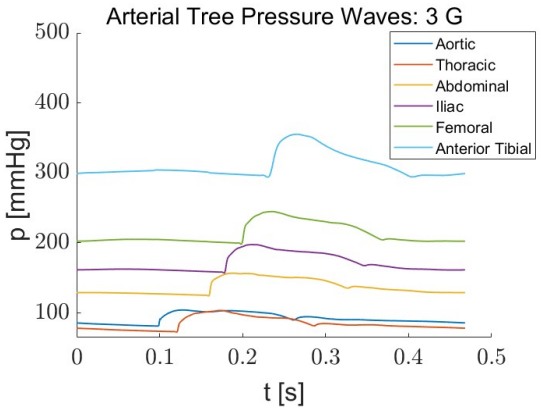

Figure 5.4: Total pressure waveforms measured at various arterial sites: 3g

The trends reported above highlight the effect of increasing G-load on pressure waves, both in terms of waveform shape and in terms of mean values and amplitudes. A qualitative observation of the waveforms immediately reveals that, as G increases, the profiles become progressively smoother, dampening the sharper variations. This smoothing effect is particularly evident at the wave peaks and feet. At the level of the aortic root, these points correspond to specific phases of the cardiac cycle related to the left ventricle, such as the ejection phase (pressure peaks) and the opening of the aortic valve (pressure wave feet). For example, observing the pressure wave in the anterior tibial artery, under 0G conditions it presents a main peak preceded by a secondary peak, which progressively merges with the main peak as G increases, eventually forming a single, regular peak at 3G. This

phenomenon also occurs in the other arterial sites analyzed and is associated with a general increase in peak values. Moreover, this variation in the maximum value of the pressure wave is not uniform along the arterial tree but becomes progressively more pronounced with increasing distance from the central region. In fact, while the anterior tibial artery exhibits a peak increase of +120.8% from 0G to 3G, the iliac artery records an increase of +45%, whereas the aortic root actually shows a decrease of -13.5%.

With regard to the wave foot, associated with the centrally induced effect of aortic valve opening—which marks the beginning of the ejection phase and the end of the isovolumetric contraction phase of the left ventricle—significant changes are observed across different sites as G varies. While in the 0G case, the downward peak of the wave foot becomes more pronounced with increasing distance from the heart, higher G-levels result in a reduced magnitude of this variation, even in the most peripheral sites. Additionally, the pressure wave minimum points exhibit a clear and global increasing trend from 0G to 3G: +18.3% at the aortic root, +144.8% at the iliac artery, and +368.5% at the anterior tibial artery. Also in this case, the percentage variation becomes more significant as the distance from the central region increases.

Mean pressure [mmHg]	**0g**	**0.5g**	**1g**	**1.5g**	**2g**	**2.5g**	**3g**
$p_{aortic\,root}$	92.21	95.75	96.22	96.41	96.18	95.11	92.14
$p_{thoracic}$	94.01	96.02	94.96	93.63	91.87	89.28	84.78
$p_{abdominal}$	92.55	103.65	111.57	119.20	126.38	132.72	137.15
p_{iliac}	92.73	109.41	122.94	136.18	148.99	160.95	170.97
$p_{femoral}$	91.78	115.67	136.35	156.74	176.71	195.82	212.99
p_{tibial}	89.59	129.69	166.87	203.90	240.53	276.33	310.19
Pulse pressure [mmHg]	**0g**	**0.5g**	**1g**	**1.5g**	**2g**	**2.5g**	**3g**
$p_{aortic\,root}$	51.74	47.58	40.42	34.75	30.58	26.57	22.96
$p_{thoracic}$	57.99	53.95	48.94	44.28	40.15	36.01	31.07
$p_{abdominal}$	62.66	58.80	51.05	45.24	41.31	37.35	32.86
p_{iliac}	72.12	67.63	62.51	57.34	52.29	46.98	40.77
$p_{femoral}$	80.13	76.03	70.59	65.11	59.72	54.07	47.01
p_{tibial}	104.51	96.95	89.05	83.41	77.26	70.19	61.31

Table 5.1: Mean and pulse pressure values at increasing gravitational acceleration along the Arterial Tree.

By examining the mean pressure values at the various sites of the arterial tree under different levels of gravitational acceleration, it can be observed that

(except for the aortic root and the thoracic torta, where mean pressure values show limited variability) there is a clear increase in mean pressure at all other sites as gravity increases. Furthermore, the percentage increase in mean pressure is more pronounced in the peripheral region (at the level of the anterior tibial artery, the percentage change from 0G to 3G is approximately +246%) compared to more central regions, such as the aAbdominal aorta (where the percentage change is about +48.2%).

With regard to pulse pressures, a clear trend of decreasing pulsatility is observed as gravitational acceleration increases, at all the arterial sites analyzed. This trend is more pronounced in the central region (the percentage decrease between 0G and 3G at the Aortic Root level is about -55.6%) compared to the peripheral region (at the level of the anterior tibial artery, the percentage variation is about -41.3%). The overall reduction in pulsatility is in line with the decrease in stroke volume, whose effect is more pronounced in the central region, compared to the periphery, where vascular tone is physiologically higher.

In light of all these considerations, it can therefore be stated that the reduction in pressure pulsatility is associated—at most sites (with the exception of the aortic root, for instance)—with a more pronounced increase in the minimum values than in the maximum values of the pressure waves. As a consequence, the range between maximum and minimum values narrows as G increases, which effectively corresponds to a reduction in pulsatility. This is also consistent with the observed increase in mean pressure values, which become progressively higher toward the periphery. In the case of the aortic root, the reduction in pulsatility is associated both with an increase in the minimum value and a decrease in the maximum value, which is also consistent with the minimal change in mean pressure between 0G and 3G.

Focusing now on the analysis of the flow rate waves, the overall waveforms corresponding to four different gravitational conditions (0G, 1G, 2G and 3G) are presented for the same arterial sites previously introduced in the analysis of pressure waves (see figures 5.5, 5.6 5.7, 5.8). Additionally, the table 5.2 reports the mean and pulsatile flow rate values associated with all the analyzed waveforms, for a range of gravitational accelerations from 0G to 3G, with a step of 0.5G.

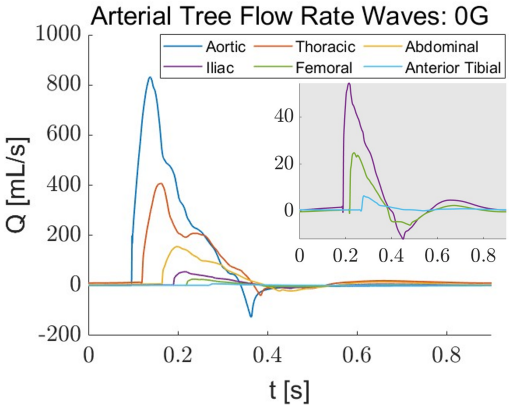

Figure 5.5: Total flow rate waveforms measured at various arterial sites: 0g

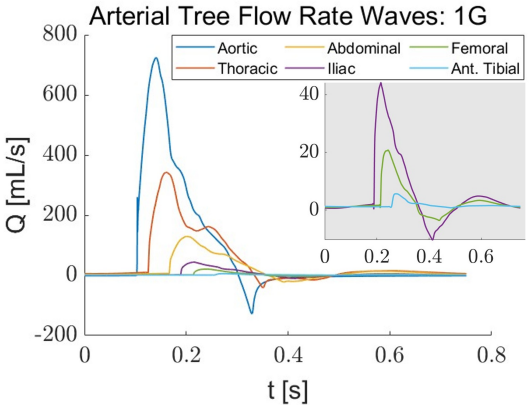

Figure 5.6: Total flow rate waveforms measured at various arterial sites: 1g

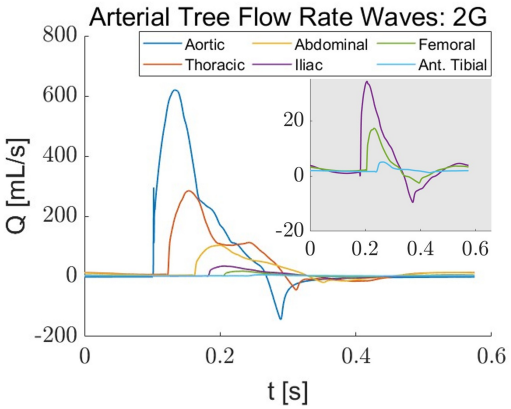

Figure 5.7: Total flow rate waveforms measured at various arterial sites: 2g

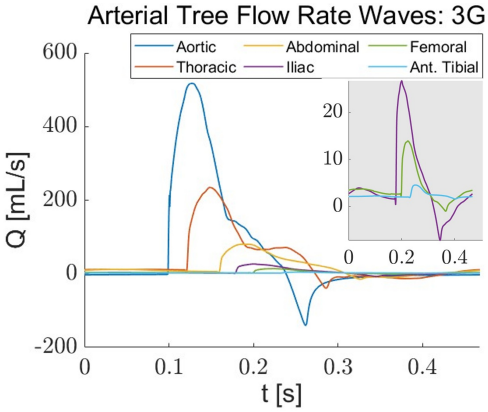

Figure 5.8: Total flow rate waveforms measured at various arterial sites: 3g

By examining the pulsatile values of the flow rate waves reported in table 5.2, it is evident that they decrease with increasing gravitational acceleration across all the sites analyzed. In particular, the extent of this reduction becomes progressively more significant with increasing distance from the central region. Indeed, while at the level of the aortic root the pulsatility of the flow rate wave decreases by -31.4% between 0G and 3G, at the level of the iliac artery the percentage reduction reaches -48.9%, and at the anterior tibial site it reaches -54%.

Conversely, the effect of increasing G on the mean values of the flow rate waves does not elicit a uniform response along the arterial tree. Specifically, in the sites analyzed between the aortic root and the iliac artery, the mean flow rate decreases

with increasing G, with percentage variations between 0G and 3G ranging from -26.2% (iliac artery) to -35.8% (thoracic aorta). In contrast, at the level of the femoral and anterior tibial arteries, the mean value increases with increasing G, with values growing toward the periphery: +80% for the femoral artery and +120% for the anterior tibial artery. It is therefore observed that, as G increases, the central and abdominal regions undergo a sort of homogeneous "emptying," leading to a reduction in arterial blood flow rate mean values, while an opposite "filling" trend is observed in the lower limbs, causing a significant increase in mean flow rate values.

The effect of varying G is also observed in terms of changes in the peak values of the flow rate waves. Specifically, all the analyzed sites show a reduction in the maximum value, which initially occurs at the level of the aortic root during the ejection phase—separating an acceleration phase from a deceleration phase of the blood flow within the aorta—and is then propagated toward the periphery. Physiologically, these values significantly decrease when considering progressively more peripheral vessels, as expected due to the branching of the arterial tree in compliance with the continuity condition. As G increases, peak values decrease at every arterial site. However, this reduction is not uniform: at the aortic root, the reduction between 0G and 3G amounts to -37.8%, becomes more pronounced at the level of the iliac artery (-51%), and then returns to approximately -30% at the level of the lower limbs (specifically in the anterior tibial artery).

Looking now at the feet of the flow rate waves, these present negative values, indicating a condition of blood backflow that physiologically occurs at the level of the aortic root following the closure of the aortic valve. This site, in fact, exhibits the lowest flow rate values—corresponding to the wave feet—compared to the other vessels, with progressively dampened and less negative values moving toward more peripheral sites. This pattern is maintained under increasing gravitational accelerations, with a slight increase in the extent of these variations. In particular, at 0G, the percentage variation between the minimum flow rate at the aortic root and that at the femoral artery is -95.3%, while at 1G it is -97.2%, and at 3G it reaches -99.3%. The anterior tibial artery is the only analyzed site to exhibit positive minimum flow rate values, although still very low, with a slightly increasing trend as G rises: from a minimum of approximately 0.037 mL/s at 0G to 1.58 mL/s at 3G. At the level of the aortic root, increasing G leads to a slight increase in the absolute value of the wave foot (which becomes more negative), whereas the sites between the thoracic aorta and the femoral artery show a slight reduction in the magnitude of the minimum value (i.e., it becomes less negative with increasing G).

Mean flow rate [mL/s]	**0g**	**0.5g**	**1g**	**1.5g**	**2g**	**2.5g**	**3g**
$Q_{aortic\,root}$	85.08	79.11	75.62	72.38	69.05	65.04	59.20
$Q_{thoracic}$	55.88	49.99	46.80	43.99	41.30	38.65	35.87
$Q_{abdominal}$	21.94	20.31	19.49	18.72	17.93	17.10	16.17
Q_{iliac}	6.33	5.86	5.62	5.40	5.19	4.96	4.67
$Q_{femoral}$	2.09	2.52	2.89	3.19	3.43	3.62	3.78
Q_{tibial}	1.07	1.38	1.65	1.88	2.07	2.23	2.35
Pulse flow rate [mL/s]	**0g**	**0.5g**	**1g**	**1.5g**	**2g**	**2.5g**	**3g**
$Q_{aortic\,root}$	959.22	911.37	852.45	808.07	763.12	721.62	658.10
$Q_{thoracic}$	447.43	421.26	383.95	352.95	329.96	307.31	274.15
$Q_{abdominal}$	177.16	169.02	151.33	136.07	123.79	110.96	95.23
Q_{iliac}	66.27	60.56	54.48	48.62	43.84	39.22	33.87
$Q_{femoral}$	30.74	27.13	24.37	22.15	19.79	17.43	14.90
Q_{tibial}	6.43	5.55	4.85	4.32	3.86	3.45	2.96

Table 5.2: Mean and pulse flow rate values at increasing gravitational acceleration along the Arterial Tree.

5.2 Gravity stress effect on Impedance and Wave Speed

At this stage, in preparation for wave separation analysis, it is necessary to compute the characteristic impedance associated with each arterial vessel under the different gravitational conditions. In addition to Z_c, the wave speed c will also be computed under the same conditions. For the purposes of the upcoming wave analysis, the set of arterial sites will now also include two vessels located above the orthostatic indifference level: the right Internal Carotid Artery (ICA-right) and the right External Carotid Artery (ECA-right).

The calculation of characteristic impedance and wave speed was carried out as previously described (see Section 3.2) for the case of the aortic root, using the PQ and PU-Loop methods, respectively. Specifically, for each vessel analyzed, local values of Z_c (and c) were calculated for each segment composing the vessel. Subsequently, the average of these segmental values was computed to obtain a single representative mean value for the entire vessel. For the sake of completeness, a more refined analysis was undertaken, encompassing the evaluation of both impedance and wave speed across an extended set of gravitational conditions. The investigation was confined to the interval between 0 G and 3 G, while adopting an incremental step of 0.1G, thereby yielding a total of 31 distinct gravitational states

considered.

First, the average values of characteristic impedance obtained for the different arterial sites under all the various gravitational conditions are reported. In Figure 5.9, reported below, each color corresponds to a specific site, allowing the reader to follow the variation of Z_c as a function of gravitational acceleration (g/g_0).

Next, the trends in terms of average wave speed (c) are reported for the same arterial sites and gravitational conditions. As before, local values of c were initially computed for each individual segment of each vessel and then averaged to yield a representative mean wave speed for the entire artery under consideration. The following figure (5.10) illustrates the obtained trend of wave speed under different gravity conditions across all the analyzed arterial sites.

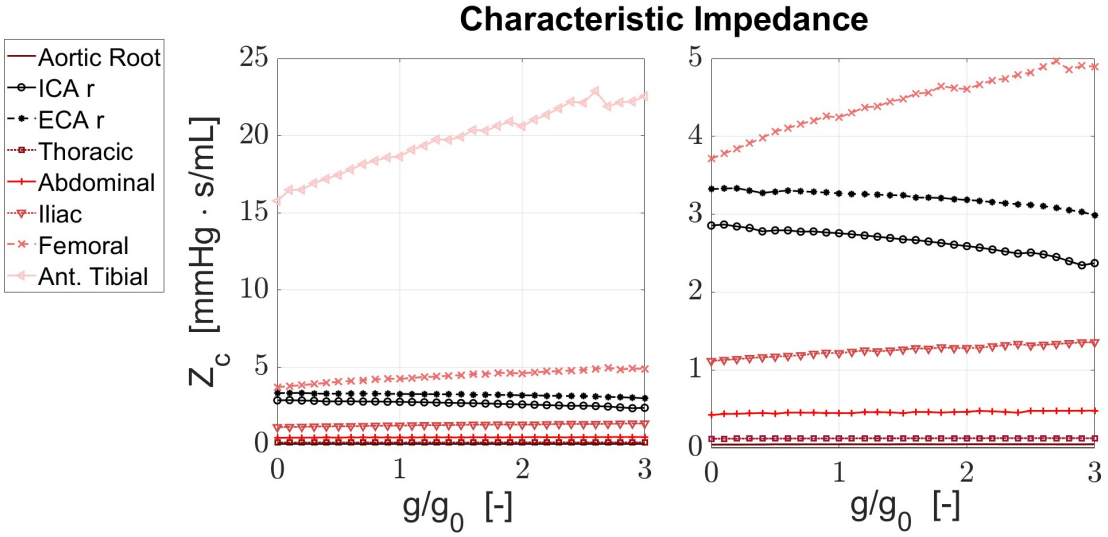

Figure 5.9: Trend of characteristic impedance (Z_c) with varying gravity across the analyzed arterial sites. Each analyzed site is associated with a distinct color. On the left, the curves corresponding to all investigated sites are shown. On the right, a zoomed-in view is provided for impedance values ranging between 0 and 5 $mmHg \cdot s/mL$.

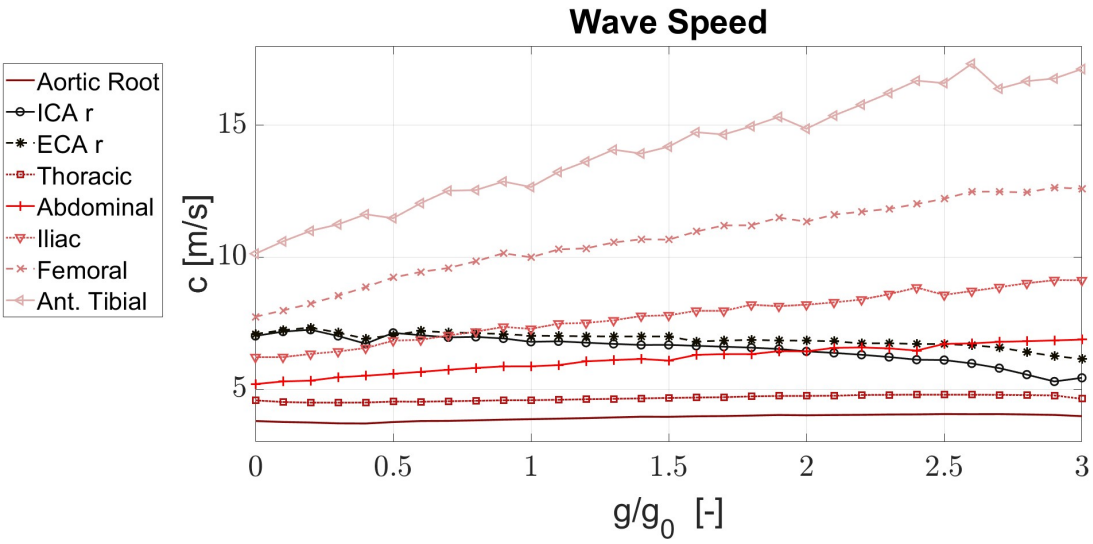

Figure 5.10: Trend of wave speed (c) with varying gravity across the analyzed arterial sites. Each analyzed site is associated with a distinct color.

Hereafter, tables 5.3 and 5.4 are provided illustrating the numerical values of characteristic impedance (Z_c) and wave speed (c), computed through the PQ and PU-Loop local Methods. For the sake of brevity, only the values associated with the 0.5G incremental steps are reported in the tables below. The last column of each table reports the percentage variation in characteristic impedance and wave speed between the aortic root (site n. 1) and the anterior tibial artery (site n. 47), computed for each gravity condition (% $Var.\ 1-47$). Conversely, the last row of each table displays the percentage variation calculated between the 0G and 3G conditions, site by site (% $Var.\ 0G-3G$).

$Z_c\ [mmHg \cdot s/mL]$	**Aortic R.**	**ICA r**	**ECA r**	**Thoracic**	**Abdom.**	**Iliac**	**Femoral**	**Ant. Tibial**	% Var. 1-47
0G	0.0414	2.8549	3.3233	0.1170	0.4216	1.1148	3.7122	15.7738	+380
0.5G	0.0453	2.7925	3.2904	0.1190	0.4396	1.1708	4.0628	17.4538	+384
1G	0.0453	2.7565	3.2677	0.1218	0.4470	1.2155	4.2448	18.6441	+410
1.5G	0.0460	2.6769	3.2414	0.1224	0.4458	1.2622	4.4807	19.9230	+432
2G	0.0461	2.5905	3.1820	0.1233	0.4628	1.2813	4.6051	20.6148	+446
2.5G	0.0455	2.5077	3.1209	0.1240	0.4755	1.3144	4.8193	22.1339	+485
3G	0.0462	2.3719	2.9858	0.1226	0.4779	1.3554	4.8957	22.5543	+487
% Var. 0G-3G	+11.6	-16.9	-10.2	+4.8	+13.4	+21.6	+31.9	+43.0	

Table 5.3: Numerical values and percentage variation of characteristic impedance Z_c at different arterial sites under distinct gravity conditions. The last column reports the percentage variation in Z_c between the aortic root (site n. 1) and the anterior tibial artery (site n. 47). The last row displays the percentage variation calculated between the 0G and 3G conditions, site by site.

$c\ [m/s]$	**Aortic R.**	**ICA r**	**ECA r**	**Thoracic**	**Abdom.**	**Iliac**	**Femoral**	**Ant. Tibial**	% Var. 1-47
0G	3.7915	7.0147	7.0904	4.5753	5.1928	6.2093	7.7423	10.1310	+167
0.5G	3.7494	7.1318	7.0486	4.5281	5.5783	6.8371	9.1589	11.4484	+205
1G	3.8616	6.7924	7.0257	4.5794	5.8639	7.2810	9.9952	12.6580	+228
1.5G	3.9510	6.6765	6.9966	4.6654	6.0817	7.7975	10.6638	14.1884	+259
2G	4.0086	6.4309	6.8367	4.7424	6.4306	8.2008	11.3449	14.8660	+270
2.5G	4.0551	6.1014	6.6599	4.7866	6.7147	8.5702	12.2140	16.5956	+309
3G	3.9755	5.4281	6.1443	4.6334	6.8767	9.1248	12.5916	17.1300	+331
% Var. 0G-3G	+4.9	-22.6	-13.3	+1.3	+32.4	+47.0	+62.6	+69.1	

Table 5.4: Numerical values and percentage variation of wave speed (c) at different arterial sites under distinct gravity conditions. The last column reports the percentage variation in c between the aortic root (site n. 1) and the anterior tibial artery (site n. 47). The last row displays the percentage variation calculated between the 0G and 3G conditions, site by site.

By examining the trends of characteristic impedance (Z_c) and wave speed (c) across different arterial sites under increasing gravitational acceleration (G), physiologically consistent patterns emerge that reflect both the structural organization of the vascular tree and the systemic regulatory mechanisms.

First, in vessels located below the level of orthostatic indifference (approximately corresponding to heart level), both Z_c and c exhibit a progressively increasing distribution along the cranio-caudal axis, from the aortic root to the anterior tibial artery. Moreover, they both show an overall increasing trend with increasing G. The former trend aligns with the physiological organization of the arterial system, where the area compliance decreases with distance from the heart, due to a gradual stiffening of more peripheral arteries. According to the Moens–Korteweg (4.1) equation, this reflects the fact that, physiologically, the reduction in area compliance with distance from the heart outweighs the concurrent decrease in cross-sectional area. Since Z_c is directly influenced by c, the increase in wave speed also leads to an increase in characteristic impedance.

This physiological decrease in arterial compliance toward peripheral districts can be interpreted as a mechanism to counteract the gravitationally induced caudal fluid shift, which leads to blood pooling in the lower extremities even in upright 1G conditions. The observed results suggest that this progressive stiffening along the caudal direction persists across increasing gravity levels. Furthermore, as G increases, the difference in both Z_c and c between central and peripheral regions becomes more pronounced. This is due to the increased hydrostatic column below the level of orthostatic indifference, which accentuates the caudal fluid shift. It can thus be hypothesized that, in addition to a "passive" stiffening of vessels toward

the periphery, the cardiovascular system also actively increases peripheral vasoconstriction as G rises—especially in more distal sites where the hydrostatic column is greatest. Specifically, reflexive vasoconstriction of peripheral districts is mediated by high-pressure baroreceptors located at the carotid sinus and aortic arch. These receptors, being sensitive to the central pressure drop induced by the fluid shift, activate sympathetic-mediated vasoconstriction in an effort to preserve arterial pressure *(Guyton & Hall, Textbook of Medical Physiology)*. In order to underline this result, the last columns in the tables 5.4 and 5.3 report the percentage changes in Z_c and c between the anterior tibial artery and the aortic root for each gravity level. These clearly indicate that the variation increases with G. Therefore, it may be concluded that the percentage stiffening of peripheral arterial walls increases progressively with rising gravitational acceleration and hydrostatic pressure below the heart, suggesting a compensatory response aimed at mitigating orthostatic stress along the cranio-caudal axis.

Analyzing the site-specific trends of Z_c and c with increasing G, it becomes evident that vessels below the heart level exhibit different behaviors depending on their anatomical location. Central sites experience relatively smaller variations in both parameters compared to more distal sites. In particular, while the aortic root shows slightly greater changes than the thoracic aorta, the absolute magnitude of variation in Z_c and c from 0G to 3G remains extremely limited. In general, all sites below heart level display a monotonic increase in both parameters with increasing G, with a clear trend from the thoracic to the tibial level. Central vessels, such as the aortic root and thoracic aorta, exhibit low and relatively stable values of Z_c and c due to their proximity to the heart and their high compliance, which enables them to dampen pressure peaks. These central arteries have limited capacity for compliance modulation and lack active vasoconstriction. Additionally, due to their location near the heart, they are less affected by changes in the hydrostatic load along the cranio-caudal axis, maintaining approximately constant Z_c and c values regardless of G. In contrast, the anterior tibial artery exhibits the highest relative increase in both Z_c and c from 0G to 3G, indicating a greater susceptibility to compliance changes than central vessels like the aorta. This confirms that, in hypergravity, the cardiovascular system adopts a compensatory strategy based on progressive arterial stiffening in more peripheral regions to counteract increasing orthostatic stress.

Conversely, vessels located above the level of orthostatic indifference, such as the internal and external carotid arteries, display an opposite trend with increasing G. Both exhibit a decreasing trend in Z_c and c, which is more pronounced in the internal carotid artery (ICA), especially in wave speed. The reduction in cerebral perfusion pressure due to fluid shift under higher G levels leads to an increase in

area compliance of the carotid arteries, exceeding the increase in cross-sectional area associated with vasodilation (as per the 4.1 equation). The difference in behavior between the ICA and ECA may be attributed to their distinct functional roles. The ECA supplies extracranial structures—such as facial muscles and skin—which are less critical for homeostasis compared to the cerebro-ocular regions perfused by branches of the ICA. The greater compliance variation in the ICA may thus reflect an effort to stabilize pressure in vessels supplying vital, pressure-sensitive organs.

To sum up, the observed trends suggest that the functional and regulatory mechanisms of the arterial system are preserved across different gravity levels. More importantly, these mechanisms appear to become increasingly amplified with rising hydrostatic gradients, in order to counteract the orthostatic stress induced by gravity and ensure stable cerebral perfusion.

5.3 Gravity stress effect on Decomposed Wave Patterns

Once the mean values of characteristic impedance and wave speed have been computed under the different gravitational conditions and at the various arterial sites considered, the wave decomposition process can be carried out. In particular, both pressure waves and flow rate waves were decomposed by separating the forward and backward components in all relevant cases.

It is worth recalling that the gravitational acceleration levels analyzed range from 0G to 3G, adopting increments of 0.5G according to a first investigation approach. The arterial vessels examined—each uniquely identified by a reference number—include the Aortic Root (1), the right Internal Carotid Artery (12), the right External Carotid Artery (13), the Thoracic Aorta (18), the Abdominal Aorta (37), the Iliac Artery (42), the Femoral Artery (46) and the Anterior Tibial Artery (47).

In figures 5.11 and 5.12, the superimposed profiles of the decomposed pressure and flow rate waves (forward and backward) are shown for each site, under four distinct gravitational conditions: 0G, 1G, 2G, and 3G. For conciseness, the diagrams are shown only for four gravitational conditions, thereby enabling a qualitative and visual appreciation of the effect of increasing gravitational stress on waveforms. Furthermore, table 5.5 provides the mean and the pulse values of all decomposed pressure and flow rate waves obtained through wave separation, across all analyzed gravitational conditions (0G, 0.5G, 1G, 1.5G, 2G, 2.5G, 3G) and different arterial sites.

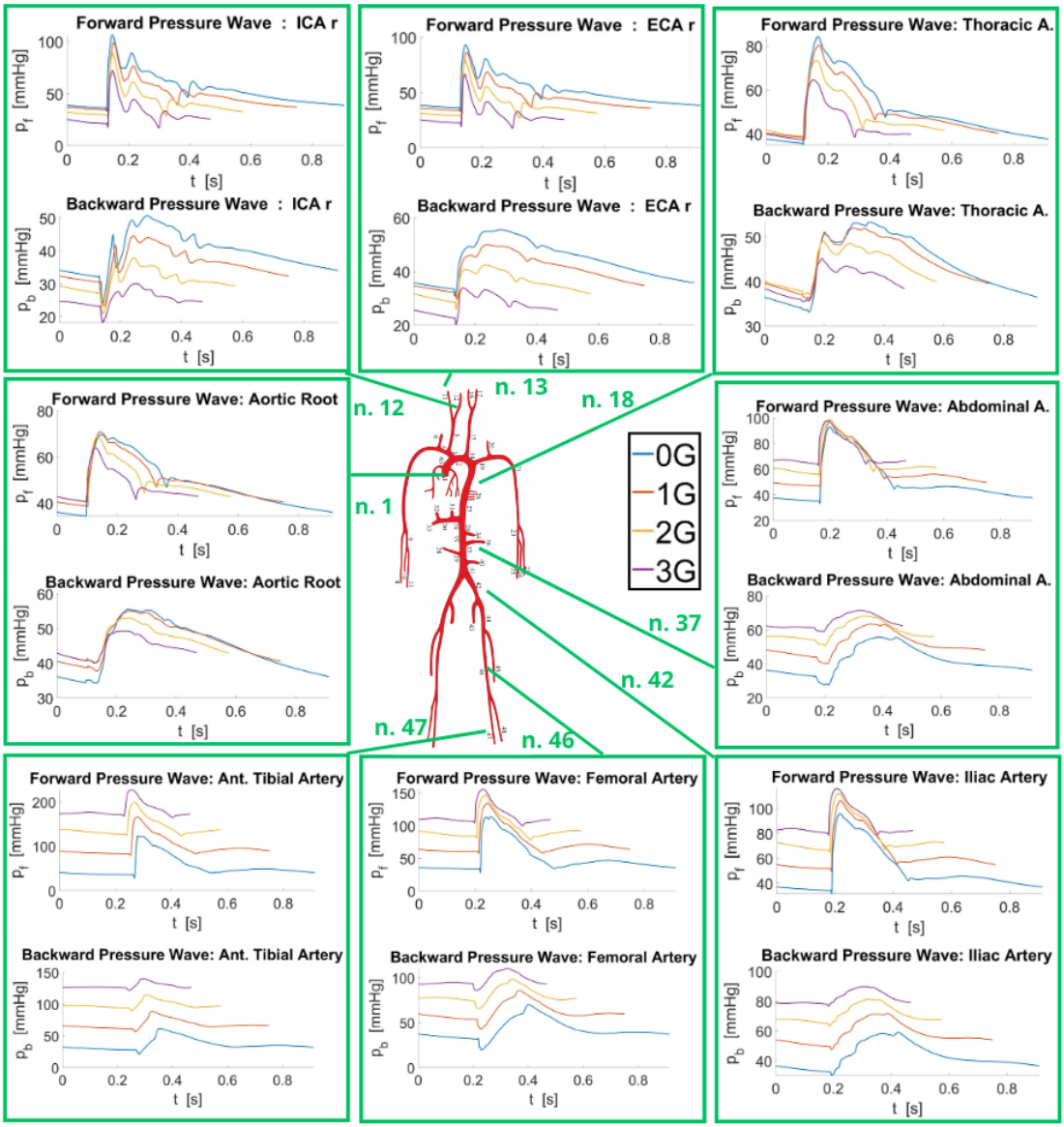

Figure 5.11: Forward and backward pressure waves obtained at different arterial sites under four distinct gravitational conditions: 0G (blue), 1G (red), 2G (yellow), and 3G (purple). Numbers associated with each arterial site correspond to the arterial tree topology illustrated in Figure 3.1.

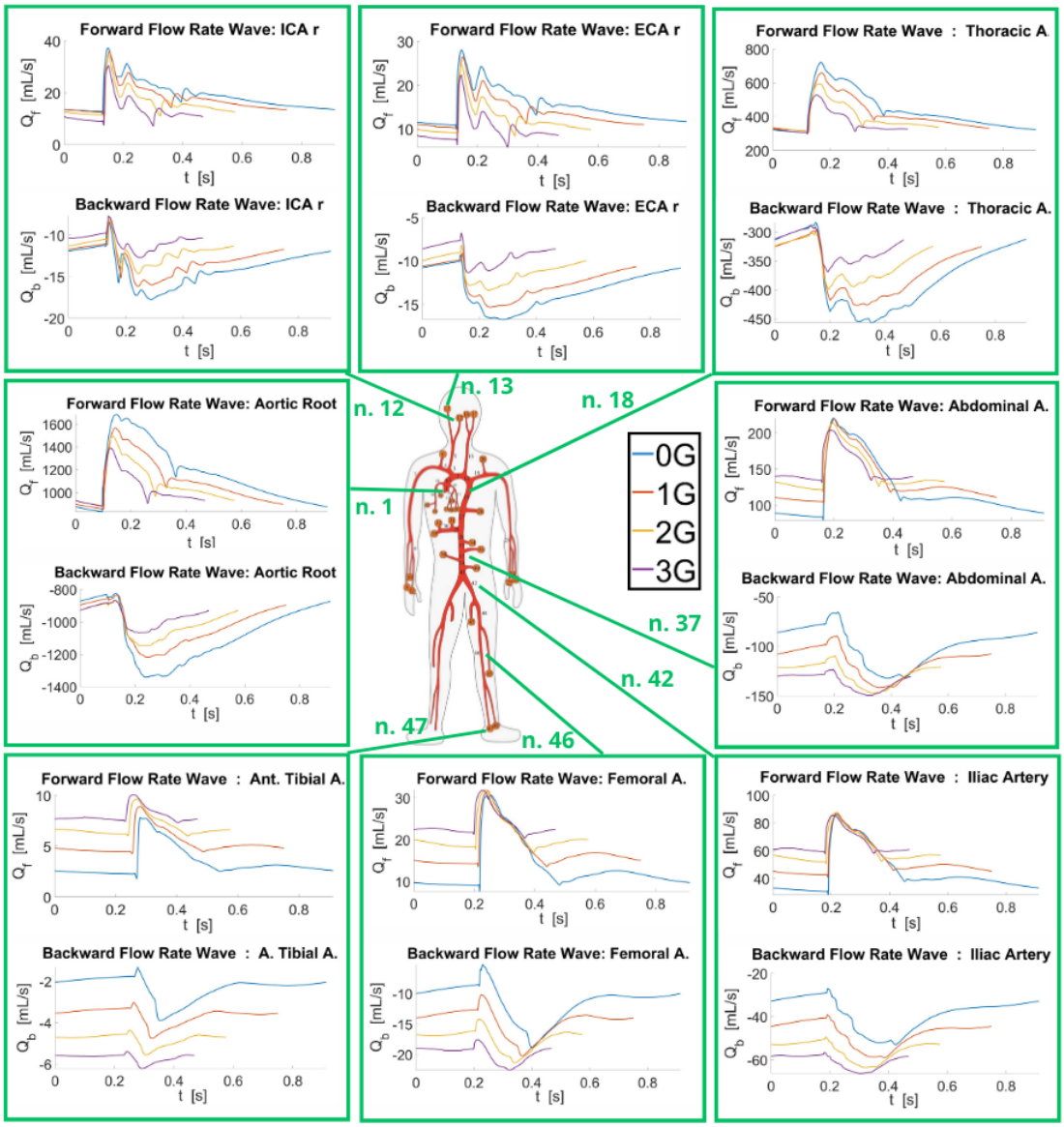

Figure 5.12: Forward and backward flow rate waves obtained at different arterial sites under four distinct gravitational conditions: 0G (blue), 1G (red), 2G (yellow), and 3G (purple). Numbers associated with each arterial site correspond to the arterial tree topology illustrated in Figure 3.1.

Aortic Root	0G	0.5G	1G	1.5G	2G	2.5G	3G
p_b mean [mmHg]	44.35	46.08	46.40	46.54	46.50	46.07	44.70
p_f mean [mmHg]	47.87	49.66	49.82	49.87	49.68	49.03	47.43
Q_b mean [mL/s]	-1071.50	-1017.79	-1025.05	-1011.44	-1008.23	-1013.17	-968.57
Q_f mean [mL/s]	1156.58	1096.91	1100.67	1083.83	1077.27	1078.21	1027.77
p_b pulse [mmHg]	21.25	20.61	17.30	14.93	12.89	10.95	9.15
p_f pulse [mmHg]	35.35	34.78	32.27	30.18	28.07	25.83	23.46
Q_b pulse [mL/s]	513.55	455.14	382.17	324.54	279.52	240.76	198.30
Q_f pulse [mL/s]	854.22	768.26	712.89	655.97	608.68	567.96	508.33
r ICA	0G	0.5G	1G	1.5G	2G	2.5G	3G
p_b mean [mmHg]	39.61	38.58	36.06	33.56	30.97	28.29	25.47
p_f mean [mmHg]	53.21	51.62	48.46	45.03	41.27	36.79	30.62
Q_b mean [mL/s]	-13.87	-13.81	-13.08	-12.54	-11.96	-11.28	-10.74
Q_f mean [mL/s]	18.64	18.49	17.58	16.82	15.93	14.67	12.91
p_b pulse [mmHg]	26.59	24.21	21.36	19.09	16.88	14.36	11.96
p_f pulse [mmHg]	73.37	70.13	68.03	65.38	62.66	59.79	55.30
Q_b pulse [mL/s]	9.32	8.67	7.75	7.13	6.52	5.73	5.04
Q_f pulse [mL/s]	25.70	25.11	24.68	24.42	24.19	23.84	23.31
r ECA	0G	0.5G	1G	1.5G	2G	2.5G	3G
p_b mean [mmHg]	44.00	43.23	40.80	38.15	35.25	31.89	27.58
p_f mean [mmHg]	50.35	48.50	45.22	41.89	38.40	34.52	29.71
Q_b mean [mL/s]	-13.24	-13.14	-12.49	-11.77	-11.08	-10.22	-9.24
Q_f mean [mL/s]	15.15	14.74	13.84	12.92	12.07	11.06	9.95
p_b pulse [mmHg]	24.71	23.00	20.31	18.28	16.50	14.88	13.62
p_f pulse [mmHg]	60.17	57.75	55.96	54.59	53.13	51.99	48.96
Q_b pulse [mL/s]	7.44	6.99	6.21	5.64	5.19	4.77	4.56
Q_f pulse [mL/s]	18.11	17.55	17.13	16.84	16.70	16.66	16.40
Thoracic Aorta	0G	0.5G	1G	1.5G	2G	2.5G	3G
p_b mean [mmHg]	43.74	45.04	44.63	44.12	43.39	42.24	40.19
p_f mean [mmHg]	50.27	50.98	50.33	49.51	48.48	47.04	44.59
Q_b mean [mL/s]	-373.97	-378.54	-366.54	-360.44	-351.90	-340.67	-327.93
Q_f mean [mL/s]	429.85	428.52	413.34	404.44	393.21	379.33	363.79
p_b pulse [mmHg]	20.24	19.10	16.01	13.39	12.07	10.94	9.65
p_f pulse [mmHg]	49.31	46.60	42.89	38.87	35.35	32.15	28.16
Q_b pulse [mL/s]	173.04	160.55	131.45	109.42	97.91	88.24	78.70
Q_f pulse [mL/s]	421.61	391.66	352.28	317.53	286.66	259.28	229.75

Abdominal Aorta	0G	0.5G	1G	1.5G	2G	2.5G	3G
p_b mean [mmHg]	41.65	47.36	51.43	55.43	59.04	62.29	64.71
p_f mean [mmHg]	50.90	56.29	60.14	63.77	67.34	70.42	72.44
Q_b mean [mL/s]	-98.78	-107.74	-115.06	-124.34	-127.57	-131.02	-135.40
Q_f mean [mL/s]	120.73	128.05	134.55	143.06	145.50	148.12	151.57
p_b pulse [mmHg]	28.10	27.37	23.47	19.69	17.35	15.07	12.49
p_f pulse [mmHg]	59.84	57.04	52.58	47.76	44.05	39.85	34.77
Q_b pulse [mL/s]	66.65	62.26	52.51	44.17	37.48	31.70	26.14
Q_f pulse [mL/s]	141.94	129.76	117.63	107.14	95.18	83.82	72.75
Iliac Artery	0G	0.5G	1G	1.5G	2G	2.5G	3G
p_b mean [mmHg]	42.83	51.28	58.05	64.68	71.17	77.21	82.32
p_f mean [mmHg]	49.90	58.14	64.88	71.50	77.82	83.74	88.65
Q_b mean [mL/s]	-38.42	-43.80	-47.76	-51.24	-55.54	-58.75	-60.74
Q_f mean [mL/s]	44.76	49.65	53.38	56.65	60.73	63.71	65.41
p_b pulse [mmHg]	28.79	27.79	24.16	20.94	17.98	15.52	13.26
p_f pulse [mmHg]	64.22	61.27	56.71	52.16	47.20	42.39	37.23
Q_b pulse [mL/s]	25.83	23.74	19.87	16.59	14.03	11.81	9.78
Q_f pulse [mL/s]	57.61	52.33	46.65	41.33	36.84	32.25	27.47
Femoral Artery	0G	0.5G	1G	1.5G	2G	2.5G	3G
p_b mean [mmHg]	42.00	52.71	62.04	71.23	80.46	89.19	97.25
p_f mean [mmHg]	49.78	62.96	74.31	85.51	96.25	106.63	115.75
Q_b mean [mL/s]	-11.31	-12.97	-14.62	-15.90	-17.47	-18.51	-19.86
Q_f mean [mL/s]	13.41	15.50	17.51	19.08	20.90	22.13	23.64
p_b pulse [mmHg]	50.73	48.38	42.60	38.05	33.06	29.17	24.46
p_f pulse [mmHg]	85.51	82.98	77.33	73.73	68.95	63.89	55.89
Q_b pulse [mL/s]	13.67	11.91	10.04	8.49	7.18	6.05	5.00
Q_f pulse [mL/s]	23.03	20.42	18.22	16.46	14.97	13.26	11.42
Ant. Tibial Artery	0G	0.5G	1G	1.5G	2G	2.5G	3G
p_b mean [mmHg]	36.36	52.78	68.04	83.20	98.89	113.48	128.61
p_f mean [mmHg]	53.22	76.91	98.84	120.70	141.64	162.86	181.58
Q_b mean [mL/s]	-2.31	-3.02	-3.65	-4.18	-4.80	-5.13	-5.70
Q_f mean [mL/s]	3.37	4.41	5.30	6.06	6.87	7.36	8.05
p_b pulse [mmHg]	40.74	36.99	32.35	28.48	24.68	21.99	18.41
p_f pulse [mmHg]	95.26	92.79	86.97	81.42	75.04	71.18	62.60
Q_b pulse [mL/s]	2.58	2.12	1.73	1.43	1.20	0.99	0.82
Q_f pulse [mL/s]	6.04	5.32	4.66	4.09	3.64	3.22	2.78

Table 5.5: Mean and pulse values of forward/backward pressure and flow rate waves under different gravity conditions.

In the following, representative graphs have been plotted based on the variables presented in the table 5.5, in order to more clearly illustrate the evolution of selected parameters as a function of gravitational acceleration and across all the analysed arterial sites.

Firstly, figure 5.13 depicts the mean forward pressure wave values across increasing G. Each site is associated with a distinct color and exhibits a specific trend in mean forward pressure as gravity increases. Central sites—such as the aortic root and thoracic aorta, which are located at approximately the same height as the heart—display nearly constant trends across G, demonstrating effective regulatory mechanisms that maintain mean forward pressure within physiological ranges at 1G. Specifically, the aortic root's mean values vary between +4.2% and -0.92% relative to the 0G condition. By contrast, peripheral vessels caudal to the heart show increasing influence of G on mean forward pressure.

With increasing G, a twofold effect occurs: firstly, mean forward pressure increases in all sites below heart level, and secondly the percentage increase becomes progressively steeper in more distal vessels, as evidenced by diverging curves in figure 5.13. Consistent with decreasing compliance and progressive increases in wave speed and characteristic impedance, the mean forward pressure waves in regions below the orthostatic indifference point stabilize at higher average levels. Notably, under microgravity conditions, all sites exhibit extremely similar mean forward pressure values, whereas with increasing G they diverge markedly—excluding the central vessels, which show quite a constant behaviour across the entire G range. In fact, the anterior tibial artery shows the steepest increase, with a percent change of approximately +242% between 0G and 3G.

Conversely, carotid sites exhibit a mild reduction in mean forward pressure. The right internal and external carotids remain nearly constant between 0G and 1G, then decline at higher G. This finding aligns with an increase in area compliance of vessels above the indifference level, helping counteract cephalic perfusion pressure loss due to the gravity induced fluid shift. In this case, the ICA exhibits a slightly greater percentage change compared to the ECA, with a variation between 1G and 3G of -37%, as opposed to -34% for the ECA.

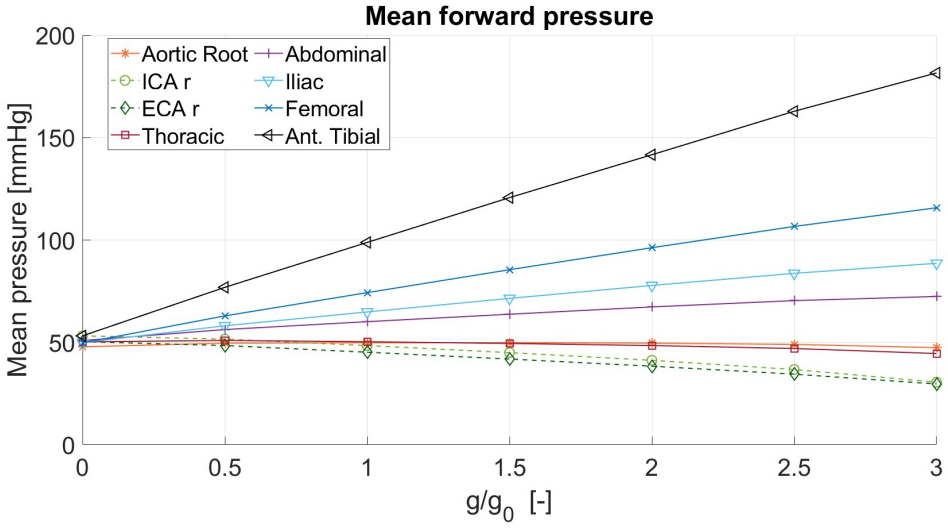

Figure 5.13: Trend of the mean forward pressure wave values as gravitational acceleration increases (g/g_0). Each arterial site is represented by a different color and a specific marker. Sites located above heart level are represented using dashed lines.

Differently from the mean forward pressure values, across both above- and below-heart-level regions, pulsatile amplitudes of forward pressure waves decrease with increasing G. However, pulsatility percentage variations differ between sites located above and below heart level (see figure 5.14). Specifically, the vessels extending from the aortic root to the anterior tibial artery show percentage reductions in pulse forward pressure of approximately -30%/-40% between 0G and 3G, while the ICAr shows around -25% reduction, and the ECA around -17%. Given that carotid arteries are at roughly equivalent vertical distance from the heart as the abdominal aorta—which shows about -42% reduction in forward pressure pulsatility — carotid sites undergo roughly half the reduction observed below heart level.

Overall, it is important to underline that decreased pulsatility (especially centrally) reflects reduced exercise capacity and general cardiovascular stress. This outcome may result from two opposing effects: decreased stroke volume (SV) with rising G — which lowers central pulsatility [12] — and reduced systemic compliance (particularly in lower limbs) — which would tend to increase pressure pulsatility for a given volume change. The former appears to predominate at higher G, resulting in a reduction in pressure systemic pulsatility. The relatively smaller pulsatility changes observed in carotid vessels may reflect more robust cerebral autoregulation and a greater vasodilation effectiveness in preserving pulse forward pressure values.

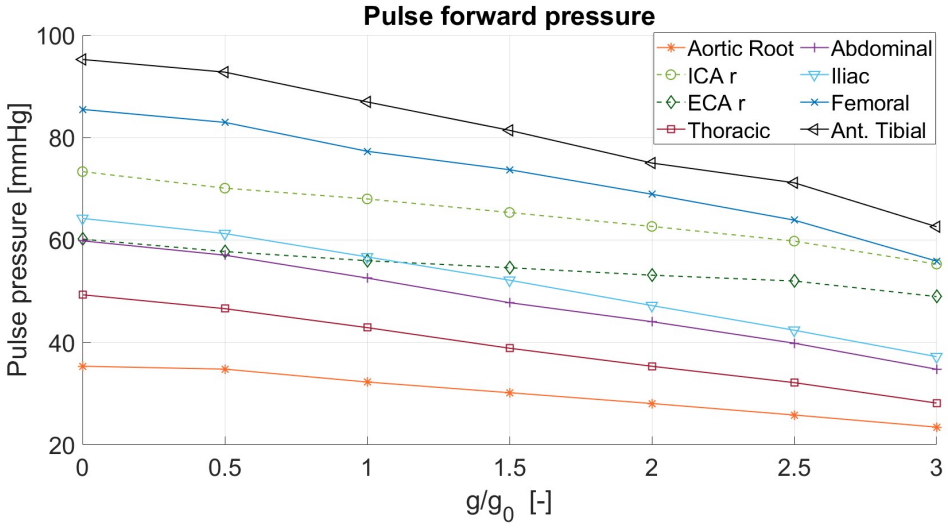

Figure 5.14: Trend of the pulse forward pressure wave values as gravitational acceleration increases (g/g_0). Each arterial site is represented by a different color and a specific marker. Sites located above heart level are represented using dashed lines.

Regarding mean values of forward flow rate waves, per-site trends as a function of G are illustrated in figure 5.15. It can be observed that the physiological gradient of decreasing mean forward flow rate from the aortic root to peripheral vessels is preserved, with increasing G, in accordance with continuity constraint and arterial systemic branching. However, under gravity changes, distinct arterial vessels show different behaviours. Interestingly, vessels near heart level (such as aortic root and thoracic aorta) show a progressive reduction in mean forward flow rate values from 0G to 3G: -11.1% for the aortic root and -15.4% for the thoracic aorta. This result could be related to the decrease of SV (as documented by [12]), despite the HR increase, as well as to the reduced venous return induced by fluid shift.

In contrast, distal vessels from abdominal aorta to tibial artery demonstrate increasing forward flow rate mean values with rising G: +25.5% (abdominal aorta), +46.1% (iliac), +76.3% (femoral), and +139% (anterior tibial). This suggests a distinction between the volumetric indifference level and the orthostatic indifference level: the point of negligible volume change lies below heart level, separating regions where mean forward flow rate decreases (such as the thoracic and upper body region) from those where it increases (as lower abdomen and lower limbs). This result reflects upper body blood depletion versus lower body pooling as a consequence of gravity stress increase.

Carotid sites similarly show decreasing mean forward volumetric flow, with larger percent drops compared to central sites: -31% for the right ICA and -34% for the right ECA. This is consistent with carotid vessels being located above the volumetric indifference point and more distant from it compared to central vessels. The slightly smaller percentage reduction observed for the ICA (wrt the ECA) may reflect more effective cerebral autoregulation to protect perfusion of highly pressure-sensitive cerebro-ocular tissues.

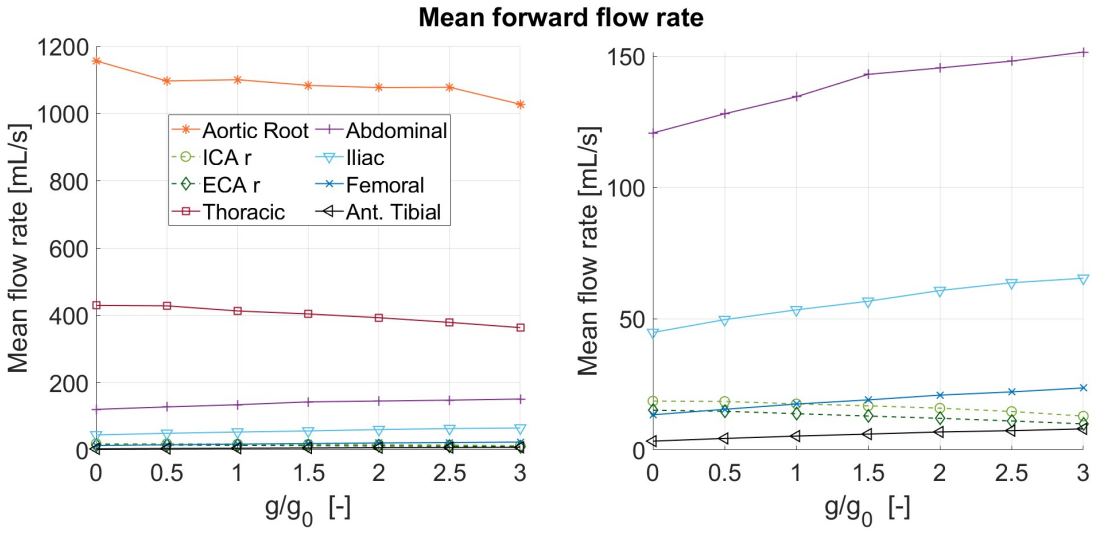

Figure 5.15: Trend of the mean forward flow rate wave values as gravitational acceleration increases (g/g_0). Each arterial site is represented by a different color and a specific marker. Sites located above heart level are represented using dashed lines. A zoomed-in view on flow rate values between 0 mL/s and 150 mL/s is shown on the right.

With regard to the pulsatility of the forward flow waves, a decreasing trend is observed across all arterial sites analyzed, similarly to the pressure waves behaviour (see figure 5.16). At the central level, the percentage variation in forward flow wave pulsatility between 0G and 3G is approximately -40.5% at the aortic root and -45.5% at the thoracic aorta. Considering that during the early phase of systole the only existing wave is the forward wave, this finding may be indicative of a reduced left ventricle contractile response under increasing orthostatic load. Moving caudally, this reduction becomes progressively more pronounced, reaching -54.0% at the anterior tibial artery. The carotid sites also exhibit a reduction in forward flow pulsatility; however, this decline is significantly less marked, with percentage reductions of approximately -9.3% (right ICA) and -9.4% (right ECA) between 0G and 3G.

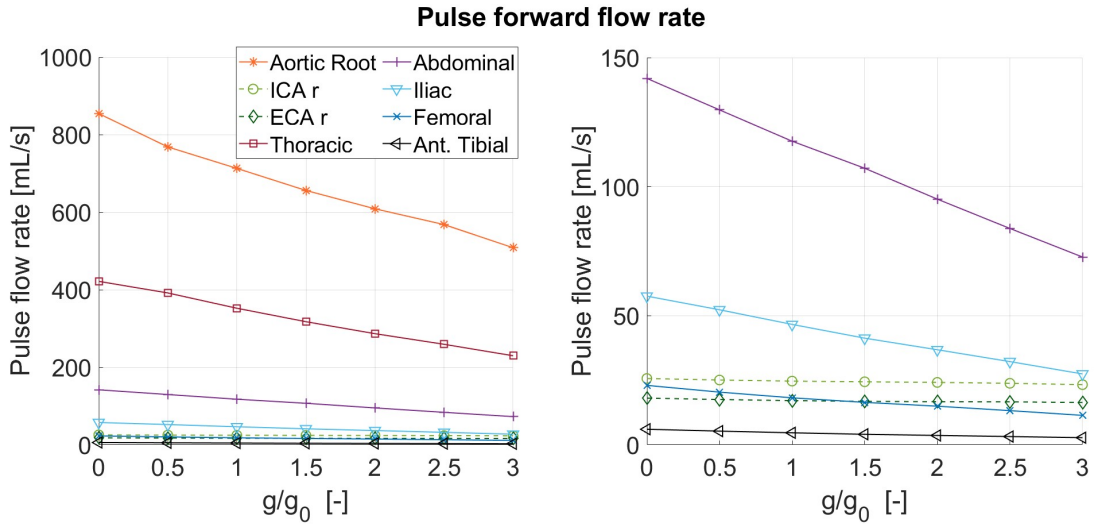

Figure 5.16: Trend of the pulse forward flow rate wave values as gravitational acceleration increases (g/g_0). Each arterial site is represented by a different color and a specific marker. Sites located above heart level are represented using dashed lines. A zoomed-in view on flow rate values between 0 mL/s and 150 mL/s is shown on the right.

At this stage, the analysis aims to investigate the effect of gravitational acceleration (G) not only on forward pressure and flow waves, but also on backward components, in order to assess the impact of orthostatic stress on reflected waves along the arterial tree. Specifically, the analysis focuses on three representative sites: the central region (aortic root), the distal caudal region (anterior tibial artery), and the distal cranial region (right external carotid artery, ECA).

Figure 5.17 compares forward and backward wave variables at the level of the aortic root. On the left, the plots illustrate the trends in mean and pulse values of pressure waves as a function of G, while the right-hand side displays the same quantities for volumetric flow rate waves. Blue lines indicate forward waves, whereas orange lines denote backward waves. At the aortic root, the mean values of both forward and backward pressure waves remain approximately constant across the G spectrum. In contrast, the mean values of flow waves exhibit a notable reduction in magnitude. For both pressure and flow, the mean values of backward waves are slightly lower than those of forward waves, indicating a substantial, albeit not equivalent, contribution of reflected waves. For mean backward flow rate waves values, the curve is plotted using the absolute value, despite the negative mean values. Interestingly, the mean flow values—both forward and backward—exhibit minimal variation within the gravitational range of 0.5G

to 2.5G, while more pronounced changes occur at the extremes of microgravity and hypergravity (0G–0.5G and 2.5G–3G). Regarding pulsatility, as previously discussed, a decreasing trend is observed for all waveforms analyzed—both forward and backward—with comparable percentage reductions between 0G and 3G for waves of the same type. Notably, the pulsatility of pressure waves does not exhibit the plateau observed in the mean flow rate waveforms values within the intermediate gravitational interval (0.5G–2.5G).

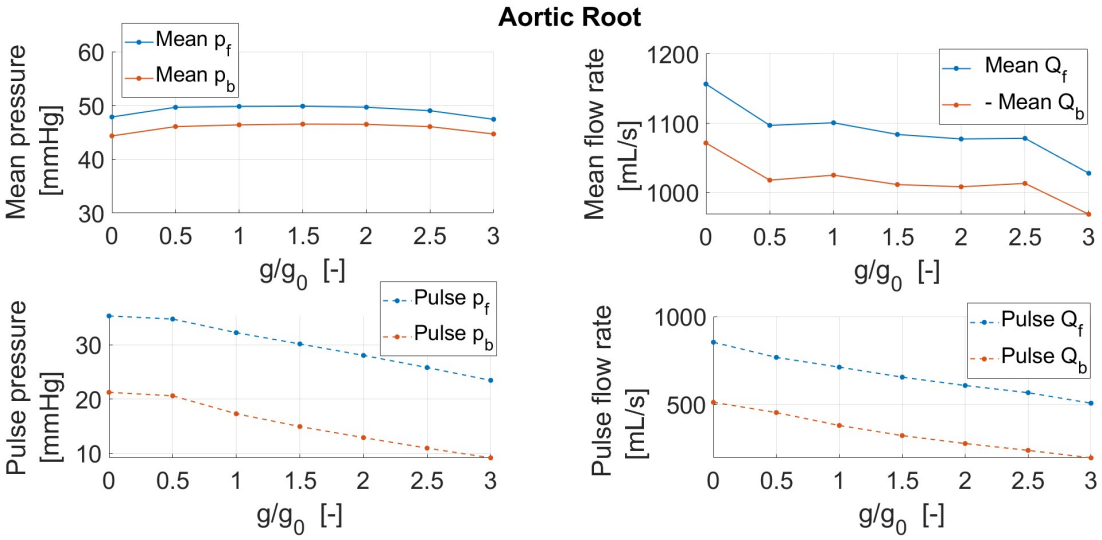

Figure 5.17: (Left) Trend of mean and pulsatile values of the total pressure forward and backward waves, at the aortic root. (Right) Trend of mean and pulsatile values of the total flow rate forward and backward waves, at the aortic root. Forward quantities are represented by blue lines, while backward quantities are shown in orange. Solid lines indicate mean values, whereas dashed lines represent pulsatile components.

Figure 5.18 presents the same variables previously illustrated in figure 5.17, but for the peripheral site of the anterior tibial artery. In this case, the mean values of both forward and backward pressure waves exhibit a marked increase with rising G, with a steeper rise observed for the backward wave: from 0G to 3G, mean forward pressure increases by +241%, while backward pressure increases by +254%. A similar trend is observed for the mean values of forward and backward flow rate waves: from 0G to 3G, the absolute value of mean backward flow rate increases by +147%, while forward flow rate increases by +139%. Likewise, the percentage changes in pulsatile values of both pressure and flow rate waves (forward and backward) are greater for the backward components than for the forward ones. Specifically, from 0G to 3G, the pulsatility of backward and forward pressure waves

decreases by -54.8% and -34.3%, respectively, while the pulsatility of backward and forward flow waves decreases by -68.2% and -54.0%, respectively. These findings suggest that reflected waves at peripheral sites—such as the anterior tibial artery—are more sensitive to changes in gravitational acceleration than their forward counterparts, for both pressure and flow rate. Moreover, this effect appears more pronounced in distal regions compared to central sites (see the case of the aortic root).

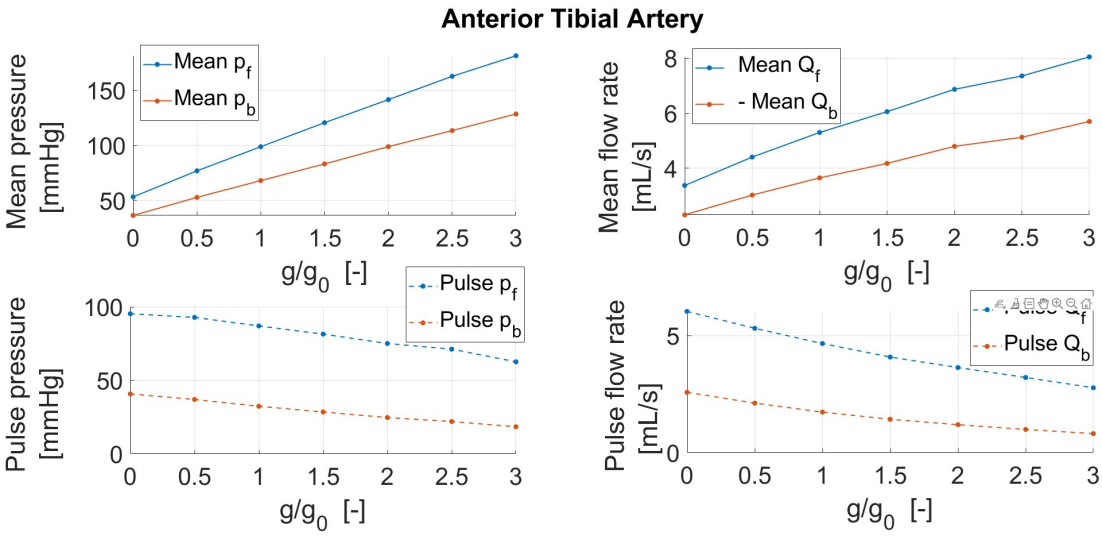

Figure 5.18: (Left) Trend of mean and pulsatile values of the total pressure forward and backward waves in the anterior tibial artery. (Right) Trend of mean and pulsatile values of the total flow rate forward and backward waves in the anterior tibial artery. Forward quantities are represented by blue lines, while backward quantities are shown in orange. Solid lines indicate mean values, whereas dashed lines represent pulsatile components.

Finally, Figure 5.19 examines the case of the right external carotid artery, displaying the same quantities previously discussed in figures 5.17 and 5.18. In this instance, the mean values of both pressure and flow rate waves decrease with increasing G, affecting both forward (as previously noted) and backward components. Between 0G and 3G, the mean values of backward and forward pressure decrease by -37.3% and -41.0%, respectively, while the corresponding changes in flow rate are -30.2% and -34.3%. This suggests that in this case, backward waves are slightly less affected than forward waves in terms of percentage changes in mean values due to varying G. Regarding pulsatility, which decreases in all cases examined, differences between forward and backward waves are more substantial than those observed for mean values and show opposite nature. Specifically, the pulsatility

of backward pressure decreases by -44.9% between 0G and 3G, compared to only -18.6% for forward pressure pulsatility. Similarly, flow rate pulsatility decreases by -38.7% for the backward wave and by -9.4% for the forward wave. This behavior, on one hand mirrors the trend observed in the anterior tibial artery (where backward waves appear more sensitive to gravitational changes), while, on the other hand, contrasts with what is seen in the mean value trends.

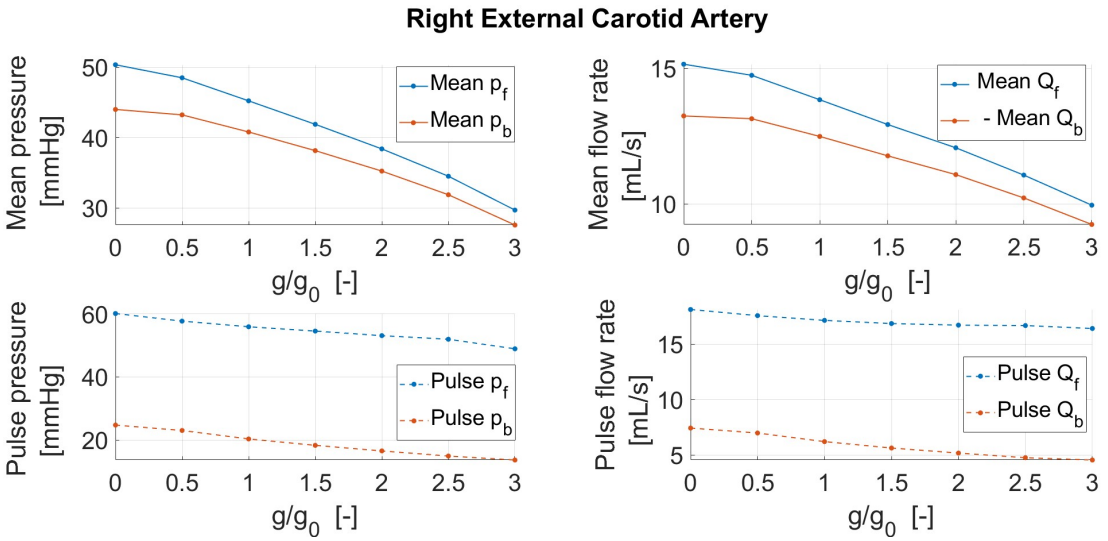

Figure 5.19: (Left) Trend of mean and pulsatile values of the total pressure forward and backward waves in the right external carotid artery. (Right) Trend of mean and pulsatile values of the total flow rate forward and backward waves in the right external carotid artery. Forward quantities are represented by blue lines, while backward quantities are shown in orange. Solid lines indicate mean values, whereas dashed lines represent pulsatile components.

5.4 Gravity stress effect on Reflection Parameters

After performing the wave separation and thereby isolating the forward and backward components of both pressure and flow rate waves, it is now possible to proceed with the calculation of the reflection coefficients. In particular, the following section focuses on the analysis of the Reflection Magnitude and the Reflection Index, both evaluated with respect to pressure waves. The relevant formulas and the underlying mathematical framework have been presented earlier, and the reader is referred to the corresponding section for further details (see Section 2.5).

Figures 5.20 and 5.21 illustrate the trends of the Reflection Magnitude (RM) and the Reflection Index (RI), computed for the various gravitational conditions across all analyzed arterial sites, each represented by a distinct color. In addition, tables 5.6 and 5.7 present the corresponding numerical values of both reflection coefficients, calculated after the wave decomposition process. The final row of each table reports the percentage variations observed between the 0G and 3G conditions for each analyzed site.

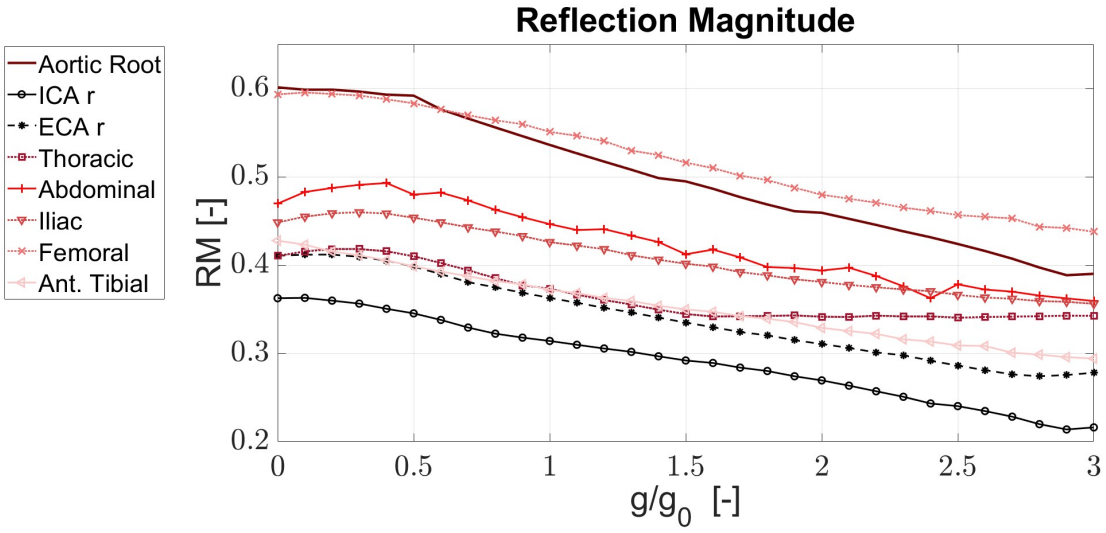

Figure 5.20: Reflection Magnitude under varying gravity (g/g_0) across the analyzed arterial sites. Each analyzed site is associated with a distinct color and a specific marker.

By analyzing the trend of RM, shown in Figure 5.20, as gravitational acceleration increases across the different locations, it can be observed that RM generally exhibits a monotonic decrease in nearly all the arterial sites analyzed. A slightly different behavior is observed at the level of the thoracic aorta, where RM remains approximately constant between 1.5G and 3G, oscillating within a narrow range between 0.3403 and 0.3446. The most significant percentage reduction is observed in the right internal carotid artery (ICAr), amounting to approximately -40%. Conversely, the smallest percentage reduction occurs at the level of the thoracic aorta, where RM decreases by about –16.5% between 0G and 3G, with the majority of the variation occurring between 0G and 1.5G. The aortic root exhibits a marked decrease in RM between 0G and 3G, suggesting that the backward wave component diminishes more substantially than the forward component as gravitational acceleration increases. This may imply a particularly effective attenuation of reflected wave amplitude in proximity to the aortic valve, which is especially sensitive to the

effects of pressure surges (water hammer phenomena).

Moreover, it is observed that in the thoraco-abdominal region the percentage variations in RM generally tend to diminish, but increase again when moving towards the caudal extremity. From the iliac artery to the anterior tibial artery, the magnitude of the RM reduction becomes progressively more pronounced.

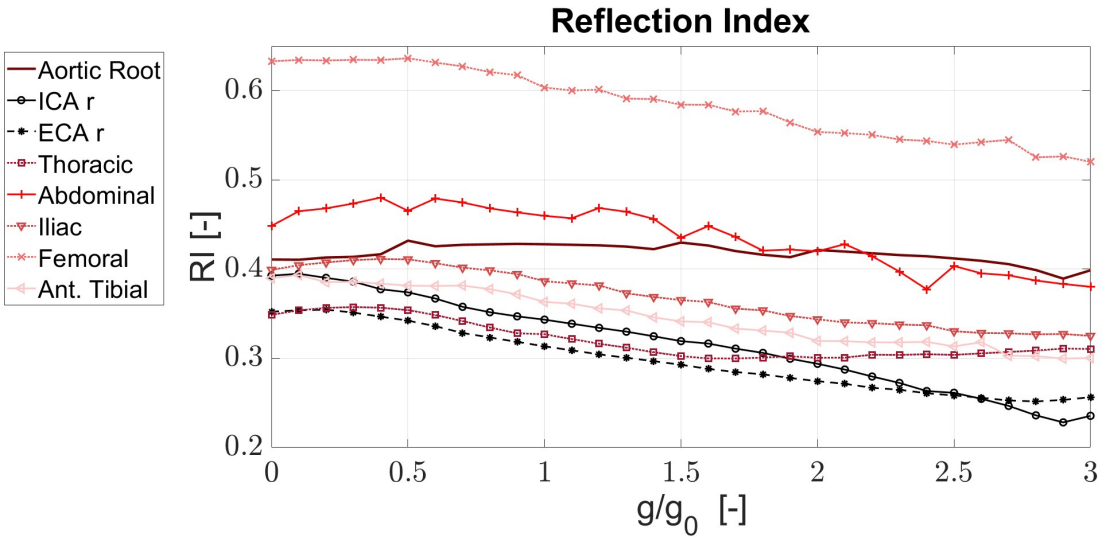

Figure 5.21: Reflection Index under varying gravity (g/g_0) across the analyzed arterial sites. Each analyzed site is associated with a distinct color and a specific marker.

Examining the behavior of the RI values across different sites and gravitational loads 5.21 reveals generally smaller percentage changes between 0G and 3G when compared to RM. An exception is again observed in the ICAr, where the percentage reduction in RI from 0G to 3G is comparable to that of RM. A significant difference in the behavior of the two parameters emerges at the aortic root: while RM shows a clear decrease, RI remains approximately constant across G levels. This indicates that, although the backward wave amplitude decreases significantly relative to the forward wave (as reflected in the RM reduction), its contribution relative to the total wave amplitude changes much less at the central level.

Another key distinction between the behavior of RI and RM is that, while RM consistently decreases with increasing G in all sites, RI exhibits a slight initial increase between 0G and 0.5G at certain locations, such as the aortic root, thoracic aorta, abdominal aorta, iliac artery, and femoral artery. In contrast, in both the ICAr and the ECAr, the RI follows a monotonic decreasing trend. Additionally, within the gravitational range of 0G to 1G, RI shows more modest percentage variations in the sites between the thoracic aorta and the anterior tibial artery than

those observed between 1G and 3G at the same sites.

	Aortic Root	**ICA r**	**ECA r**	**Thoracic**	**Abdominal**	**Iliac**	**Femoral**	**Ant. Tibial**
RM 0G	0.6012	0.3625	0.4107	0.4104	0.4696	0.4484	0.5932	0.4277
RM 0.5G	0.5924	0.3453	0.3983	0.4099	0.4798	0.4536	0.5831	0.3986
RM 1G	0.5361	0.3140	0.3629	0.3731	0.4464	0.4260	0.5509	0.3719
RM 1.5G	0.4947	0.2920	0.3348	0.3446	0.4122	0.4015	0.5160	0.3498
RM 2G	0.4592	0.2694	0.3105	0.3415	0.3938	0.3808	0.4796	0.3289
RM 2.5G	0.4239	0.2403	0.2861	0.3403	0.3782	0.3662	0.4566	0.3090
RM 3G	0.3901	0.2162	0.2781	0.3425	0.3593	0.3561	0.4377	0.2941
% Variation 0G-3G	-35.1	-40.4	-32.3	-16.5	-23.5	-20.6	-26.2	-31.2

Table 5.6: Numerical values of Reflection Magnitude (RM) at different arterial sites under distinct gravity conditions. The final row reports the percentage variations of RM observed between the 0G and 3G conditions for each analyzed site.

	Aortic Root	**ICA r**	**ECA r**	**Thoracic**	**Abdominal**	**Iliac**	**Femoral**	**Ant. Tibial**
RI 0G	0.4108	0.3927	0.3523	0.3489	0.4485	0.3993	0.6331	0.3898
RI 0.5G	0.4331	0.3453	0.3423	0.3541	0.4654	0.4109	0.6364	0.3815
RI 1G	0.4279	0.3434	0.3135	0.3270	0.4597	0.3865	0.6035	0.3632
RI 1.5G	0.4298	0.3193	0.2928	0.3025	0.4352	0.3653	0.5844	0.3414
RI 2G	0.4215	0.2939	0.2744	0.3007	0.4200	0.3438	0.5537	0.3195
RI 2.5G	0.4120	0.2614	0.2584	0.3039	0.4035	0.3304	0.5396	0.3133
RI 3G	0.3987	0.2355	0.2564	0.3105	0.3803	0.3252	0.5204	0.3003
% Variation 0G-3G	-2.9	-40.0	-27.2	-11.0	-15.2	-18.6	-17.8	-23.0

Table 5.7: Numerical values of Reflection Index (RI) at different arterial sites under distinct gravity conditions. The final row reports the percentage variations of RI observed between the 0G and 3G conditions for each analyzed site.

In general, it can be concluded that, relative to the baseline condition (1G), an increase in gravitational loading along the cranio-caudal axis leads to a reduction in both reflection parameters (RM and RI) at all analyzed sites, irrespective of whether the location lies above or below the level of orthostatic indifference. Notably, the highest percentage reductions with increasing G are found, in both RM and RI, at the level of the internal carotid artery. This suggests highly effective regulatory mechanisms precisely at one of the vessels supplying cerebral circulation—a region particularly sensitive to pressure variations. Conversely, the smallest percentage changes in both reflection parameters are observed at the level of the thoracic and abdominal aorta. Furthermore, in the lower limbs, wave reflections parameters remain strictly limited, despite the increase in hydrostatic loading.
These findings suggest the presence of an effective wave trapping mechanism, which not only appears to remain functional with increasing gravitational acceleration, but

may in fact become even more effective in attenuating the backward components of pressure waves.

5.5 Evaluation Metrics of gravity stress impact on Waveforms

Following the completion of wave decomposition at all relevant arterial locations and under each gravitational condition, the subsequent phase entails a detailed examination of the total pressure and flow rate waves, as well as of their forward and backward components. In particular, a comparative analysis of the resulting waveforms is required, using those obtained under the 1G condition as a reference benchmark.

To gain meaningful insights into the impact of altered gravity, it is essential not only to compare the waveforms qualitatively, but also to characterize their evolution quantitatively as gravity increases. This calls for the introduction of dedicated metrics capable of capturing relevant changes in waveform morphology, amplitude, timing, and interaction. Such metrics must be carefully defined to ensure they are sensitive to the specific hemodynamic alterations induced by varying gravitational loads, thus enabling a robust assessment of how wave propagation dynamics adapt across different gravitational regimes.

However, it is important to note that varying gravitational acceleration (G) leads to changes in the duration of a single cardiac cycle (RR interval), and that the waves obtained at different sites and under different G levels differ in terms of both mean value and variance. Consequently, in order to meaningfully compare the waveforms, it is necessary to normalize them with respect to both time (abscissa) and amplitude (ordinate) [13].

Regarding the temporal axis, the time variable is normalized by the duration of the cardiac cycle (RR) for each gravitational condition, resulting in a unified dimensionless time vector t':

$$t' = \frac{t}{RR} \quad \in \quad [0,1] \tag{5.1}$$

As for the amplitude, the z-score of each forward and backward pressure and flow rate wave — already normalized in time and generically denoted as $y'(t')$ — is computed. This transformation reduces each signal to a distribution with zero mean and unit standard deviation:

$$y'(t') = \frac{y(t') - \mu_y}{\sigma_y} \tag{5.2}$$

where μ_y denotes the mean value of $y(t)$ and σ_y represents the standard deviation of $y(t)$.

At this point, in order to perform a quantitative and meaningful comparison, the following metric, termed the Normalized Signal Difference (NSD), is introduced:

$$NSD = \int_0^1 |y'(t')_{1G} - y'(t')_{\#G}|\, dt' \quad \in \quad [0,2] \tag{5.3}$$

where $\#G$ indicates any gravitational condition other than 1G, for which the NSD would trivially be zero. Based on the NSD values obtained from the pairwise comparisons, waves of the same type (pressure/flow rate and total/forward/backward) and at the same site but under different G conditions can be compared both fully and quantitatively. Specifically, the closer the NSD value is to zero, the more similar the two waveforms are, indicating that they share the same shape. Conversely, the larger the NSD value (approaching 2), the greater the discrepancy between the two signals, reflecting a maximal alteration in waveform morphology.

5.5.1 Evaluation of gravity stress impact on total waveforms

In the following section, the waveform morphology of total pressure and flow waves, normalized in time and in amplitude, is examined as a function of gravitational acceleration. Figures 5.22, 5.23, 5.24 and 5.25 display the total pressure and flow rate normalized waveforms recorded at selected representative sites corresponding to different anatomical regions: the aortic root, right internal carotid artery (ICAr), iliac artery and anterior tibial artery. For each normalized waveform type, the curves obtained under seven equally spaced gravitational conditions—ranging from 0G to 3G in 0.5G increments—have been superimposed on the same graph and are distinguishable by color. Each pair of images corresponds to a specific site and qualitatively illustrates the effect of increasing gravity on the morphology of pressure and flow rate normalized waveforms.

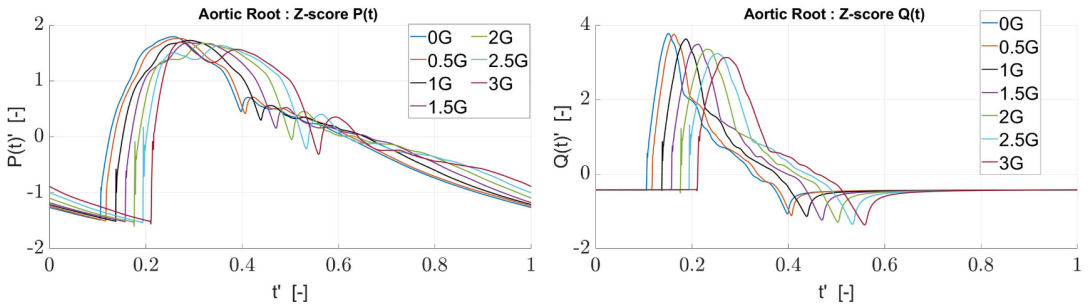

Figure 5.22: Time- and amplitude-normalized total pressure (left) and flow (right) waves at the aortic root site, shown for increasing gravity levels from 0G to 3G in 0.5G increments.

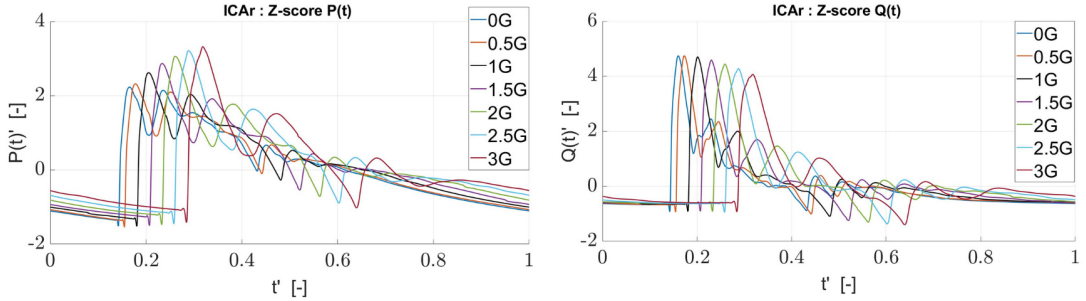

Figure 5.23: Time- and amplitude-normalized total pressure (left) and flow (right) waves in the right ICA, shown for increasing gravity levels from 0G to 3G in 0.5G increments.

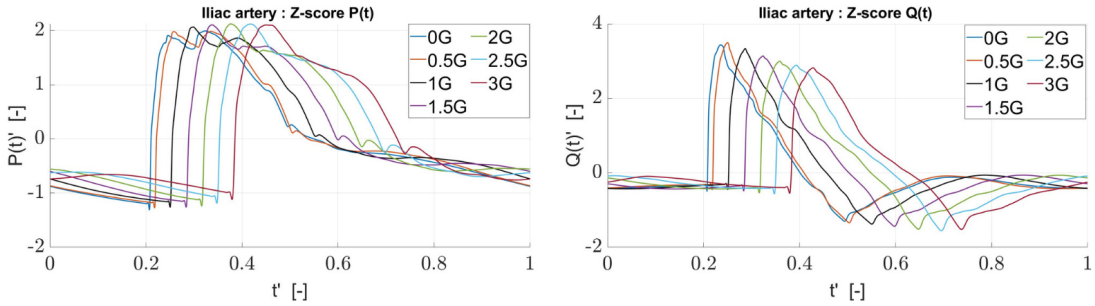

Figure 5.24: Time- and amplitude-normalized total pressure (left) and flow (right) waves in the iliac artery, shown for increasing gravity levels from 0G to 3G in 0.5G increments.

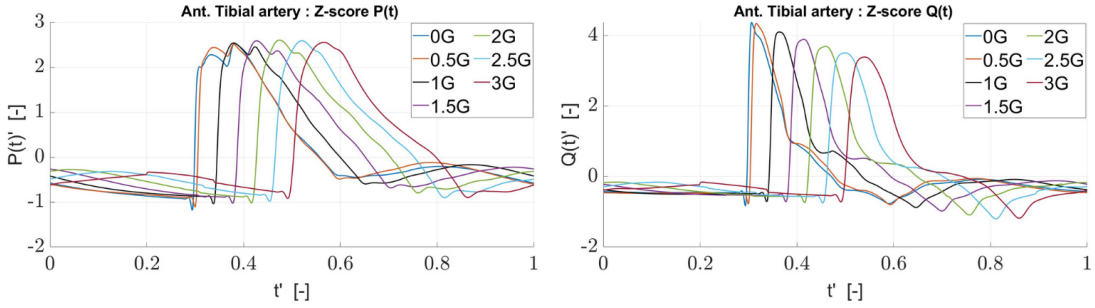

Figure 5.25: Time- and amplitude-normalized total pressure (left) and flow (right) waves in the anterior tibial artery, shown for increasing gravity levels from 0G to 3G in 0.5G increments.

As gravitational acceleration increases, a preliminary site-by-site inspection reveals that the normalized total waveforms often do not exhibit macroscopic alterations in shape, but are primarily affected by a temporal phase shift. For instance, the wave foot—typically well-defined and easily identifiable—systematically shifts toward higher dimensionless time values as the gravitational load increases, across all sites examined. In fact, under gravitational conditions more intense than 1G, both pressure and flow rate waves appear phase-shifted with respect to the reference condition (1G), specifically showing a delay relative to it. Conversely, for g/g_0 values lower than unity, the corresponding waves are found to be in advance. This observation is confirmed not only in the cases illustrated in figures 5.22, 5.23, 5.24 and 5.25, but consistently across all total signals and for all gravitational conditions evaluated within the 0G–3G range.

In order to highlight these aspects related to the phase shift of the signals with respect to the 1G baseline, it was deemed appropriate to assign a sign to the NSD values calculated according to the definition 5.3: positive for temporal shifts corresponding to waves leading in phase, and negative for waves lagging in phase. Figures 5.26 and 5.27 report the trends of signed NSD values corresponding to the different arterial sites analyzed. The computation was performed across the entire range of gravitational accelerations investigated, with an incremental step of 0.1G. Each arterial site is associated with a distinct line style and color, as well as specific markers, to allow for clear differentiation.

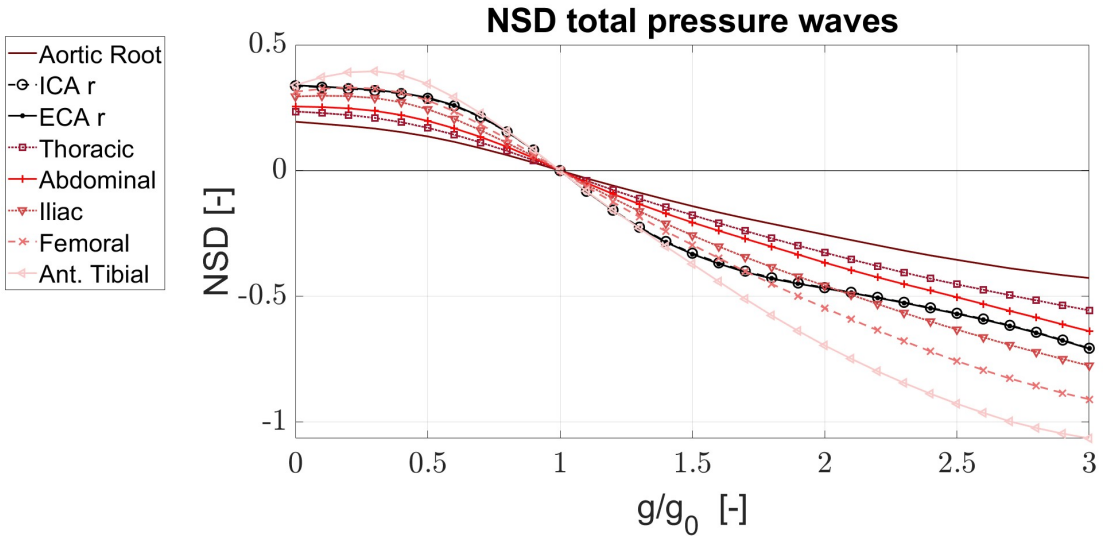

Figure 5.26: NSD signed trend computed for normalized total pressure waves for different gravity levels, ranging from 0G to 3G. Each different arterial site is described through a specific line style and colour, as well as a distinct marker.

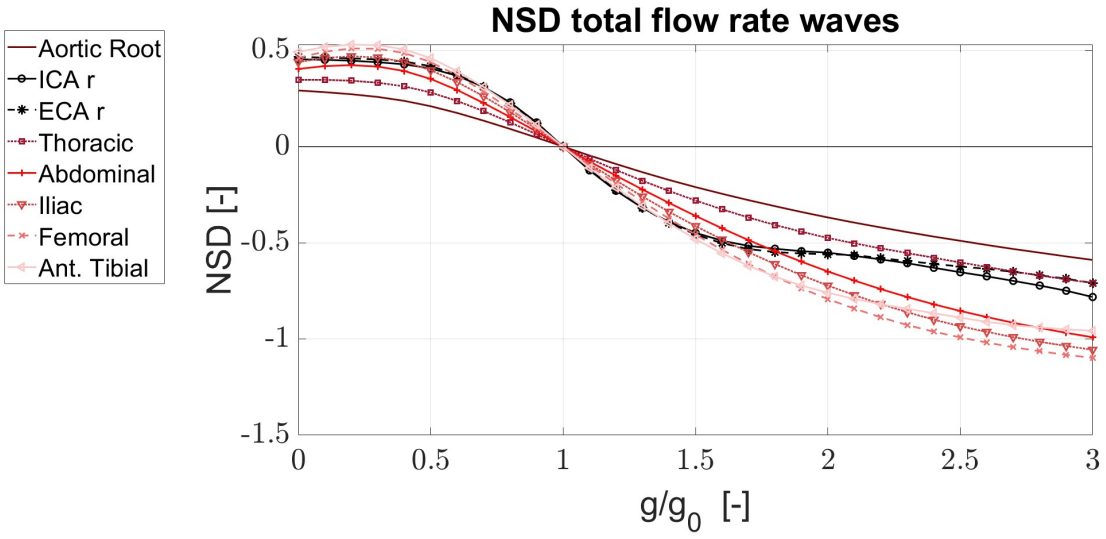

Figure 5.27: NSD signed trend computed for normalized total flow rate waves for different gravity levels, ranging from 0G to 3G. Each different arterial site is described through a specific line style and colour, as well as a distinct marker.

First, it can be stated that the NSD values for both flow rate and pressure waves fall within a rather similar range. Overall, it is evident that the aortic site represents, in both cases, the location exhibiting the least waveform distortion,

under conditions of both microgravity and hypergravity. In both cases, as the sites move progressively farther from the central region, there is a clear increase in the absolute NSD values, from the aortic root to the femoral artery. The anterior tibial artery adheres to this pattern in the case of total pressure waves (indeed showing the highest absolute NSD values), but deviates from it in the case of flow rate waves, where between 2G and 3G it exhibits a more stabilized and contained trend compared to the femoral and iliac sites.

With regard to the right internal and external carotid arteries, located above heart level, they display nearly overlapping trends in terms of NSD, both for pressure and for flow rate waves. Specifically, both exhibit a plateau-like behavior in the acceleration range between 0G and 0.5G, followed by a reduced-slope trend between 1.7G and 3G. This flattening under hypergravity conditions is particularly evident for total flow rate waves, underscoring the effectiveness of cerebral regulatory mechanisms in limiting alterations in blood flow within the vessels supplying the extra- and intracranial circulation. Across the 0G–0.5G range, all sites display a tendency to plateau in terms of both pressure and flow rate NSD. Interestingly, in the case of pressure waves at the anterior tibial artery, the NSD trend suggests the emergence of a mild peak between 0G and 0.5G, which, however, tends to dampen at the exact 0G condition. The stabilized NSD behavior observed for g/g_0 values below 0.5 highlights the absence of symmetry with respect to the corresponding hypergravity interval. Indeed, all sites exhibit higher absolute NSD values at 2G compared to 0G, and this asymmetry becomes progressively more pronounced with increasing distance of the site from the central region.

That said, the analysis conducted thus far has been limited to the computation of the NSD value through the integration of the absolute difference between the analyzed signal and the reference one (1G). However, the clear phase shift observed in flow rate and pressure waves with respect to the baseline condition introduces an additional consideration that warrants attention. In fact, phase shifting, even when not accompanied by an actual modification of waveform morphology, leads to an increase in the NSD value, an increase that must nevertheless be regarded as "spurious" with respect to the sought-after information on waveform shape variation. Based on this observation, a preliminary phase-alignment procedure was implemented to account for this shift and isolate waveform shape changes. Specifically, for each anatomical site and for each type of normalized total wave (pressure and flow), a cross-correlation analysis was performed between the waveforms associated with each G-level and the reference waveform at 1G. From the cross-correlation, the dimensionless time lag corresponding to the maximum correlation coefficient was extracted, allowing identification of the optimal temporal shift required to achieve the best alignment with the baseline waveform. This shift is signed, thereby

preserving critical information on whether the waveform in question leads or lags the 1G reference. A positive shift indicates that the waveform is temporally advanced relative to the baseline and must be moved forward in time, whereas a negative shift implies a delayed waveform that requires translation toward smaller dimensionless time values. Following this phase-alignment process, the waveforms at different G-levels were translated along the dimensionless time axis to optimally overlap with the 1G reference waveform. This allowed subsequent calculation of the Normalized Signal Difference (NSD), as previously defined, with the confidence that this shape metric was not altered by mere temporal misalignment.

As an illustrative example, figures 5.28 and 5.29 show the trends at the aortic root site of the total pressure and flow rate normalized waveforms corresponding to the various gravitational conditions, each compared individually with the reference signal (1G). For each normalized waveform, the reference wave, the original (unaligned) wave, and the optimally shifted wave are displayed. Additionally, next to each shifted signal, the signed dimensionless shifting time (t_{shift}) and the related NSD value, computed between the shifted signal and the 1G reference, are reported.

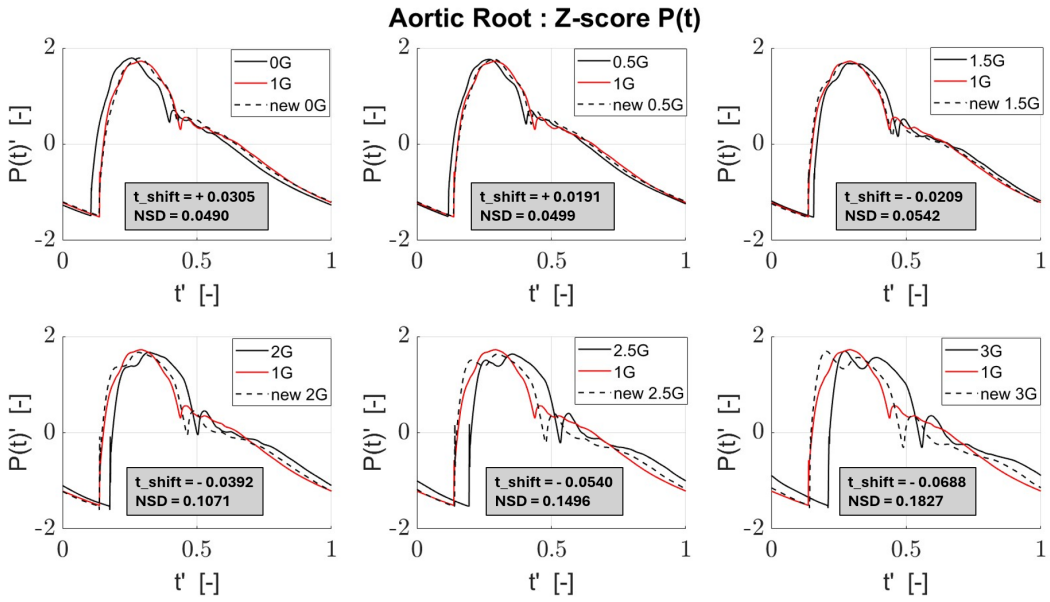

Figure 5.28: Phase alignment of normalized total pressure normalized waveforms wrt 1G reference signal at aortic root. The red curves represent the 1G baseline waves; the solid black curves represent the normalized waveforms corresponding to the various gravitational conditions (one per subplot); the dashed black curves represent the same waveforms after being temporally shifted to ensure optimal overlap with the 1G baseline.

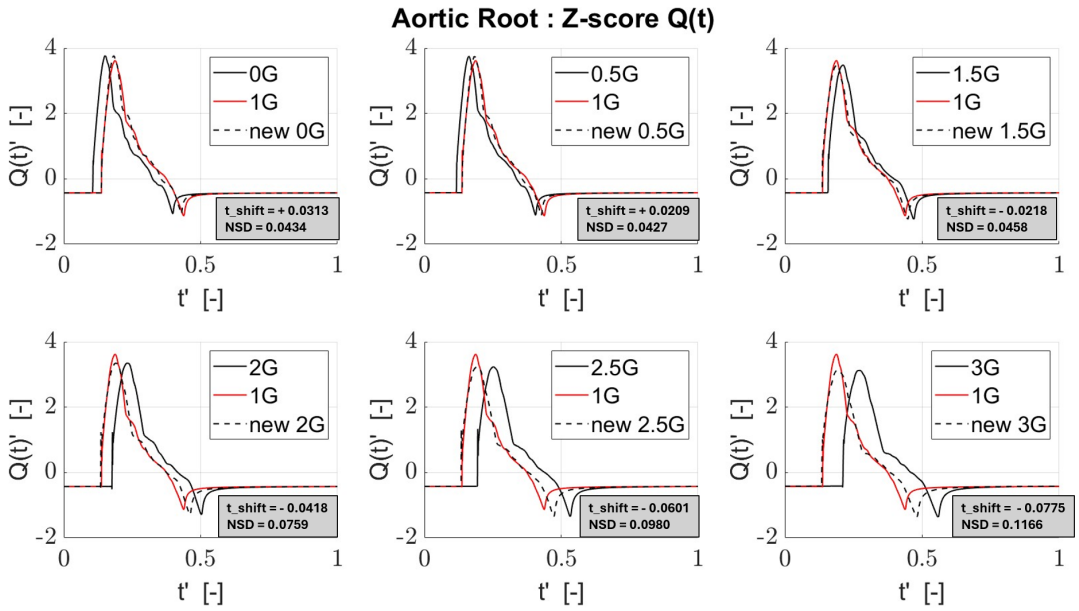

Figure 5.29: Phase alignment of normalized total flow rate normalized waveforms wrt 1G reference signal at aortic root. The red curves represent the 1G baseline waves; the solid black curves represent the normalized waveforms corresponding to the various gravitational conditions (one per subplot); the dashed black curves represent the same waveforms after being temporally shifted to ensure optimal overlap with the 1G baseline.

In the case of the aortic root, figures 5.30 and 5.31 present the trends of the NSD values computed for the total pressure and flow rate waveforms, both before (light green line – ORIGINAL) and after (dark green line – SHIFTED) the phase-alignment process. Prior to alignment, NSD was calculated using the normalized waveforms in their original form, without any temporal shifting with respect to the same 1G baseline. By definition, the NSD values for all curves and waveform types are zero under the 1G condition, since this waveform serves as the reference.

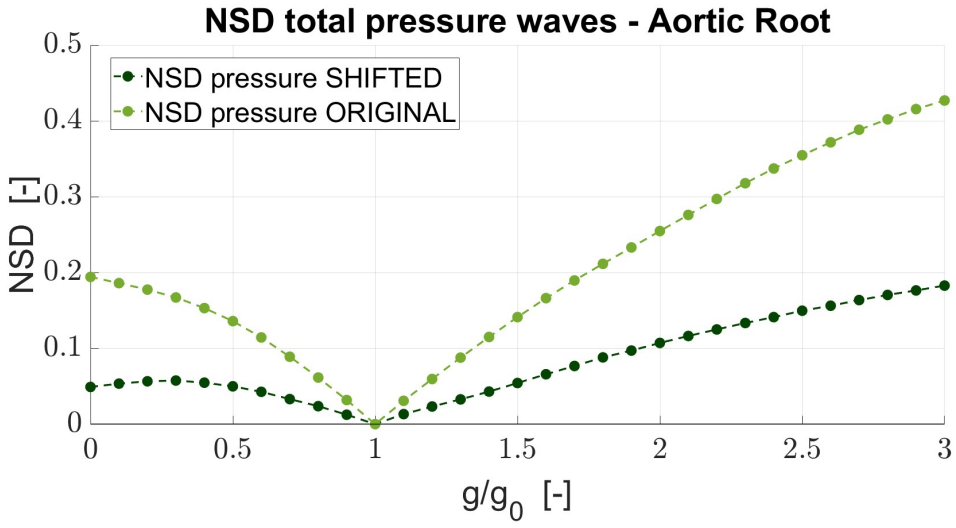

Figure 5.30: NSD trend computed before (light green – ORIGINAL) and after (dark green – SHIFTED) the phase-shifting process applied to the normalized total pressure waves at the aortic root site. NSD values are shown for different gravity levels ranging from 0G to 3G.

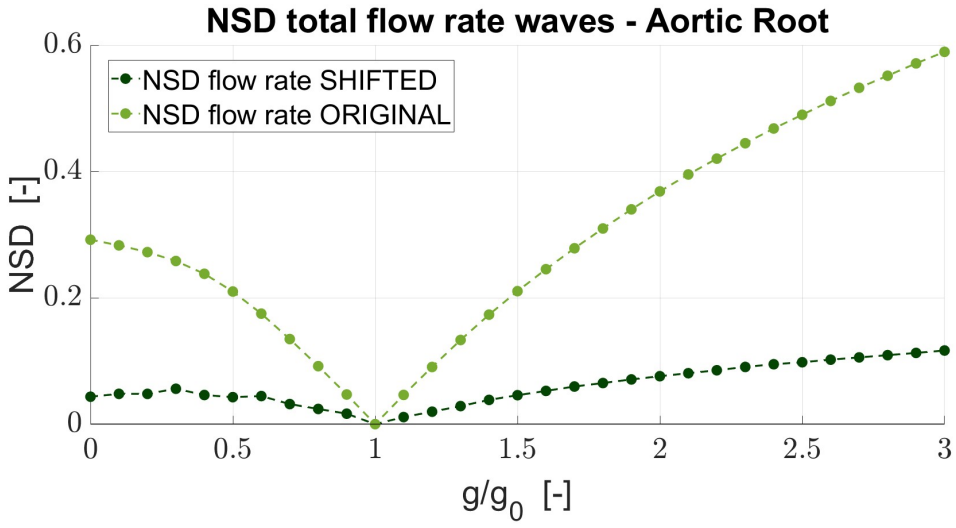

Figure 5.31: NSD trend computed before (light green – ORIGINAL) and after (dark green – SHIFTED) the phase-shifting process applied to the normalized total flow rate waves at the aortic root site. NSD values are shown for different gravity levels ranging from 0G to 3G.

From these trends, it becomes immediately evident that, following the phase-alignment procedure, the NSD values globally decrease. This confirms the necessity of aligning signals in time before conducting a quantitative comparison based on waveform deviation, such as through integrated differences.

To additionally account for the sign of the temporal misalignment, the right-hand plots in figures 5.32 and 5.33 show the trends of the time shifts (t-shift) associated with each total waveform, while the left-hand plots display the corresponding NSD values—again for the aortic root example. In order to retain information on whether the analyzed waveform leads or lags the reference, the NSD values have been assigned the same sign as the associated t-shift, even though NSD is inherently defined as a non-negative quantity. This approach allows for a more comprehensive interpretation of whether the waveform precedes or follows the reference in time. Both total pressure and total flow rate waveforms are represented below, referring to the aortic root site.

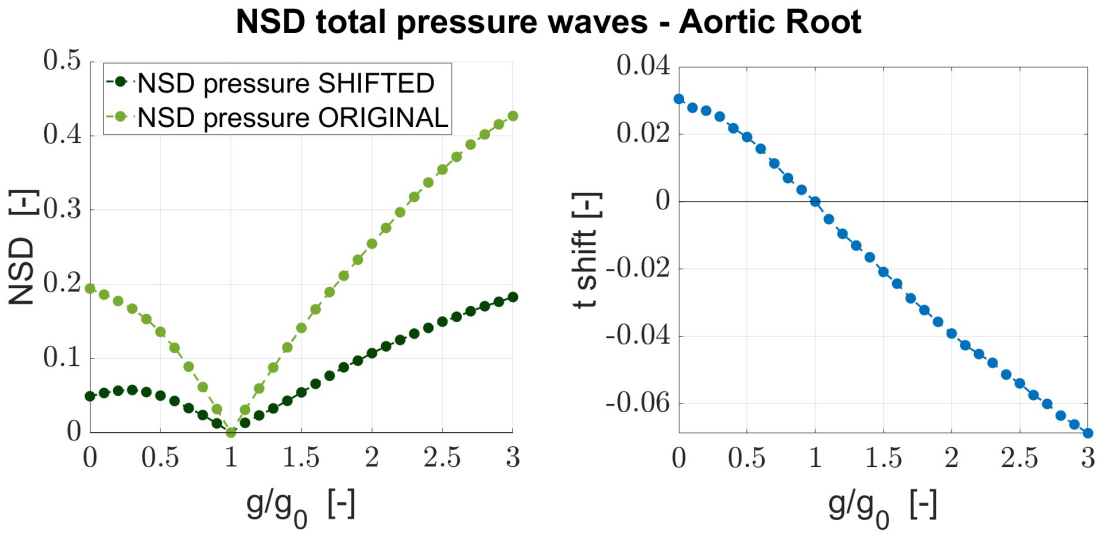

Figure 5.32: (Left) NSD trend before (ORIGINAL) and after (SHIFTED) the phase-shifting process applied to the normalized total pressure waves at the aortic root site, with respect to the 1G baseline. The NSD sign reflects the direction of the phase shift. (Right) signed phase shift time for each normalized total pressure waves at the aortic root site.

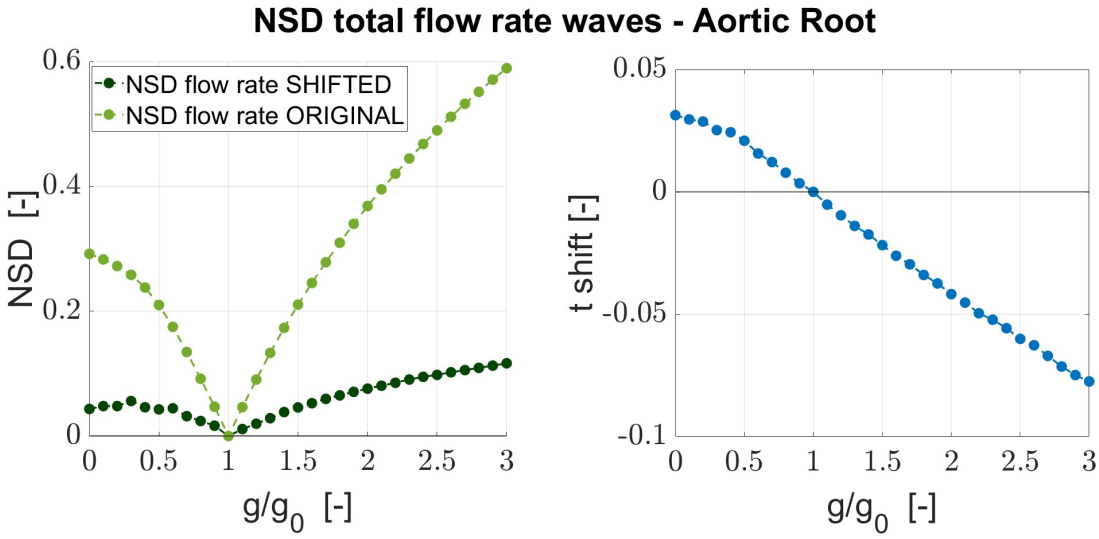

Figure 5.33: (Left) NSD trend before (ORIGINAL) and after (SHIFTED) the phase-shifting process applied to the normalized total flow rate waves at the aortic root site, with respect to the 1G baseline. The NSD sign reflects the direction of the phase shift. (Right) signed phase shift time for each normalized total flow rate waves at the aortic root site.

The plots clearly show that, for gravitational loads below 1G, both pressure and flow rate waveforms occur in advance relative to the baseline. Conversely, as gravitational acceleration increases beyond 1G, these same waveforms exhibit a progressively increasing delay. Indeed, moving further away from the reference condition results in a larger absolute time shift, as illustrated by the increasing displacement of the waveform foot from the reference. Notably, this behavior is not limited to the aortic root, but is also consistently observed across the other arterial sites analyzed.

In the figure 5.34, the trends of NSD values for total pressure waves were reported, computed using waves that were rephased with respect to the 1G reference wave. Interestingly, the pressure waves exhibiting the greatest shape deviation from the baseline condition were those corresponding to the right ICA and right ECA. Moreover, these two sites displayed very similar NSD values, with nearly overlapping trends as a function of G. In contrast, aortic sites—namely the aortic root, thoracic aorta, and abdominal aorta—exhibited both closely matching NSD values and the lowest overall NSD values, indicating the smallest shape variation relative to the corresponding 1G pressure wave. Peripheral sites, such as the iliac, femoral, and anterior tibial arteries, also demonstrated very similar NSD trends among themselves and occupied an intermediate position between the carotid and

aortic NSD values. From these results, it appears that within the aorta, being closest to the heart, the shape variations of total pressure waves remain rather limited, with NSD values confined between +0.2 and -0.2. This contrasts with the behavior observed in more peripheral regions. In particular, waveform variations in the carotid vessels resulted in NSD values that were nearly double, in absolute terms, compared to those in central vessels.

Another noteworthy observation concerns the slope in the range between 0G and 0.5G. Within this microgravity interval, the NSD trends for all sites appeared nearly flat, with higher values for carotid sites and lower, more compact values for the remaining sites. Conversely, the segment between 0.5G and 1.5G exhibited the steepest negative slope across all sites, being most pronounced in the ICA and ECA and least steep in aortic sites. Furthermore, in the interval between 1.5G and 2G, instead of a mirrored behavior with respect to the 0G–0.5G range, a further decreasing trend was observed. This trend maintained a negative slope comparable to that of the 0.5G–1.5G segment. As G increased, the slope remained negative, indicating an increase in the absolute value of NSD, while suggesting a progressive reduction in slope across all sites. The carotid arteries, however, displayed the most pronounced negative slopes and appeared to maintain steep declines even at higher G values.

All these findings indicate, first and foremost, that the extent of waveform shape variation for total pressure waves does not exhibit symmetrical behavior in microgravity and hypergravity relative to the 1G baseline condition. In fact, excursions of ±1G from baseline do not yield equivalent NSD outcomes; rather, hypergravity conditions induce more pronounced waveform alterations. Additionally, vessels located closer to the cerebral region showed greater waveform distortion compared to those in other body regions, both central and peripheral, and did not exhibit any distinct plateauing behavior under hypergravity, unlike the stable NSD trends observed in microgravity (between 0G and 0.5G).

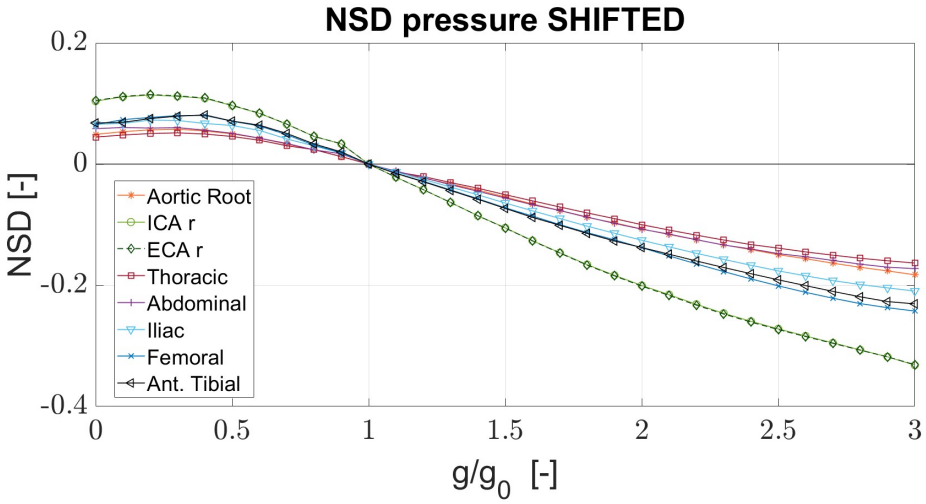

Figure 5.34: Trend of NSD values computed using pressure total waves phase-aligned with the reference signal (1G). Each arterial site is associated with a different color and a specific marker. The sign of NSD reflects the sign of the time shift applied to each analyzed wave.

Turning now to the shifting times used for rephasing the total pressure waves, which were instrumental in computing the NSD values, these adimensional times revealed particularly interesting trends reported in figure 5.35. Specifically, they exhibited a decreasing trend from 0G to 3G, effectively indicating an increase in the absolute value of NSD all the more significant as the gravitational conditions deviate from the 1G baseline. For gravitational accelerations below 1G, the shifting time appeared positive, reflecting waves that were phase-advanced with respect to the reference wave. For G values greater than 1, shifting times were negative, indicating delayed waves. Notably, the negative slope observed for each analyzed site remained approximately constant as G increased, within the 0.5G–3G interval, while being reduced in the 0G–0.5G range. This suggests that, in microgravity, temporal shifting is more limited and tends to plateau, whereas in hypergravity it reaches higher values and shows no signs of stabilization of the dimensionless phase-shift time.

For instance, in the case of the anterior tibial artery, a -1G excursion from baseline corresponds to a t_{shift} value just below 0.05. Conversely, a +1G excursion at the same site yields a t_{shift} value (in absolute terms) nearly twice as large, approximately -0.1. Furthermore, the negative slope of the shifting times across different sites became progressively steeper (i.e., more negative) with increasing distance between the site and the heart. Specifically, the shallowest slope was observed for the aortic root, while the steepest was associated with the anterior tibial artery. Carotid

sites were consistent with this trend, displaying a slope intermediate between those of the thoracic and abdominal aorta, which is consistent with their intermediate distance from the heart—despite being located in the opposite direction relative to the level of orthostatic indifference. From these findings, it can be inferred that the magnitude of the wave temporal delay is not influenced by whether the arterial site is located above or below heart level, but rather by its absolute distance from the heart.

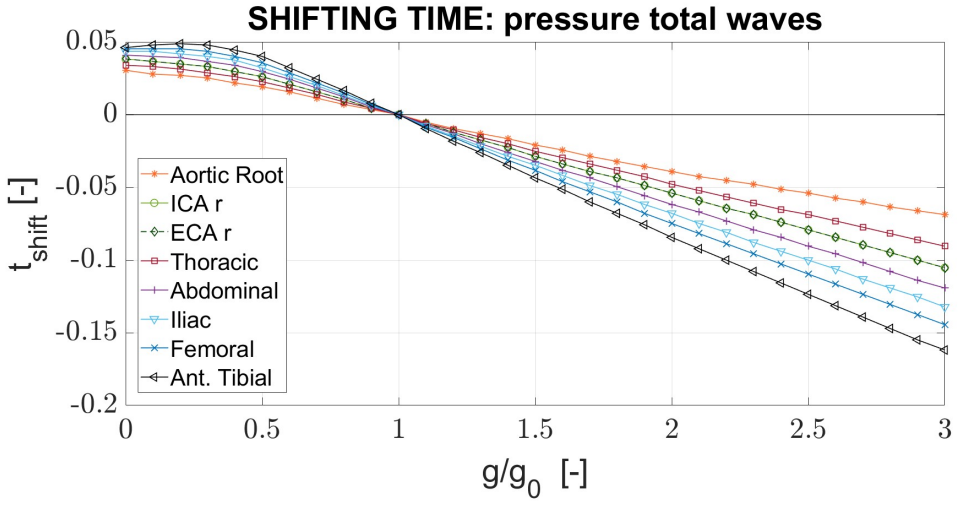

Figure 5.35: Trend of the rephasing time associated with each pressure total wave relative to the reference signal (1G). The shifting time corresponds to the value that ensures optimal overlap between each analyzed wave and the reference wave, for each site. Each arterial site is associated with a different color and a specific marker.

Turning now to the analysis of NSD trends for total flow rate waves (see figure 5.36), it is observed once again that the highest NSD values are associated with the right ICA and right ECA. These sites exhibit an almost constant trend between 0G and 0.5G, while between 0.5G and 1.5G they display the steepest negative slope among all analyzed sites. For G values greater than 1.5G, these sites continue to show the highest absolute NSD values, although the negative slope progressively decreases, suggesting the emergence of a potential plateau under hypergravity conditions. Furthermore, unlike what was observed for total pressure waves, the behavior of right ECA and right ICA diverges slightly in this case, with the ICA exhibiting a greater waveform alteration compared to the ECA. This may be related to the functional difference between the two vessels, as the ICA serves the delicate role of supplying one of the main inputs to the cerebro-ocular region. Conversely, the aortic root in this case shows the lowest absolute NSD

values, indicating that, near the blood jet outlet, the shape of the total flow rate wave is minimally affected by changes in gravitational acceleration. Regarding the remaining sites, they exhibit an interesting pattern in the interval between 0G and 0.5G, where a slight increase in NSD values is observed with increasing G, followed by a generally decreasing trend in the gravitational range between 0.5G and 3G. For G values above 1.5G, the slopes of the NSD trend for these sites begin to gradually decrease in magnitude, indicating a possible plateau under extreme hypergravity conditions. Once again, a ±1G excursion from baseline does not yield symmetric behavior with respect to the 1G wave, as NSD values under 2G conditions are higher in absolute terms than those observed under 0G. These observations suggest a stronger effect of hypergravity on waveform distortion, both for total pressure and total flow rate waves, compared to the impact observed under microgravity.

Compared to pressure wave trends, flow rate waves at the aortic level present greater variability in behavior under hypergravity. Specifically, flow rate waves at the aortic root undergo less significant shape changes between 1G and 3G compared to pressure waves at the same site. Conversely, in the thoracic and abdominal aorta, flow rate waves are more affected than pressure waves over the same gravitational range. This results in a greater behavioral difference between the aortic root and the other aortic sites, which appear more similar to peripheral sites such as the iliac, femoral, and tibial arteries.

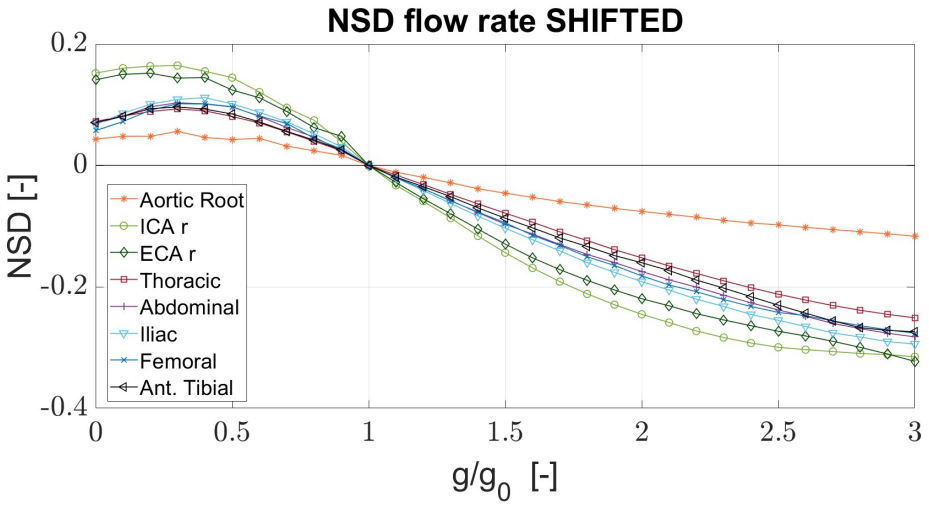

Figure 5.36: Trend of NSD values computed using total flow rate waves phase-aligned with the reference signal (1G). Each arterial site is associated with a different color and a specific marker. The sign of NSD reflects the sign of the time shift applied to each analyzed wave.

Furthermore, the analysis of shifting times for total flow rate waves reveals behavior very similar to that observed for total pressure waves, as reported in figure 5.37. Here as well, a stabilization of temporal shifting is seen within the gravitational range between 0G and 0.5G, while for higher gravitational accelerations, a clearly monotonic decreasing trend is observed. As before, the magnitude of the temporal shift increases progressively with G, and the slope becomes more pronounced as the distance of the site from the heart increases. Again, under microgravity conditions, flow rate waves appear advanced relative to the baseline 1G condition, regardless of the site considered, while at higher gravitational accelerations they appear delayed relative to the corresponding 1G wave. Total flow rate waves at carotid sites (right ICA and right ECA) exhibit practically identical shifting times, consistent with the fact that they are located at approximately the same absolute distance from heart level. As with total pressure waves, the magnitude of the shifting does not appear to be influenced by whether the site is located above or below the level of orthostatic indifference, but rather by its absolute distance from the heart.

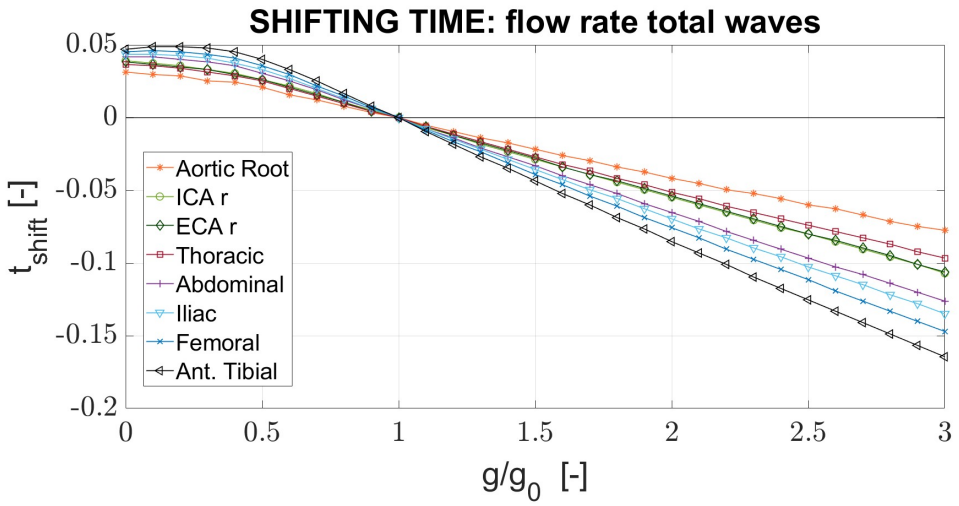

Figure 5.37: Trend of the rephasing time associated with each flow rate total wave relative to the reference signal (1G). The shifting time corresponds to the value that ensures optimal overlap between each analyzed wave and the reference wave, for each site. Each arterial site is associated with a different color and a specific marker.

At this point, attention is briefly directed to the analysis of the differences between the dimensionless phase-shift times characterizing flow rate waves and those characterizing pressure waves. In the figure below, four arterial sites are considered (aortic root, right internal carotid artery, iliac artery, and anterior tibial artery), and for each site, the dimensionless shifting times for normalized flow

rate waves (orange) and for pressure waves (blue) are reported as a function of gravitational acceleration.

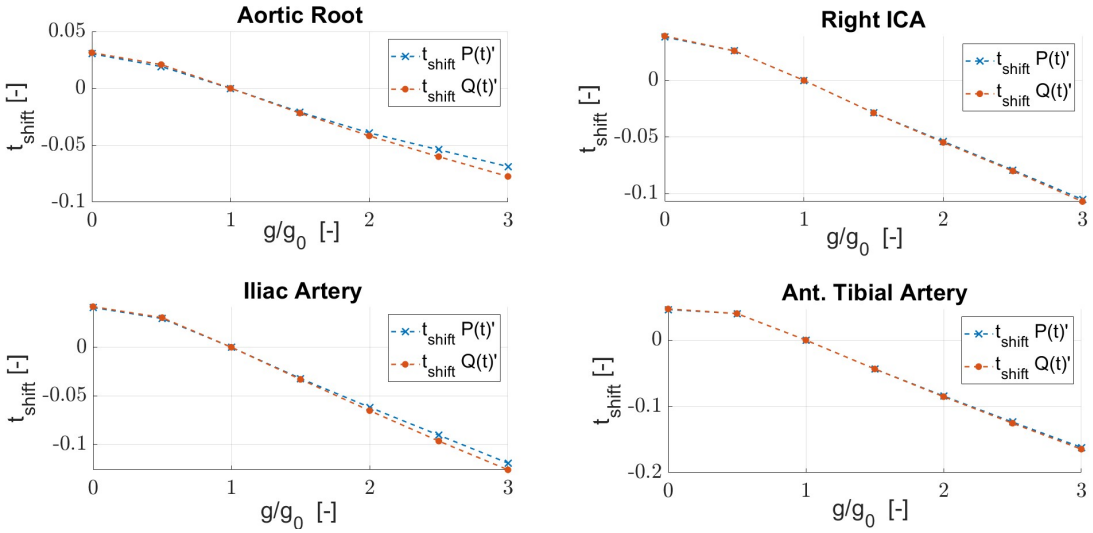

Figure 5.38: Trend of the dimensionless phase-shift time for total pressure and flow rate waves as a function of gravitational acceleration (g/g_0), across four different arterial sites: the aortic root, right internal carotid artery, iliac artery, and anterior tibial artery. Blue curves refer to pressure waves, while orange lines refer to flow rate waves.

From the figure 5.38, it can be observed that, for the right internal carotid artery and the anterior tibial artery, the dimensionless phase-shift trends of normalized pressure and flow rate waves are nearly perfectly superimposed throughout the entire range of gravitational accelerations. In contrast, for the aortic root and the iliac artery, the trends begin to diverge slightly starting from the 1.5G condition. Moreover, the magnitude of this divergence between the two curves progressively increases with increasing gravitational acceleration. Specifically, in the gravitational range between 1.5G and 3G, the shifting times associated with the total normalized pressure waves at the level of the aortic root and the iliac artery are slightly lower in absolute value, that is, less negative, than those of the corresponding flow rate waves. Since the dimensionless times in question are negative for g/g_0 values greater than 1, it follows that both flow rate and pressure waves are delayed with respect to their baseline counterparts; however, the extent of this delay is not the same as G increases. Indeed, for g/g_0 values exceeding 1.5, pressure waves require a smaller backward temporal shift to be rephased to the baseline 1G signal compared to flow rate waves, at the same site and under the same gravitational condition. This result suggests the emergence of a slight phase mismatch, with increasing G,

between pressure and flow rate signals in certain sites (notably the aortic root), particularly under extreme hypergravity conditions. More specifically, it reveals a slight delay of the flow rate wave relative to its corresponding pressure wave.

Conversely, under microgravity conditions, the rephasing times appear nearly identical for total flow rate and pressure waves across all the sites shown in the figure. At the level of the anterior tibial artery and the internal carotid artery, in particular, the phasing times remain practically identical for total pressure and flow rate waves over the full range of gravitational conditions. These findings therefore highlight an additional point of interest: the potential onset of a phase shift between pressure and flow rate signals, which appears to be localized exclusively at the central level and extending as far as the iliac bifurcation.

5.5.2 Evaluation of gravity stress impact on decomposed waveforms

After analyzing the effect of gravitational stress on the total pressure and flow waves, attention is now directed toward investigating the behavior of the decomposed flow and pressure waves as a function of g. As previously illustrated, each total wave can be decomposed into two distinct components, a forward and a backward wave, which respectively represent the forward and backward contributions to the overall signal. This decomposition was carried out after computing the characteristic impedance values for each arterial site of interest and for each gravitational condition, in accordance with the previously illustrated water hammer equation.

The results were obtained across the entire range of gravitational conditions, from 0G to 3G, with an incremental step of 0.1G. Such a finer resolution in terms of gravitational acceleration allows for a more precise and comprehensive assessment of the gravitational influence on the decomposed waves, enabling the identification of smoother and more detailed trends.

Figures 5.39 and 5.40 report representative trends of the normalized forward and backward pressure waves at the different arterial sites considered, for four distinct gravitational conditions: 0G, 1G, 2G, and 3G. The wave corresponding to the 1G condition is highlighted in black and plotted with greater thickness, as it serves as the baseline reference for the subsequent analysis of waveform variations with g.

It should be emphasized that all the waveforms presented have been previously normalized with respect to both the temporal dimension and the amplitude. Indeed, when investigating possible variations in phase and waveform morphology, it is crucial to eliminate differences arising from the varying cardiac cycle duration across

g conditions, as well as from discrepancies in the mean and standard deviation of the signals.

In particular, the analysis will focus exclusively on the forward and backward components of the pressure waves, as the results obtained from the decomposed flow rate waves would be entirely analogous and therefore redundant. Specifically, the NSD values calculated for the forward waves of pressure and flow rate are identical at each site, and the same holds true for the backward waves. This outcome is not surprising: given that the characteristic impedance is fixed for each site and each gravitational condition, the water hammer equation implies that the decomposed forward (and similarly the backward) pressure and flow rate waves differ only by a rigid translation. Consequently, upon normalization, both the forward (or backward) pressure and flow rate signals exhibit zero mean and unit standard deviation, and more importantly, they share an identical waveform, being related to one another by a multiplicative constant (i.e., Z_c).

This observation does not hold, however, for the total pressure and flow rate waves (P_t, Q_t), as discussed in the previous section. Total waves result from different combinations of the decomposed flow rate components (Q_f, Q_b), which leads to genuine waveform alterations rather than a mere signal translation, as illustrated below:

$$P_t = P_f + P_b = Z_c \cdot (Q_f - Q_b) \qquad Q_t = Q_f + Q_b \tag{5.4}$$

In light of this, reporting also the forward and backward flow rate waves, together with their corresponding NSD values, would not provide any additional insight beyond what is already observed for the pressure waves. For this reason, the analysis has been restricted to the decomposed pressure waves, with the aim of determining which signal component is more significantly affected by orthostatic loading in terms of waveform variation. By computing the NSD values (always using the 1G condition as the baseline reference) it is possible to discern whether the forward or the backward wave undergoes the larger deformation. It should nevertheless be recalled that the total waves result from different combinations of the decomposed components, and therefore a high NSD value in a single component does not necessarily translate into a high NSD value in the corresponding total signal.

For the purpose of qualitatively illustrating the effect of varying gravitational acceleration on the decomposed waves, figures 5.39 and 5.40 present the trends of the normalized forward and backward pressure wave components across the various arterial sites of interest. Specifically, for each site, the waves corresponding to four distinct gravitational conditions are shown: 0G (light blue line), 1G (black line), 2G (yellow line), and 3G (purple line). The 1G reference condition is emphasized with a thicker black line, in order to clearly highlight the baseline under each different condition.

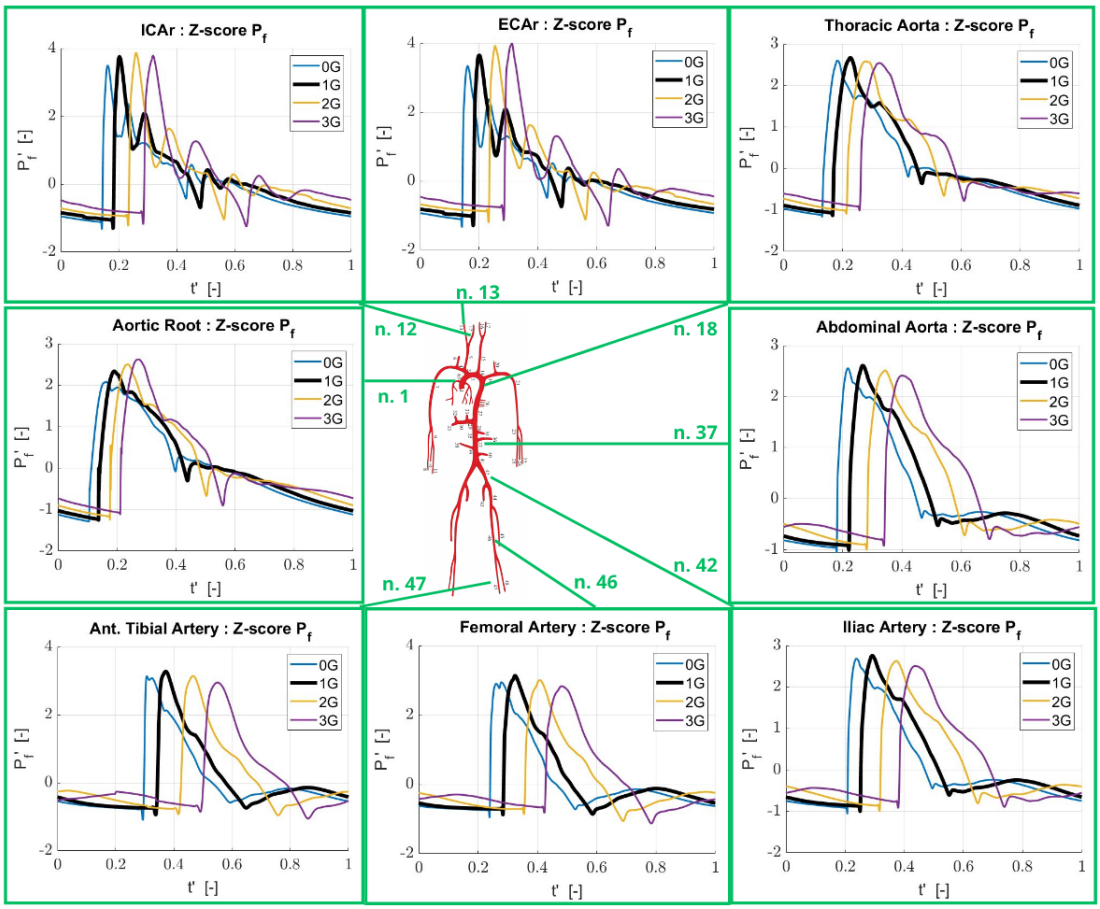

Figure 5.39: Trend of normalized forward pressure wave components across the various arterial sites of interest. For each site, the waves corresponding to four different gravitational conditions are shown: 0G (light blue line), 1G (black line), 2G (yellow line), and 3G (purple line). The 1G reference condition is highlighted using a thicker black line.

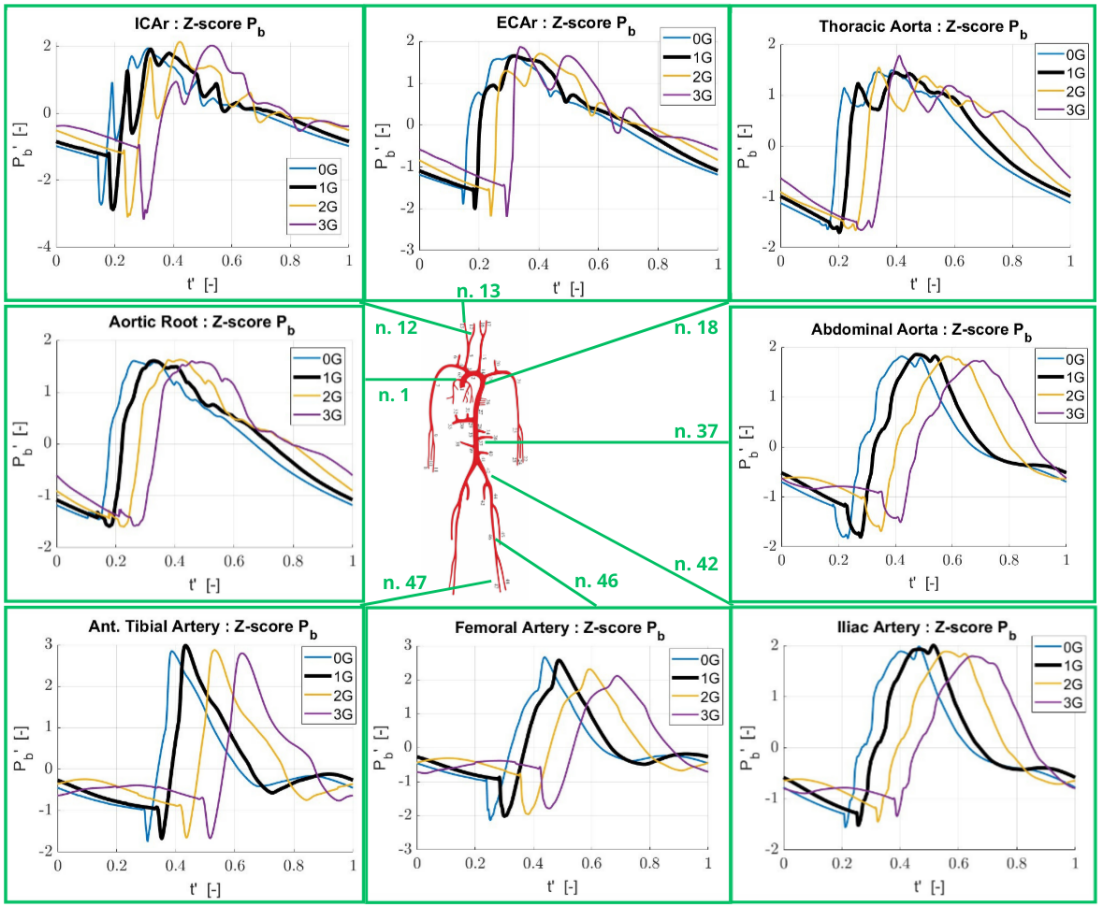

Figure 5.40: Trend of normalized backward pressure wave components across the various arterial sites of interest. For each site, the waves corresponding to four different gravitational conditions are shown: 0G (light blue line), 1G (black line), 2G (yellow line), and 3G (purple line). The 1G reference condition is highlighted using a thicker black line.

A qualitative assessment of the normalized forward and backward pressure waveforms at the different arterial sites considered reveals, first of all, that the amplitudes of the forward waves are consistently greater than those of the backward waves across all sites. This observation highlights that the backward contribution is less pronounced than the forward contribution, irrespective of both the arterial location and the gravitational acceleration applied. Moreover, the internal and external carotid arteries exhibit the most irregular waveform patterns, in both the forward and backward components. This characteristic is consistently observed under varying gravitational conditions, ranging from microgravity to the hypergravity regime considered.

When qualitatively examining the forward and backward waveforms, it can generally be observed that the wave foot is much more pronounced in the case of retrograde waves compared to forward waves. In fact, the backward components exhibit a sharper reduction in transmural pressure in the instants preceding the wavefront arrival, whereas this decrease is considerably milder for the forward waves. However, this difference between the decomposed components is less marked at central sites located at the level of the heart, namely the aortic root and the thoracic aorta, where even the backward signals display wave feet characterized by only a modest reduction in pressure prior to the steep increase associated with ventricular contraction.

Overall, based on a preliminary qualitative assessment, it can be stated that changes in gravitational acceleration do not cause a substantial alteration in waveform morphology, but rather preserve a forward and backward wave profile that remains broadly comparable to the 1G reference at each site. Nonetheless, after the normalization process, it becomes clear that gravitational accelerations different from 1G induce a phase shift in the signal, which is also evident in the decomposed waves analyzed here, in line with what has been observed for the total signals. Specifically, for accelerations greater than 1G, both forward and backward waves experience a phase delay relative to the reference signal, whereas for accelerations between 0G and 1G, the signal is advanced. This implies, therefore, that the phase-shift behavior of the decomposed signals with varying gravity mirrors that of the corresponding total signals.

At this stage, however, a quantitative analysis is carried out to assess the effect of varying gravitational acceleration on waveform morphology, focusing on the normalized decomposed signals. For this purpose, the computation of the NSD value was introduced here as well for each site and for every gravitational condition, taking the normalized pressure signal under 1G as the reference. The latter was calculated according to the definition 5.3, with the addition of further information related to the phase shift, expressed through the sign attributed to the NSD. Signals leading the baseline are associated with a positive sign, i.e., NSD values greater than zero, whereas delayed signals are associated with negative NSD values.

Figures 5.41 and 5.42, reported below, show the trends of signed NSD associated with the normalized forward and backward pressure waves, for all arterial sites analyzed and across the full range of gravitational accelerations, from 0G to 3G. As in the case of the total signals, the analysis was performed over 31 distinct gravitational conditions, adopting an incremental step of 0.1G to identify a trend as continuous and smooth as possible. Each site is represented by a curve with

a different color and marker, facilitating the interpretation of the various NSD patterns.

From the observation of the NSD trends for both forward and backward waves, it becomes evident that no symmetry exists with respect to the 1G reference condition, which, as expected, is characterized by NSD equal to zero in all cases. Indeed, as already noted for the total signals, the hypergravity condition is associated with larger absolute values of NSD compared to the microgravity case. In particular, when considering the absolute NSD values at 0G and 2G (i.e. a variation of ±1G from the baseline condition), it is found that the values at 2G are consistently higher than those at 0G across all arterial sites analyzed. This result indicates that waveform deformation is more pronounced under hypergravity than under microgravity.

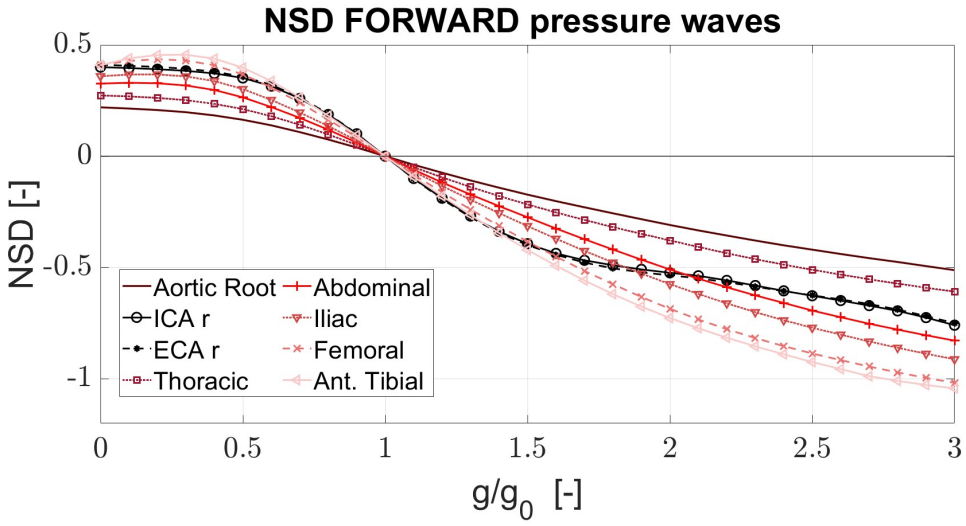

Figure 5.41: NSD trends of the forward components of the pressure signal with respect to the 1G baseline. Each curve corresponds to a specific arterial site analyzed and is distinguished by different colors and markers. The trends were obtained by evaluating the NSD values over the full range of gravitational conditions, from 0G to 3G, with an incremental step of 0.1G.

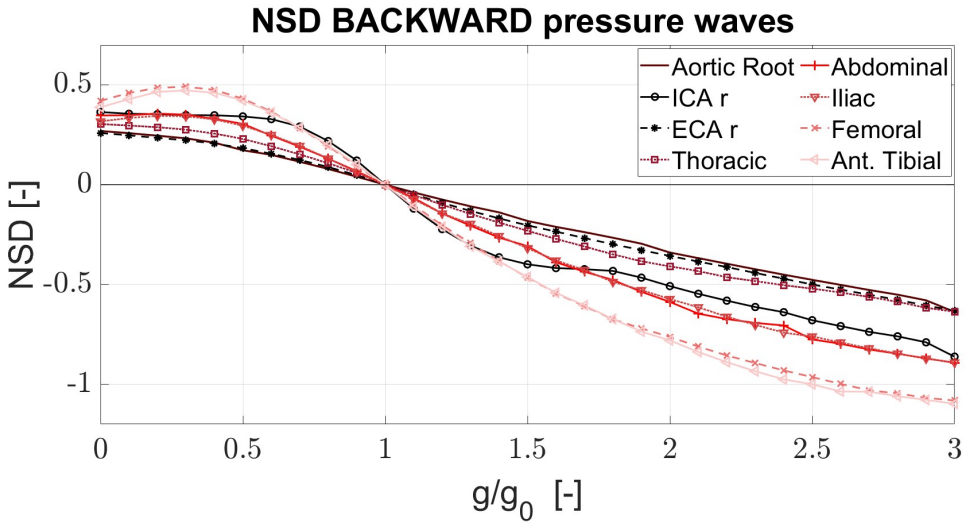

Figure 5.42: NSD trends of the backward components of the pressure signal with respect to the 1G baseline. Each curve corresponds to a specific arterial site analyzed and is distinguished by different colors and markers. The trends were obtained by evaluating the NSD values over the full range of gravitational conditions, from 0G to 3G, with an incremental step of 0.1G.

Furthermore, focusing on the sites ranging from the aortic root to the anterior tibial artery, it can be observed that greater waveform deformation occurs progressively at sites farther away from the central region. This behavior is particularly evident in the case of forward waves, where the different trends appear clearly separated, but it is also discernible in the backward signals, even though the abdominal and iliac sites (similarly to the tibial and femoral) are much more closely clustered.

Another noteworthy aspect emerges when examining the trends across the entire range of gravitational accelerations: while within the interval between 0G and 1G the NSD values tend to plateau, in the interval between 1G and 3G they generally display a continuous decreasing trend, in almost all sites analyzed. These results, similar to what was observed for the total signals, seem to suggest that the extent of waveform deformation, for both forward and backward signals, tends to stabilize and remain limited under microgravity, whereas it becomes more significant and steadily increases as g rises.

In addition, the distal sites of the femoral and anterior tibial arteries exhibit a slightly increasing trend in NSD values between 0G and 0.3G, followed by a decreasing trend for g/g_0 values greater than 0.3, in both forward and backward cases.

The presence of a local maximum of NSD within the range 0G–1G is consistent with what was previously observed for the total signals and, interestingly, does not reappear in a symmetric manner within the gravitational range between 1G and 2G.

With regard to the right internal and external carotid arteries, both were highlighted in the graphs using black curves, distinguished by two different types of markers. Their behavior in terms of NSD differs slightly from that observed at the other arterial sites located at or below the level of the heart. Specifically, it is immediately apparent that, in the case of forward signals, the ICAr and ECAr exhibit almost overlapping NSD trends, whereas in the case of backward signals the two arteries display distinct behaviors across the entire gravitational range. For the forward waves, within the interval between 0G and 1G, they show relatively high NSD values, second only to the most peripheral sites (femoral and tibial arteries), while nonetheless exhibiting a clear plateau behavior between 0G and 0.5G. For g/g_0 values greater than 1, both carotid sites display an increase in the absolute value of NSD for forward signals in the range 1G–1.5G, followed by a tendency to stabilize under hypergravity conditions, deviating from the behavior observed at all other sites. This result seems to suggest the effectiveness of regulatory mechanisms, both in microgravity and hypergravity, which tend to dampen and limit waveform variations of the forward pressure component in the carotid arteries, located above the level of the heart.

When considering the backward signal across the entire range of gravitational accelerations, the right internal carotid artery is associated with higher absolute NSD values compared to the right external carotid artery. The latter, in particular, exhibits an NSD trend almost overlapping with that of the aortic root, thereby showing a very limited waveform variation even under substantial changes in orthostatic load. Unlike the forward case, the NSD trend for the backward signal of the ECAr stabilizes at lower absolute values, indicating that waveform variations in the retrograde component are less significant than those occurring in the forward signal. The ICAr, on the other hand, also in the backward case, exhibits an NSD trend rather similar to that observed for the forward component.

This latter aspect is highlighted in figure 5.43, where the NSD trends for forward and backward waves at the same site are compared for selected vessels. In this way, the analysis aims to determine more precisely which of the two components (forward or backward) is more affected by gravity in terms of waveform deformation. Figure — displays the NSD trends computed with respect to the 1G baseline, showing for each site both the forward signal (red line) and the backward signal (green line). Solid lines connect the points obtained from the numerical solution over the 0G–3G range, with an incremental step of 0.1G.

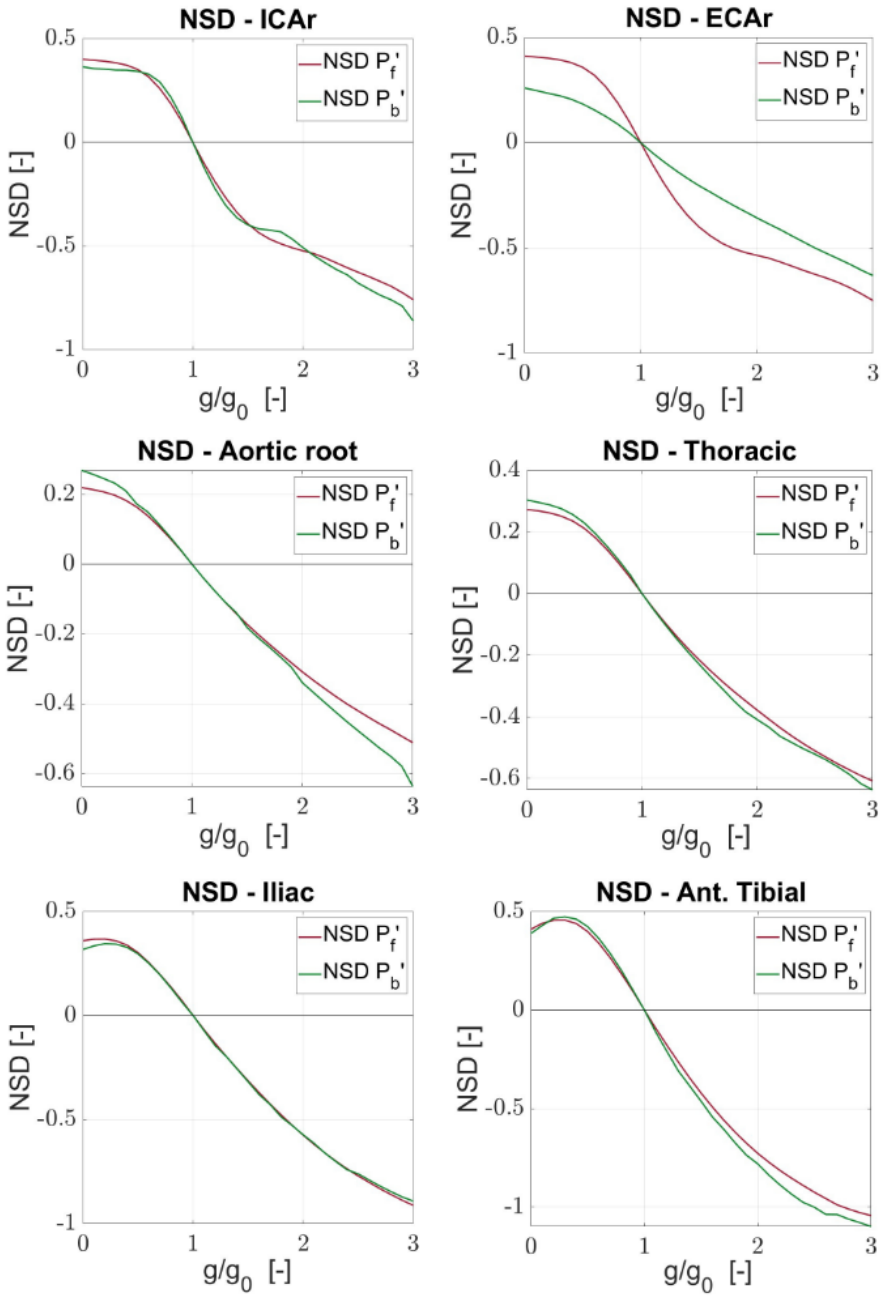

Figure 5.43: Signed NSD values of the decomposed normalized pressure waves. Each plot corresponds to a specific arterial site and shows the curve of the forward component (red line) and that of the backward component (green line). The NSD trends were computed over the full gravitational range from 0G to 3G, connecting the points evaluated with an incremental step of 0.1G by means of a continuous line.

The first two plots illustrate the NSD trends for forward and backward normalized signals at the two carotid sites analyzed. As already noted, it is clear that in the right internal carotid artery the extent of waveform deformation is rather similar for both the forward and backward components. In contrast, in the case of the right external carotid artery, the backward signal exhibits a reduced degree of waveform deformation compared to its forward counterpart.

The two central plots in figure 5.43 show the NSD trends for normalized forward and backward waves at two arterial sites located approximately at the level of the heart: the aortic root and the thoracic aorta. For both sites, within the 0.5G–1.5G range, the NSD curves for forward and backward signals are almost superimposed, whereas under more extreme micro- and hypergravity conditions a progressive separation between the two curves is observed. At the extremes of the gravitational range, in both sites, the backward signal displays larger NSD values compared to the forward one, with the difference between the two curves being more pronounced in the aortic root. Interestingly, this behavior is opposite to that observed in the right external carotid artery.

The last two plots in figure 5.43 refer to two sites more distant from the heart in the caudal direction: the iliac artery and the anterior tibial artery. At the iliac level, the NSD trends for forward and backward signals remain practically superimposed over the entire range of gravitational accelerations, while in the tibial site, for g/g_0 values greater than 1, the two curves exhibit an increasing divergence. Moreover, when examining in sequence the forward and backward NSD trends from the aortic root to the anterior tibial artery, a progressive widening of the range spanned by the NSD values is observed, indicating that the extent of waveform deformation increases with distance from the central region in the caudal direction, for both forward and backward signals. In addition, moving away from the aortic root in the caudal direction, a peak in NSD values emerges and progressively grows in the vicinity of gravitational accelerations between 0G and 0.5G. This feature is present in both the forward and backward pressure signals, as illustrated in the figure below.

Chapter 6

Conclusion

In this work, the impact of varying gravitational load on arterial hemodynamic wave propagation and waveform morphology was investigated through numerical simulations. The baseline model was defined as a 25-year-old male subject (75 kg, 175 cm) maintained in the upright position across all gravitational conditions, ranging from microgravity (0G) to moderate hypergravity (3G), with the field oriented along the cranio-caudal axis. The aim was to elucidate how gravitational stress modifies both pressure and flow rate signals, examined in terms of total waveforms as well as their decomposed components through the PU and PQ methods.

This concluding chapter summarizes the principal findings obtained, while discussing their physiological significance and broader implications. Emphasis is placed on the innovative aspects of the work, derived from the combined use of qualitative observations and ad hoc quantitative analyses.

With regard to total waveforms at arterial sites located below the level of the heart, an increase in gravitational acceleration along the cranio-caudal direction was found to exert distinct effects on pressure and flow signals. Specifically, for pressure waves, higher values of g translated into a clear increase in mean pressure, an effect that became progressively more pronounced toward the lower extremities. Conversely, flow waves exhibited a more complex behavior: while mean values decreased in the central/abdominal region with increasing orthostatic load, they increased at the level of the lower limbs. This result suggests a redistribution of blood flow below the heart level, confirming that an increase in mean flow is not necessarily associated with an increase in mean transmural pressure.

Unlike mean values, pulsatile values for both pressure and flow waves consistently exhibited a decreasing trend with increasing gravitational acceleration. The reduction in pulsatility of pressure waves was most pronounced in the central region (i.e.,

at the level of the aortic root), whereas for flow waves the reduction was slightly more significant in the periphery. Overall, the reduction in pulsatility emerges as a hallmark of a globally more demanding condition for the cardiovascular system, which becomes progressively more challenged as orthostatic load increases.

In this perspective, the results obtained in terms of wave velocity and characteristic impedance in the arterial vessels located below the level of orthostatic indifference can also be interpreted. Indeed, in the attempt to maintain central mean and pulsatile pressure levels sufficiently high to prevent potentially syncopal conditions in the subject as orthostatic stress increases, the physiological stiffening of arterial walls toward the periphery (linked to the physiological reduction of compliance in progressively more distal vessels) is supplemented by an additional short-term regulatory mechanism. This mechanism was shown to increase the incremental elastic modulus of caudal peripheral vessels, causing further wall stiffening in agreement with the observed increase in mean pressure values and wave velocity in the caudal region with increasing g. Such a mechanism represents a strategy of the cardiovascular system to counteract the downward fluid shift induced by the gravitational field, and is also related to a process of caudal peripheral vasoconstriction aimed at limiting the phenomenon of venous pooling. Indeed, although mean blood flow values increase with g and with distance from the heart in the caudal direction, they remain nonetheless contained and sustainable for the subject within the analyzed range.

Just as variations in wave velocity with gravitational acceleration were found to be negligible at the central level - where large vessels such as the aorta possess only limited vasodilatory and vasoconstrictive capacity - variations in characteristic impedance also proved to be rather limited centrally across the entire range of accelerations considered. By contrast, with increasing distance from the central region toward the caudal region, characteristic impedance values in more peripheral arterial vessels exhibited a progressive increase, which became increasingly pronounced as g rose. While short-term systemic regulatory mechanisms in the lower body are capable of eliciting the adaptive response to the increase in orthostatic load described above, arterial sites located above the level of orthostatic indifference appear to behave somewhat differently. In this work, the right external carotid artery and the right internal carotid artery were considered, the former supplying the extracranial region and the latter the intracranial region. Being situated above the level of the heart, the results show an opposite trend compared to the other analyzed sites, in terms of wave velocity and characteristic impedance, as would be expected. In both carotid vessels, wave velocity and the associated characteristic impedance decreased with increasing gravitational acceleration, indicating a progressive reduction in stiffness and a concomitant increase in compliance. In an

attempt to counteract the downward fluid shift induced by the growing orthostatic load, vessels in the upper body tend to accommodate as much blood volume as possible while maintaining transmural pressure levels as stable as possible. This behavior was particularly evident in the right internal carotid artery, which constitutes one of the inputs to cerebral circulation and thus plays a pivotal role in ensuring sufficient blood supply and in maintaining a nearly constant inlet pressure to the highly delicate cerebral organ.

This behavior of vessels positioned above the level of orthostatic indifference, namely, increasing compliance and decreasing wave velocity, is perfectly consistent with the trends observed in the reflection coefficients at the same sites: Reflection Magnitude and Reflection Index. Both parameters exhibited a clear reduction with increasing gravitational acceleration, indicating a reduction in the extent of wave reflection phenomena in the carotid arteries. This finding highlights the effectiveness of cerebral autoregulatory mechanisms, which tend to protect the intra- and extracranial regions from wave reflections, and is consistent with the reduced stiffness of these vessels at higher g levels. Conversely, the decreasing trend in reflection coefficients (RM and RI) observed in the other arterial sites located below the level of the heart proved at first to be somewhat surprising. In fact, although these vessels, particularly the most peripheral ones, experience reduced compliance and increased wave velocity and characteristic impedance, a progressive decrease in wave reflections was nonetheless observed. This result suggests the efficacy of wave trapping mechanisms along the arterial tree, capable not only of limiting the potentially hazardous increase of wave reflections along the aorta, but indeed of reducing their magnitude as gravitational acceleration rises.

By examining the trends of RM and RI, it becomes evident that this mechanism is particularly effective at the level of the aortic root, precisely where an increase in potential reflections would entail the highest risk for the regular functioning of the heart. Indeed, the aortic root is the site that exhibits the most significant decrease in RM, accompanied by only limited variability in RI. The marked reduction in RM indicates that the backward component of the pressure wave is progressively reduced in amplitude relative to the forward component as g increases, becoming increasingly less significant. Conversely, the nearly constant RI values at the level of the aortic root indicate that, overall, the impact of the backward pressure wave component remains small compared to the amplitude of the total wave.

An innovative aspect of this work lies in the identification of an ad hoc quantitative metric designed to evaluate the variation in waveform morphology as gravitational load changes: the NSD. This metric was applied both to flow and pressure signals, considering total waves as well as their decomposed components.

For the assessment of this parameter, it was necessary to define a reference signal (or baseline), which in this case was consistently chosen as the signal under 1G conditions. This parameter, based on the integration of the absolute value of the difference between two signals—one representing the baseline and the other the analyzed waveform—required a preliminary normalization process. Such normalization was carried out with respect to both the temporal axis (abscissa) and the amplitude (ordinate), in order to ensure comparability across signals, all characterized by the same dimensionless temporal extent, zero mean, and unit standard deviation.

Following this process, a first noteworthy observation emerged concerning the temporal phase shift of the signals relative to the baseline. Indeed, despite normalization, both flow and pressure waves at g/g_0 values lower than 1 were found to be advanced compared to the corresponding 1G signal, while at values greater than 1 they appeared delayed. Moreover, the extent of the temporal shift increased with gravitational acceleration across all analyzed signals. This behavior was observed not only for total waves, but also for the forward and backward components of the signals. In addition, the magnitude of this phase shift was proportional to the distance of the arterial site from the central region. Specifically, the aortic root consistently displayed the smallest phase shifts across the entire range of gravitational accelerations analyzed, while the anterior tibial artery exhibited the largest, both for pressure and flow waves. The effect of this temporal phase shift, however, revealed an influence on the NSD value due not to an intrinsic variation in waveform morphology, but rather to a potentially exclusive translational effect. To "clean" the NSD results from this spurious contribution, it was therefore decided to re-phase the analyzed signals so as to achieve the closest possible superposition with the reference signal, applying a temporal translation aimed at maximizing the cross-correlation coefficient with respect to the baseline. This reprocessing of the signals enabled the extraction of more meaningful information regarding actual waveform morphological variations. In particular, it was observed that, interestingly, the internal and external carotid arteries exhibited the greatest waveform alterations, both for pressure and for flow waves. By contrast, in the central region (aortic root, thoracic aorta, ...), the NSD values evaluated after re-phasing proved smaller, indicating reduced waveform alteration induced by increasing gravity.

Another noteworthy aspect concerns the overall lack of symmetry between microgravity and hypergravity conditions. Indeed, all NSD and phase-shift trends display slightly different behaviors when comparing the 0G–1G and 1G–2G gravitational ranges. In particular, whereas in microgravity there is a tendency toward stabilization of both NSD and phase-shift values, for g/g_0 greater than 1 the behavior is invariably monotonic, with no hint of a plateau. Moreover, some sites exhibit a slight peak in NSD within the 0G–0.5G range, which nonetheless tends to be

damped as the 0G condition is approached. These findings seem to suggest a fair capacity of the cardiovascular regulatory system to contain alterations in the morphology of pressure and flow waves as gravity decreases, in contrast to what is observed under hypergravity conditions.

An analogous observation can be made in the case of the decomposed signals, both forward and backward. Indeed, the waveform analysis conducted on signals obtained through decomposition of the total signal, in terms of NSD, yielded results similar to those observed for the total signals, particularly with regard to the forward components. The retrograde components, however, exhibited a different behavior especially at the level of the right external carotid artery, which, unlike the corresponding total signal, proved to be subject to a more limited alteration of waveform morphology. This seems to suggest a greater capacity within the extracranial circulation to contain variations in reflected waves as gravitational acceleration increases, compared with what occurs within the intracranial circulation.

The results highlighted thus far leave room for several questions that may be addressed in subsequent investigations. In particular, the lack of symmetry in waveform alteration (NSD) and in the magnitude of the temporal phase shift between micro- and hypergravity introduces a factor that warrants attention when considering exposure of a subject to gravitational acceleration exceeding 3G. Indeed, the absence of a plateau within the maximum hypergravity condition analyzed in this work raises several questions regarding the tolerability of higher orthostatic loads. For instance, it remains unclear whether NSD values exhibit a stabilization tendency under hypergravity conditions (for g/g_0 greater than 3) or whether no plateau behavior can be identified. In the future, therefore, it would be appropriate to extend the gravitational range on the hypergravity side, analyzing the short-term response of the cardiovascular system and investigating the potential emergence of plateau-like behavior in certain hemodynamic parameters as g increases. Beyond the analysis of waveform morphology and its alterations, further questions arise regarding wave-reflection phenomena. Indeed, the globally decreasing trends of the reflection coefficients (RM and RI) suggest the presence of an extremely effective wave-trapping mechanism—particularly along the aorta—capable of preserving proper cardiac function within the range of accelerations considered. However, the existence of a moving horizon for wave reflections and the precise functioning of such mechanisms remain unclear. In addition, whereas some sites seem to hint at plateau behavior under high orthostatic loads, in other vessels the trend appears to remain strictly monotonic. The issue of what would occur in terms of reflection coefficients for accelerations greater than 3G therefore remains to be defined.

This thesis, in conclusion, lays the foundations for many future developments

focused primarily on deepening the understanding of wave-trapping mechanisms along the aortic vessel and on the capacity of the cardiovascular system to manage wave-reflection phenomena as orthostatic stress increases. It is nevertheless necessary to underscore certain limitations of the present analysis with a view to possible future extensions. First, the multiscale model on which the proposed study is based is numerical/computational in nature and, as such, is unable to capture in full the complexities and interdependencies of real physiology. Moreover, the model is constructed by assuming certain uniform properties and constant parameters, which may pose challenges for the generalization of the results obtained. Second, the results presented in this work were obtained exclusively through a numerical–simulation approach which, however sophisticated the model may be, cannot reproduce real micro- and hypergravity conditions with complete fidelity. In this context, there is thus no actual validation of the results through experimental measurements performed on subjects under conditions of genuinely altered gravity. Furthermore, the model employed was calibrated to match the physiological conditions of a "standard," healthy, young male subject (25 years old), with anatomical cardiovascular parameters taken "from the textbook." This model therefore does not allow one to account for the inter-subject variability that inevitably characterizes each individual. With the analysis conducted, it was not possible, for example, to assess potential differences between male and female responses to the same inputs, nor to evaluate the impact of age or of possible pathological conditions of the subject on the investigated outcomes. Finally, it should be recalled that the variations of the gravitational field imposed in the analysis were treated as acute conditions aimed at probing the short-term response of the cardiovascular system. The analysis therefore did not take into account possible cardiovascular adaptations or remodeling that may arise following prolonged exposure to gravitational conditions different from terrestrial 1G.

Chapter 7

Appendix A

The constitutive law implemented in the current mathematical model establishes a nonlinear relationship between the local transmural pressure and the corresponding local cross-sectional area of each vessel. Furthermore, in the case of the carotid and vertebral arteries (vessels numbered No. 6, 12, 13, 16, 17, 20), the equation reported below has been supplemented with an additional hyperbolic model, which accounts for partial vessel collapse under conditions of very low transmural pressures.

$$P = B_1 + B_2 A + B_3 A^2 + B_4 A^3 - B_5 \frac{1}{\sqrt{A}} \frac{\partial Q}{\partial x} \tag{7.1}$$

The coefficients B_i $(i = 1, \dots 5)$ are defined as:

$$\begin{cases} B_1 = -\frac{1}{a_3^3}\left(a_5^3 + c_0^6\rho^3 + 3c_0^4\rho^2 a_5 + 3a_5^2 c_0^2\rho\right), \\ B_2 = \frac{3\rho c_0^2}{A_0 a_3^3}\left(\rho^2 c_0^4 + 2\rho a_5 c_0^2 + a_5^2\right), \\ B_3 = -\frac{3\rho^2 c_0^4}{A_0^2 a_3^3}\left(a_5 + \rho c_0^2\right), \\ B_4 = \left(\frac{\rho c_0^2}{a_3 A_0}\right)^3, \\ B_5 = \frac{K_v h_w}{2\sqrt{A_0} r_0}, \end{cases}$$

and are function of vessels' geometry and mechanical properties, through the **local wave velocity** at time $t = 0$ (c_0). In particular, c_0 is defined as:

$$c_0 = a_2/(2r_0)^{b_2} \tag{7.2}$$

The table below presents the values of the parameters related to the constitutive law:

a_5	-45348	N/m^2
a_3	1914	$N^{2/3}/m^{4/3}$
a_2	13.3	$m^{1.3}/s$
b_2	0.3	[-]

Table 7.1: Parameters of the constitutive law (7.1).

Furthermore,

- K_v is the effective viscosity of the wall;
- h_w is the wall thickness;
- A_0 is the vessels cross-section area at time $t = 0$;
- r_0 is the vessels radius at time $t = 0$.

Acknowledgements

Giunta al termine di questo percorso di tesi, desidero rivolgere un pensiero di gratitudine ai relatori e correlatori di questo progetto, ovvero la prof.ssa Stefania Scarsoglio, il prof.re Luca Ridolfi e il dottorando Francesco Tripoli.

In loro, l'indiscussa passione per gli argomenti approfonditi e per l'attività di ricerca è stata affiancata dalla rara capacità di creare un ambiente di lavoro basato sull'ascolto, sul dialogo e sulla gentilezza. Sono fiduciosa che il percorso che si svilupperà a partire da ora per i prossimi anni sarà arricchente sia dal punto di vista professionale sia da quello umano.

Bibliography

[1] Westerhof N, Sipkema P, Bos GVD, and Elzinga G. «Forward and backward waves in the arterial system.» In: *Cardiovasc. Res.* 6.6 (1972), pp. 648–656.

[2] Parker KH, Jones CJ, Dawson JR, and Gibson DG. «What stops the flow of blood from the heart?» In: *Heart Vessels* 4.4 (1988), pp. 241–245.

[3] Parker KH and Jones C. «Forward and backward running waves in the arteries: analysis using the method of characteristics.» In: *J. Biomech. Eng.* 112.3 (1990), pp. 322–326.

[4] Westerhof N, Stergiopulos N, Noble MI, and Westerhof BE. *Snapshots of hemodynamics: an aid for clinical research and graduate education.* Springer (New York, NY), 2010.

[5] Matteo Fois, Luca Ridolfi, and Stefania Scarsoglio. «Arterial wave dynamics preservation upon orthostatic stress: a modelling perspective». In: *R. Soc. Open Sci.* 10.3 (2023), p. 221257.

[6] Davies JE et al. «Attenuation of wave reflection by wave entrapment creates a 'horizon effect' in the human aorta.» In: *Hypertension* 60.4 (2012), pp. 926–933.

[7] Fois M, Maule SV, Giudici M, Valente M, Ridolfi L, and Scarsoglio S. «Cardiovascular response to posture changes: multiscal modeling and in vivo validation during head-up tilt.» In: *Front. Physiol.* 13 (2022), p. 826989.

[8] Saglietto A, Fois M, Ridolfi L, De Ferrari GM, Anselmino M, and Scarsoglio S. «A computational analysis of atrial fibrillation effects on coronary perfusion across the different myocardial layers.» In: *Sci. Rep.* 12 (2022), p. 15827.

[9] Kim H. Parker. «An introduction to wave intensity analysis». In: *Med Biol Eng Comput* 47.2 (2009), pp. 175–188.

[10] Hughes et al. «Waves in arteries: a review of wave intensity analysis in the systemic and coronary circulations.» In: *Artery Res.* 2.4 (2008), pp. 122–127.

[11] Jonathan P. Mynard1, Avinash Kondiboyina, Remi Kowalski1, Michael M. H. Cheung, and Joseph J. Smolich. «Measurement, Analysis and Interpretation of Pressure/Flow Waves in Blood Vessels». In: *Front. Physiol.* 11 (2020), p. 1085.

[12] F. Tripoli, L. Ridolfi, and S. Scarsoglio. «Assessing the cardiac function from micro-gravity to hyper-gravity conditions through a validated multiscale modelling approach». In: *The Journal of Physiology* (2025). Advance online publication. DOI: 10.1113/JP287142.

[13] C. Gallo, L. Ridolfi, and S. Scarsoglio. «Cardiovascular deconditioning during long-term spaceflight through multiscale modeling». In: *npj Microgravity* 6 (2020), p. 27.